SENSING, MONITORING AND CONTROL FOR LASER BASED WELDING OF ALUMINIUM SHEETS

Netherlands Institute
for Metals Research

The research described in this thesis was carried out in the framework of the Strategic Research Programme of the Netherlands Institute for Metals Research (www.nimr.nl).

Sensing, Monitoring and Control for Laser Based Welding
of Aluminium Sheets
Aalderink, Benno
ISBN 978-90-77172-31-5

Printed by PrintPartners Ipskamp.

SENSING, MONITORING AND CONTROL FOR LASER BASED WELDING OF ALUMINIUM SHEETS

PROEFSCHRIFT

ter verkrijging van
de graad van doctor aan de Universiteit Twente,
op gezag van de rector magnificus,
prof. dr. W.H.M. Zijm,
volgens besluit van het College voor Promoties
in het openbaar te verdedigen
op donderdag 4 oktober om 13.15 uur

door

Bernard Johan Aalderink
geboren op 9 september 1978
te Doetinchem

Dit proefschrift is goedgekeurd door
prof.dr.ir. J.B. Jonker, promotor
prof.dr.ir. J. Meijer, promotor
dr.ir. R.G.K.M Aarts, assistent-promotor

"Time is fun when you are having flies."

Kermit the Frog

Voorwoord

Gaat toch snel voorbij, vier jaar onderzoek doen. Voor ik begon, leek het een lange tijd en heb ik wel even moeten nadenken of ik wel zo lang met één onderwerp bezig zou willen zijn. Nu de tijd voorbij is heb ik het gevoel dat ik nog zo vier jaar verder zou kunnen werken hieraan. Ik ben dan ook blij dat ik uiteindelijk toch gekozen heb voor een promotieplaats bij het NIMR en heb mijn tijd bij Werktuigbouwkundige Automatisering als zeer prettig en leerzaam ervaren. Dit onderzoek en proefschrift was niet mogelijk geweest zonder de steun van velen.

Allereerst wil ik het NIMR bedanken voor het mogelijk maken van dit onderzoek. Zonder deze bijdrage was dit onderzoek niet mogelijk geweest. Ben Jonker en Johan Meijer wil ik bedanken voor het vertrouwen dat jullie in mij gesteld hebben. Ik heb alle ruimte gekregen om het onderzoek naar eigen wens in te richten, iets wat lang niet altijd vanzelfsprekend is. Ook wil ik graag Ronald Aarts heel hartelijk danken voor de uitstekende coaching in de afgelopen jaren. Zelden heb ik iemand zo efficiënt zien werken (en snel horen praten). Verder wil ik Frits de Lange en Pathiraj hartelijk danken voor de aanbevelingen en correcties op dit proefschrit.

Naast dat het een erg leerzame tijd was, was het vooral ook erg gezellig. Dit is met name te danken aan de groep collega's bij WA, in alfabetische volgorde: Ben, Bertus, Dannis, Dimi (Helga), Frank (the man die alles can), Frits, Gert, Hiddo, Jan, Jeroen OB (en toch heb ik de grootste kop), Jeroen vT (Volvo 480 forever ... toch?), Jilles, Johan, Johannes, Jonathan (Johnny kroepølie), Leo, Martina, Max, Menno, Pathiraj, Ronald, Sjoerd, Tjeerd, Toon (con i dito rapida), Tyrone en Wouter. Ook wil ik alle afstudeerders

bijzonder bedanken voor hun inzet: Jelle, Jeroen, Juan en Bart-Jan.

Het leuke van het werken voor het NIMR is dat je ontzettend dicht bij het bedrijfsleven staat. Binnen mijn project heb ik intensief samengewerkt met Corus PAC. In het begin was het allemaal een beetje aftasten van beide zijden, maar uiteindelijk hebben we een goede relatie opgebouwd. Bij Corus wil ik met name Cierick Goos en Tony van der Veldt hiervoor bedanken. Daarnaast is ook de samenwerking met collega's binnen NIMR Cluster 8 is altijd erg prettig verlopen.

Ook was het af en toe erg fijn om de gedachten eens helemaal te verzetten. Af en toe een biertje drinken met de Pompwortels helpt dan uitstekend (zeg Benno, wanneer krijg je nu eens een echte baan?).

Graag wil ik mijn familie bedanken voor de ondersteuning en de motivatie die ze mij de afgelopen jaren altijd gegeven hebben. Het is erg fijn te weten dat jullie achter mij staan.

Als laatste wil ik graag Wendy bedanken. Jij weet mij altijd weer te motiveren en hebt aan een half woord genoeg. Bedankt dat je af en toe even op de rem trapt.

Benno Aalderink
Enschede, juli 2007

Nomenclature

Abbreviations

2D/3D	Two/three dimensional
a.u.	Arbitrary units
CCD	Charged coupled devices
CW	Central wavelength
EBW	Electron beam welding
FEM	Finite element method
FLC	Fuzzy logic control(ler)
FOV	Field of view
FWHM	Full width half maximum
GMA	Gas metal arc
HAZ	Heat affected zone
HLG	Hybrid laser/GMA welding
LPF	Low pass filter
LW	Laser welding
LWM	Laser weld monitor
MZ	Melt zone
Nd:YAG	Neodymium-doped yttrium aluminium garnet
PRS	Power regulator system
ROI	Region of interest
RW	Resistance welding
SS	Single spot laser welding

SSCW	Single spot laser welding with cold wire feeding
TS	Twin spot laser welding
TSCW	Twin spot laser welding with cold wire feeding
TWB	Tailor welded blank
WMS	Weld monitor system
WW	Weldwatcher

Symbols

A	Absorptivity	
A_f	Cross sectional area of a fluid flow	m^2
a_x	Polynomial coefficient	
b	Material thickness	m
c	Speed of light in vacuum ($2.998 \cdot 10^8$)	m/s
c_p	Specific heat	J/(kg K)
c_p^*	Specific heat, including the latent heat of the solid-liquid phase transition	J/(kg K)
c_r	Recondensation factor	
d	Diameter	m
d_s	Laser spot diameter	m
e	Difference between reference and measurement value of the sensor signal	
$\boldsymbol{e_{x_i}}$	Unit vector along the x_i axis	
$\boldsymbol{e_n}$	Unit vector normal to a boundary	
$\boldsymbol{F}$	Volumetric force	N/m^3
F_λ	Wavelength dependant scaling function	
g	Gravitational acceleration (9.81)	m/s^2
H_V	Vickers hardness	HV
h	Height	m
I	Irradiance	W/m^2
I_E	Erichsen index	m
$I_{E\%}$	Erichsen index as fraction of the base material value	

I_c	Irradiance at coaxial measurement position	W/m^2
I_o	Irradiance at off-axis measurement position	W/m^2
K	Proportionality factor	
$K_{i\uparrow}$	Tuning parameter for the integrating action of the PI-controller, when the laser power is increased	
$K_{i\downarrow}$	Tuning parameter for the integrating action of the PI-controller, when the laser power is decreased	
$\boldsymbol{K_k}$	Diagonal 2x2 matrix with tuning parameters for the force term in the FEM model, that forces the material flow around the keyhole	
$K_{p\uparrow}$	Tuning parameter for the proportional gain of the PI-controller, when the laser power is increased	
$K_{p\downarrow}$	Tuning parameter for the proportional gain of the PI-controller, when the laser power is decreased	
$\boldsymbol{K_s}$	Diagonal 2x2 matrix with tuning parameters for the force term in the FEM model, that freezes the material outside the melt contour	
k	Thermal conductivity	W/(m K)
k_W	Wien's displacement constant ($2.897{\cdot}10^{-3}$)	m K
L	Latent heat function	J/K
L_m	Latent heat of the solid-liquid phase transition	J
L_v	Latent heat of the liquid-gas phase transition	J
l	Length	m
l_k	Keyhole length	m
l_m	Melt pool length	m
l_w	Cross sectional wetted length of the fluid flow	m
P	Laser power	W
P_a	Absorbed laser power	W
P_g	Mean GMA power	W

P_i	Initial laser power	W
$\dot{P}$	Laser power change	W/s
$\boldsymbol{\dot{P}_W}$	Laser power change vector	W/s
Pe	Peclet number	
p	Pressure	Pa
p_0	Atmospheric pressure	Pa
p_a	Ambient pressure	Pa
p_d	Hydrodynamical pressure	Pa
p_i	Radiation pressure	Pa
p_r	Recoil pressure	Pa
p_s	Hydrostatical pressure	Pa
p_γ	Surface tension pressure	Pa
$\boldsymbol{Q}$	Weight vector	
q	Heat source	W/m^3
q_i	Total heat input per weld length	J/m
R	Reflectivity	
R_h	Hydraulic radius	m
R_k	Ratio of keyhole length to keyhole width	
R_s	Spectral response of the sensor	
R_γ	Ratio of opening and closing surface tension pressure terms	
Re	Reynolds number	
r	Radius of curvature	m
r_k	Keyhole radius	m
r_s	Radius of laser beam at the focal point	m
$\boldsymbol{S}$	Sensor signals vector	
$\boldsymbol{S_f}$	Filtered sensor signals vector	
S_f^*	Filtered sensor signals vector divided by the laser power	
$\boldsymbol{S_t}$	Reference values for sensor signals	
S_t^*	Reference value for sensor signal divided by the laser power	
s	Gap width	m
T	Temperature	K

T_b	Boiling temperature	K
T_c	Critical temperature	K
T_f	Transmittance optical filters	
T_k	Keyhole wall temperature	K
T_l	Liquidus temperature	K
T_m	The average of the liquidus and solidus temperature	K
T_r	Room temperature	K
T_s	Solidus temperature	K
t	Time	s
$\boldsymbol{u}$	Local speed	m/s
v	Welding speed	m/s
v_f	Fluid flow velocity	m/s
v_w	Wire feeding speed	m/s
$\boldsymbol{W}$	Weld identification vector	
w	Width	
w_k	Keyhole width	m
w_m	Melt pool width	m
$\boldsymbol{x}$	Spatial coordinates	m
z	Dimensionless function	
γ	Surface tension	N/m
$\partial\Omega_i$	Boundary of computational domain i	
ϵ	Strain	
λ	Wavelength	m
λ_{max}	Wavelength where the black body temperature radiation curve reaches it's maximum value	m
μ	Dynamic viscosity	kg/(m s)
ρ	Density	kg/m^3
σ	Stress	Pa
σ_b	Ultimate tensile strength	Pa
$\sigma_{b\%}$	Ultimate tensile strength as fraction of the base material value	
Ω_i	Computational domain i	

Notations

$\tilde{a}$	Dimensionless version of a
$\boldsymbol{a}$	Vector or array
$\boldsymbol{a^T}$	Transpose of $\boldsymbol{a}$
$\dot{a}$	$\frac{d}{dt}a$
$a(b)$	a is a function of b
$a \cdot b$	In-product of a and b
∇	$(\frac{\partial}{\partial x_1}, \ldots, \frac{\partial}{\partial x_N})$

Contents

Voorwoord **i**

Nomenclature **iii**

Contents **ix**

1 Introduction **1**
1.1 Conduction and Keyhole Laser Welding 1
1.2 Laser Welded TWB's 4
1.3 AA5182-O/H111 7
1.4 Research Objectives 7
1.5 Outline and Contributions 9
1.6 Publications 10

2 Photodiode-Based Fuzzy Logic Control of Laser Welding **13**
2.1 Introduction 13
2.2 General FLC Framework for Laser Welding Control 17
2.3 The Switching Controller in the FLC Framework 20
2.3.1 The Switching Controller 20
2.3.2 Reformulation of the Switching Controller 23
2.4 Experimental Setup FLC System 26
2.5 Implementation of FLC for Aluminium 29
2.5.1 FLC Framework 29
2.5.2 Controller Tests 32

2.6 Implementation of FLC for Zinc Coated Steel 35
2.6.1 FLC Framework 35
2.6.2 Controller Tests 38
2.7 Conclusions 43

3 Camera-Based Monitoring of Laser Welding 45
3.1 Optical Process Emissions 45
3.1.1 Experimental Setup for Spectroscopic Measurements 47
3.1.2 Spectroscopic Measurement Results 49
3.2 Camera-Based Systems 52
3.2.1 Visualisation of Aluminium Laser Welding 52
3.2.2 Physical Principles Monitoring System 53
3.2.3 Prototype Monitoring System 54
3.2.4 Monitoring System Performance 57
3.3 Conclusions 61

4 Melt Pool Shape 63
4.1 Melt Pool Modelling 64
4.2 Computational Domain 65
4.3 Thermal Model 66
4.4 Hydrodynamical Model 69
4.5 Solution Strategy 71
4.6 Experimental Verification for Aluminium 74
4.7 Experimental Verification for Mild Steel 80
4.8 Conclusions 86

5 Keyhole Shape 89
5.1 Keyhole Shape Variations 90
5.2 Pressure Terms at the Keyhole Wall 93
5.2.1 Pressure Balance 93
5.2.2 Surface Tension Pressure 96
5.2.3 Radiation Pressure 97
5.2.4 Hydrodynamical Pressure 98
5.2.5 Hydrostatical Pressure 98

Contents

5.2.6 Recoil Pressure 98
5.3 Keyhole Elongation and Weld Bead Formation 100
5.4 Experimental Verification for Aluminium 103
5.5 Experimental Verification for Mild Steel 105
5.6 Conclusions 107

6 Gap Bridging with Laser-Based Welding Processes 109
6.1 Twin Spot Laser Welding 110
6.2 Laser Welding with Cold Wire Feeding 114
6.3 Hybrid Laser/GMA Welding 119
6.4 Gap Bridging Capabilities 126
6.4.1 Visual Inspection of the Weld Bead 128
6.4.2 Microscopic Inspection of Cross Sections 135
6.4.3 Micro Hardness Measurements 140
6.4.4 Tensile Tests 143
6.4.5 Erichsen Cupping Tests 147
6.5 Conclusions 150

7 Conclusions and Recommendations 153
7.1 Conclusions 153
7.2 Recommendations 155

A Aluminium Alloy Designation 159

B Filter Characteristics 161

C Material Parameters 165
C.1 AA5182 165
C.2 FeP04 168

D Estimation of Reynolds Number for Melt Pool Flow 171

Bibliography 174

Summary 183

Contents

Samenvatting **185**

Chapter 1

Introduction

Solid state laser welding has become an important joining technique in today's industry. In this chapter, a general introduction of the laser welding process is presented. Section 1.2 gives an overview of the applications of laser welding in the automotive industry. After this, more specific information is given about a laser welding application that is typically encountered in the automotive industry, namely the production of Tailor Welded Blanks (TWB's). At the end of the chapter, the objectives of this research are stated, followed by an outline of the remainder of this thesis and an overview of the contributions of the author to the subject of laser welding of aluminium TWB's.

1.1 Conduction and Keyhole Laser Welding

The continuous wave Nd:YAG rod solid state laser is a well established laser source in industry. With a wavelength of 1064 nm, it is well suited for welding of aluminium alloys, since the absorption coefficient of these materials is relatively high for this wavelength. This laser light can be transported using optical fibers, which is an advantage for situations in which a flexible beam delivery system is required. Traditionally, Nd:YAG rod lasers are pumped using flash lamps. For a better efficiency, diode laser

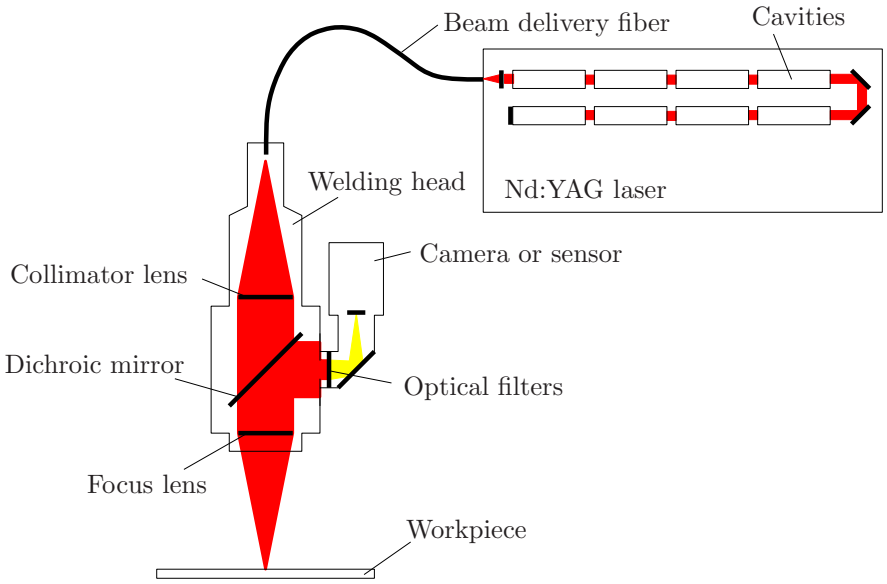

Figure 1.1: *Schematic overview of a typical laser welding system.*

stacks can be used for optical pumping. Nd:YAG rod lasers are available up to 6 kW laser power, with a moderate beam quality [1, 2]. The experimental work described in this thesis was mainly performed using a 4 kW lamp-pumped Nd:YAG rod laser source (Figure 1.1).

At the end of the beam delivery fiber, the laser beam diverges. To reach the high intensity levels needed for laser material processing, the beam needs to be focussed onto the workpiece. This is done using a laser welding head. This optical system usually consists of a collimator lens, which changes the diverging beam to a parallel beam, and a focus lens, which focusses the beam on the workpiece. In fact, both lenses image the exit of the fiber on the workpiece. Sometimes a dichroic mirror is placed at an angle of 45^o to the optical axis in the path of the parallel beam. This mirror is transparent for the Nd:YAG laser radiation, but reflects visible light partially. In this way a camera or sensor system can "view" the

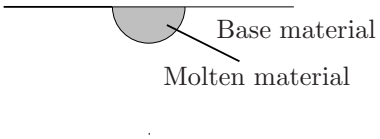

Figure 1.2: *The conduction welding mode.*

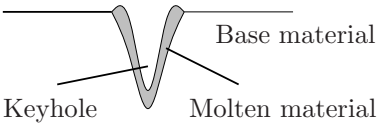

Figure 1.3: *The keyhole welding mode.*

welding process coaxially with the laser beam.

In the case of laser welding, either the welding head is moved over the sample, or the workpiece is moved underneath a stationary laser beam. Usually the welding area is covered with an inert gas, to prevent oxidation and pore formation during welding. Throughout this research, argon is used as shielding gas.

In laser welding, two different welding modes occur, depending on the intensity of the laser light on the sample surface. Up to an irradiance of approximately 10^8 W/m^2, the metal irradiated by the laser spot melts and the heat is mainly transported by conduction [1]. This welding mode is therefore referred to as conduction welding. Figure 1.2 illustrates this welding mode, in which the width and the depth of the melt pool have the same order of magnitude.

When the irradiance rises to about 10^{10} W/m^2, the conduction welding mode changes into a keyhole welding mode [1]. At these intensity levels, the evaporation pressure on the melt surface becomes large enough to initiate and maintain a gas column inside the metal, which is called a keyhole. This gas column allows the laser light to penetrate the metal much deeper, which results in a weld with a very high depth-to-width-ratio (Figure 1.3). In this welding mode, deep penetration welds can be made with a low heat input compared to other welding processes, thus minimising thermal deformations of the sample. The metal vapour inside and above the keyhole (Figure 1.4) emits process light, which will be discussed in Chapters 2 and 3.

In Figure 1.4, a cross section of the interaction zone of the laser with the material is shown for the full penetration keyhole welding process of a thin

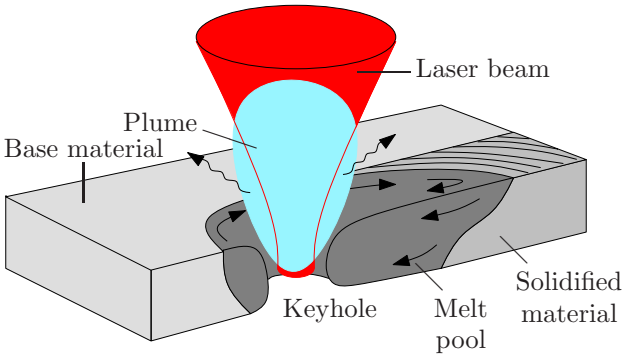

Figure 1.4: *Schematic cross section of the full penetration keyhole laser welding process of a thin sheet.*

sheet. In this cross section the melt pool, keyhole and solidified weld bead are indicated. Also the plume, which emits light, is shown. The arrows in the melt pool roughly indicate the local direction of the melt flow.

1.2 Laser Welded TWB's

Laser welding has found its way in many industrial applications. Although it has taken some time for the automotive industry to adopt this welding technique, nowadays it is often used. A modern car contains approximately 40 m of laser welds in total. The first laser welding cells have been installed in the mid-eighties. In the automotive industry, the production volumes are high and reliability and operational costs are very important. Therefore, most laser welding research focusses on increasing the productivity and robustness of the process.

For environmental and economical reasons, car manufactures are always searching for ways to reduce the weight of cars while maintaining optimal strength. An important way to achieve this is by the use of Tailor Welded Blanks (TWB's). These are body panels consisting of sheets with different thicknesses and/or materials, welded together and formed into the desired

1.2 Laser Welded TWB's

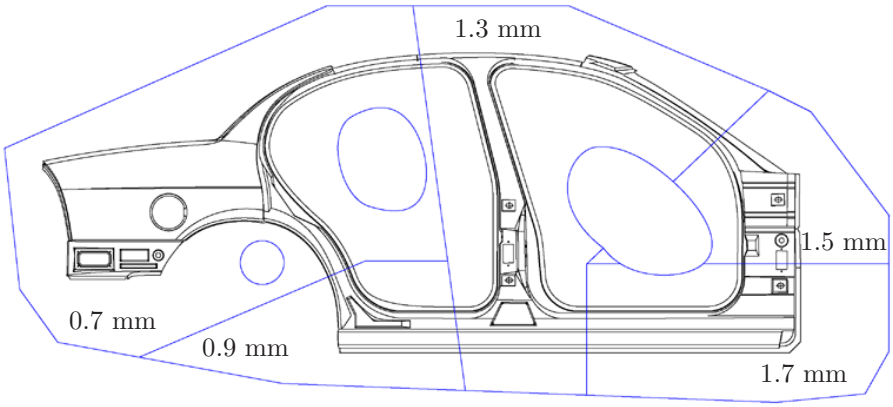

Figure 1.5: *Example of the layout of a TWB for a side panel of a car (Courtesy of the International Iron & Steel Institute)*

shape. TWB's are thicker in areas where high loads occur and thinner in other areas. In this way, a considerable weight reduction can be achieved [3]. In Figure 1.5 an example of a layout of a TWB for the side panel of a car is shown.

In recent years, other materials besides mild steel are used more and more in car bodies. For weight reduction, aluminium alloys and high strength steel sheets are well suited. For a good corrosion resistance, zinc coated steel is often used. These materials pose new challenges for laser welding. Steel TWB's have been used in car bodies now for over 20 years. However, TWB's of aluminium alloys have only recently been introduced. In 2003 Corus developed the first serially produced aluminium TWB: a part of the Lamborghini Gallardo front wheel arch (Figures 1.6 and 1.7). This TWB is produced using laser keyhole welding [4].

Due to the high welding speed, the non-contact nature of the process and the suitability for process automation, laser welding is well-suited for the production of TWB's. The resulting welds have a high tensile strength and good formability compared to welds produced with other welding processes.

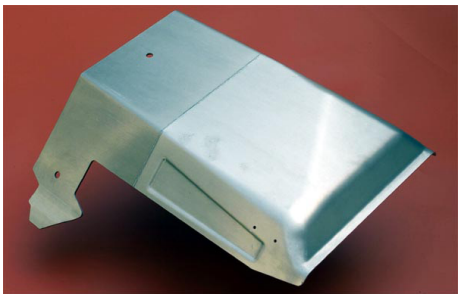

Figure 1.6: *The first aluminium TWB, welded by Corus (Courtesy of Corus)*

Figure 1.7: *A Lamborghini Gallardo, containing the first aluminium TWB as part of the front wheel arches (Courtesy of Audi AG).*

(a) Sheets of equal thickness.

(b) Sheets of unequal thickness.

Figure 1.8: *Schematic overview of a butt weld configuration.*

These strength and formability are required during the mould forming stage of the TWB's [5].

In the production of TWB's, sheets are typically welded in a butt weld configuration (Figure 1.8). In this configuration, the laser beam must be carefully aligned with the sheet edges to obtain a sound weld at the correct position. The maximum allowable misalignment is about 0.2 to 0.3 mm. This imposes high demands on workpiece clamping and manipulator accuracy. It is also important that the sheets fit-up well and that no gap is present between the sheets. This requires good edge preparation and clamping of the sheets [6].

Element	Mg	Mn	Cu	Si	Ti	Al
Content [wt%]	4.90	0.26	0.11	0.08	0.01	Bal.

Table 1.1: *The composition of the AA5182-O/H111 base material (information provided by Corus).*

1.3 AA5182-O/H111

Since this project focusses on laser welding for automotive industry, a typical automotive quality material was selected. For aluminium exterior car parts, usually AA6xxx aluminium alloys are used (a description of the ANSI aluminium alloy designation is given in Appendix A). Due to the high Si content, these materials are sensitive for hot cracking during welding. This can be prevented by using an appropriate filler alloy and parameter settings [7].

Aluminium interior car parts are typically constructed using AA5xxx alloys, which can be welded with or without a filler wire. AA5xxx series alloys possess good welding characteristics and corrosion resistance. AA5182-O/H111 is a standard material produced by Corus, used for the production of aluminium TWB's and was selected for the experimental work described in this thesis. The composition of AA5182-O/H111 is given in Table 1.1. Since TWB's are typically made of sheets with thicknesses ranging from 1 to 3 mm, 1.1 and 2.1 mm sheets were selected for this research.

AA5182-O/H111 alloy has significant quantities of Mg in solid solution (4.9 wt%), which increases the strength, while not compromising the ductility. These sheets have been annealed and subsequently strain-hardened slightly by cold rolling [8, 9]. The important properties of these sheets in the context of this work, are summarised in Appendix C.

1.4 Research Objectives

Many researchers have investigated the laser welding of aluminium alloys. However, there still remain many unanswered questions. For TWB's pro-

duction, a full penetration weld without welding defects is very important. To guarantee this, a thorough understanding of the keyhole laser welding process is necessary. For the full penetration laser welding of thin aluminium sheets, the behaviour of the keyhole, its relation to the resulting weld bead shape and the relation to sensor signals are not fully understood.

A camera-based real-time monitoring system is required for a fundamental investigation of the laser welding process. Such a system could also provide a basis for a control system which can reliably produce defect free joints. However, since the visualisation of the laser welding process of aluminium has proven to be very difficult, such a camera-based system is not commercially available.

There are different techniques currently available to improve the quality of laser welds, like the use of twin spot optics, cold wire feeding and the combination of laser welding with arc welding. To facilitate a selection of a suitable welding technique for a specific application, a quantitative comparison of the gap bridging capabilities of these different laser welding techniques is required.

In this research, many of the above stated problems are addressed. The objectives are summarised below:

- Development of a photodiode-based penetration control system for the keyhole laser welding of metal sheets, with an emphasis on aluminium and zinc coated steel. With this system full penetration should be guaranteed during the welding process, which will increase the robustness of the laser welding process for TWB's.
- Development of a camera-based optical monitoring system for the keyhole laser welding of metal sheets, with an emphasis on aluminium. With this monitoring system, process models can be validated.
- Development and validation of process models of the keyhole and melt pool, which will provide a better fundamental understanding of the laser keyhole welding process for TWB's.
- Evaluation of different laser-based welding techniques, like twin spot laser welding, laser welding with cold wire feeding and hybrid laser/GMA

welding, for the tolerance of gaps during the welding of aluminium TWB's. This investigation should result in guidelines for the suitability of these processes in different applications.

1.5 Outline and Contributions

For penetration control of the laser welding process, commercially available photodiode-based sensor systems are available. In Chapter 2, a fuzzy logic control system based on these sensor systems is described, which can maintain full penetration during the laser welding process of zinc coated steel and aluminium sheets. For zinc coated steel, this system proves to be robust against the influence of external disturbances and is suitable for industrial implementation. For aluminium this system is not suited, since the performance is very dependent on external influences and the results are difficult to reproduce. For a more reliable monitoring and/or control system for aluminium alloys, a camera-based system is necessary.

For a fundamental investigation of the laser welding process, a camera-based monitoring system is required, which is able to produce a good image quality in the presence of the optical emissions of the welding process. The development this monitoring system is described in Chapter 3. Using this system, the welding process can be visualised much clearer than any commercially available system can. This system can also be used as a basis for a camera-based control system for the laser welding of aluminium sheets.

In Chapter 4, a Finite Element model of the laser keyhole welding process is presented, which gives considerable insight into the thermal profile and the flow in the melt pool. With this model, the melt pool shape can be predicted in a qualitative way for the welding of both aluminium alloy and mild steel sheets. Chapter 5 describes modelling of the pressure balance at the keyhole wall. Using this model, changes in the keyhole shape can be explained, which are strongly related to the resulting weld quality.

In Chapter 6 different laser-based welding techniques are described in detail and are tested. Processes, like for instance the twin spot laser welding process with cold wire feeding and the hybrid laser/GMA welding process

are evaluated for their gap bridging capabilities. A quantitative overview is presented which can be used for selection of suitable techniques for the welding of thin aluminium sheets.

A summary of the conclusions and some recommendations for further research is provided in Chapter 7.

1.6 Publications

2007

- J. Jauregui, B.J. Aalderink, R.G.K.M. Aarts, J. Olde Benneker, and J. Meijer. Design, Implementation and Testing of a Fuzzy Control Scheme for Laser Welding. *Journal of Laser Applications*, in press.

- B.J. Aalderink, D.F. de Lange, R.G.K.M. Aarts, and J. Meijer. Experimental Observation of Keyhole Shapes in the Laser Welding of Aluminium Blanks. *Journal of Laser Applications*, in press.

- B.J. Aalderink, D.F. de Lange, R.G.K.M. Aarts, and J. Meijer. Keyhole shapes during laser welding of thin metal sheets. *Journal of Physics D: Applied Physics*, 40:5388-5393, 2007.

- B.J. Aalderink, R.G.K.M. Aarts, and J. Meijer. Increased gap bridging capabilities using twin spot and hybrid laser/GMA welding for AA5182. *Proceedings of LIM '07*, pages 79-83, 2007.

2006

- B.J. Aalderink, D.F. de Lange, R.G.K.M. Aarts, and J. Meijer. Experimental verification of multi-physical modelling of the keyhole laser welding process. *Proceedings of ICALEO '06*, pages 479-486, 2006.

2005

- B.J. Aalderink, R.G.K.M. Aarts, J.B. Jonker, and J. Meijer. Weld

Plume Emissions During Nd:YAG Laser Welding. *Proceedings of LIM '05*, pages 413-417, 2005.

- B.J. Aalderink, R.G.K.M. Aarts, J.B. Jonker, and J. Meijer. Experimental Observations of the Laser Keyhole Welding Process of AA5182. *Proceedings of ICALEO '05*, pages 832-836, 2005.

2004

- B.J. Aalderink, R.G.K.M. Aarts, J.B. Jonker, and J. Meijer. Study of the Optical Emissions During Nd:YAG Laser Welding of AA5182. *Proceedings of ICALEO '04*, 2004.

Chapter 2

Photodiode-Based Fuzzy Logic Control of Laser Welding

Optical sensors are often used to monitor the laser welding process. Such sensors can be divided into two categories: photodiode-based systems and camera-based systems. Photodiode-based sensors have a high temporal resolution, but provide no direct spatial information. In this chapter, commercially available photodiode-based sensor systems are used with a fuzzy logic control structure. The aim is to ensure full penetration keyhole welding, even in the presence of external disturbances like drifts in focal position and material thickness variations.

2.1 Introduction

With TWB laser welding, full penetration welds are required to obtain a high quality joint. To minimise production costs, it is also desirable to use a high welding speed. In this context, monitoring the weld penetration on-line or using a control system to ensure full penetration can be of considerable advantage. On-line monitoring and control of weld penetration during the

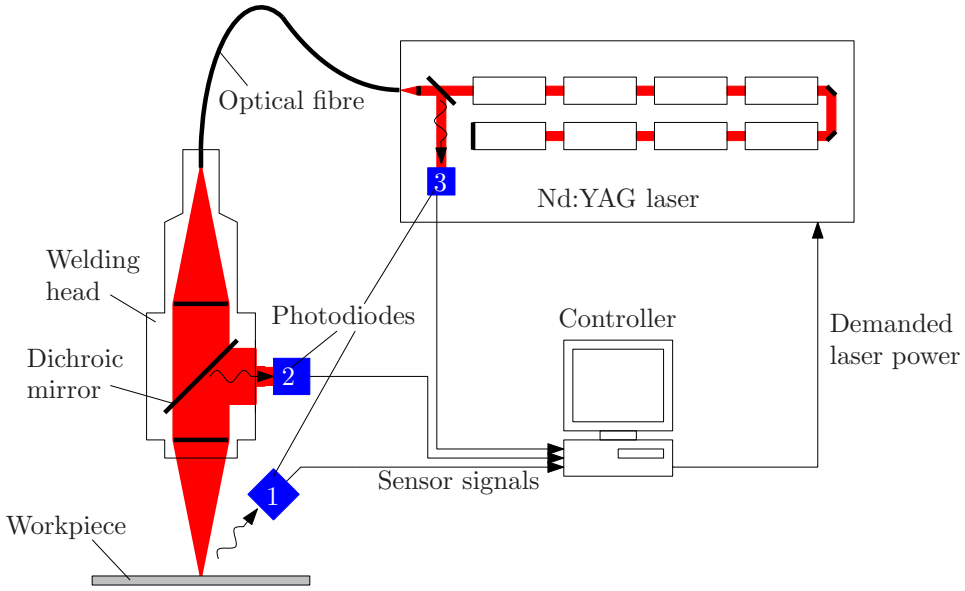

Figure 2.1: *Schematic overview of an experimental setup for laser welding with penetration control, using photodiode sensors.*

laser welding of thin sheets using photodiodes has been demonstrated in the past [10, 11, 12, 13, 14, 15].

In Figure 2.1 an overview of a typical experimental setup used for photodiode-based penetration control is given. The laser light is transported from an industrial Nd:YAG laser source to the welding head by means of an optical fiber. Using this welding head, the laser beam is focussed on the workpiece by the collimator and focus lenses. The photodiode can be placed at various locations in the setup. Position 1 is the so-called off-axis position, and provides the diode with a direct view of the welding process. When the photodiode is placed in position 2, it has a coaxial view of the process via the dichroic mirror. There are also photodiode systems available that are placed inside the laser source (position 3). These systems record light that is emitted by the laser welding process and which is

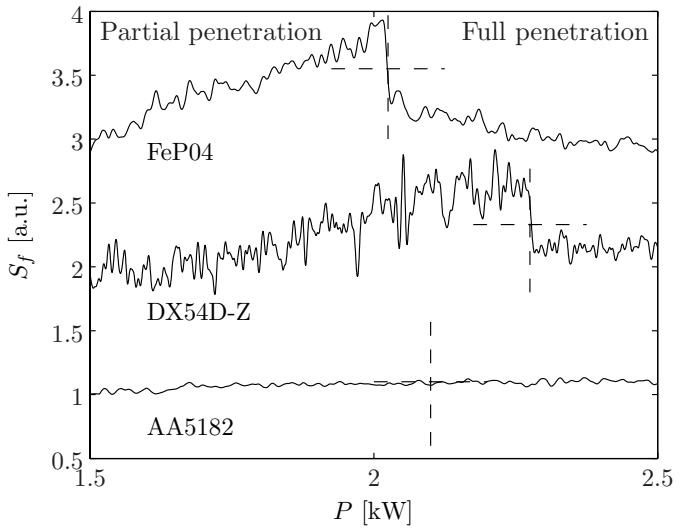

Figure 2.2: *The filtered Weldwatcher sensor signal S_f as function of the laser power P for FeP04 (v = 140 mm/s), AA5182 (v = 140 mm/s) and DX54D-Z (v = 70 mm/s). The vertical dashed lines indicate the transition from partial to full penetration for each welding process, the horizontal dashed lines indicate a possible threshold level for the detection of this transition.*

transported back to the laser through the optical fiber.

Postma et al. demonstrated a control system for the laser welding of FeP04 (mild steel) TWB's, which is capable of maintaining a full penetration, by controlling the laser power [16, 17]. This system uses a photodiode sensor placed at position 3 in Figure 2.1. The controller makes use of a jump in the signal level, which can be observed as the keyhole penetrates the sheet (top signal in Figure 2.2). When the keyhole fully penetrates the sheet, the signal is below a certain threshold (in Figure 2.2 examples of these threshold levels are displayed). In this situation, the controller slowly reduces the laser power in an effort to minimise the applied laser power

while maintaining full penetration. When the keyhole starts to close at the bottom, the signal rises above the threshold level. The controller reacts to this by quickly increasing the laser power. This results in a welding process that is always fully penetrated, while using an optimal laser power setting. This system was later expanded by de Graaf et al. [18]. More details of the control systems of Postma and de Graaf are given in Section 2.3.

For the automotive industry, aluminium and zinc coated steel sheets are also of interest. Figure 2.2 includes the filtered Weldwatcher (WW) sensor signals recorded during welding of aluminium alloy AA5182-O/H111 in a butt weld configuration and zinc coated steel DX54D-Z GI in an overlap configuration, in addition to the signal recorded during the welding of mild steel FeP04 in a butt weld configuration. The signals have been filtered using a fourth order low-pass Butterworth filter with a cut-off frequency of 100 Hz. For FeP04 and AA5182 a welding speed of 140 mm/s was used. DX54D-Z was welded at a welding speed of 70 mm/s.

As was seen with the FeP04 welding process, DX54D-Z welding also showed the sensor signal value to drop as the keyhole penetrates the bottom sheet. However, this drop is less pronounced. For lower welding speeds (e.g. 30 mm/s), this distinctive drop, which forms the basis of the switching controller, could not be observed (not shown in the figure). For the AA5182 welding process, this distinctive drop in the sensor signal does not manifest at all, irrespective of the welding speed. This is confirmed by findings of de Graaf [18]. Therefore, for the AA5182 and DX54D-Z welding processes it is very difficult to reliably estimate the welding mode based on this single sensor signal.

To overcome the above limitation, it was considered that use of a multi-sensor system may be necessary. Hence, in this work, a combination of several photodiode sensor signals were used. In most cases, each of these individual signals contains insufficient information for a reliable estimation of the welding mode. However a combination of these signals may result in a better estimate.

Both the need to use multiple sensor signals and the fact that the relation between the laser power and the resulting weld penetration is highly non-linear are strong arguments to use a Fuzzy Logic-based controller. In

this chapter, a Fuzzy Logic Controller (FLC) for penetration control of the laser welding process is treated.

In Section 2.2, the general structure of a Fuzzy Logic penetration controller developed for the laser keyhole welding process will be discussed. Section 2.3 shows that the switching controller can be rewritten in a FLC framework. Section 2.4 will detail the equipment used for this controller. In Sections 2.5 and 2.6 the performance of the developed Fuzzy Logic controllers will be evaluated for penetration control of AA5182 sheets in a butt weld configuration and DX54D-Z sheets in an overlap configuration, respectively. Parts of this work have been published [19].

2.2 General FLC Framework for Laser Welding Control

In this section, the developed FLC [20] for full penetration control during the laser welding process of thin metal sheets will be described. The structure of the applied control system is presented as a block diagram in Figure 2.3.

The top figure schematically shows the closed loop control structure. The sensor dynamics, welding process and laser dynamics are all incorporated in the Plant block. The input of the Plant is the required laser power P. P is the amount of laser power that is calculated by the FLC. This value is passed to the controller of the laser source. The actually delivered laser power will deviate somewhat from P due to the laser source dynamics.

The output of the Plant consists of the photodiode sensor signals $\boldsymbol{S}$ and the welding speed v. This output vector is returned to the FLC, which subsequently recalculates a suitable input for the Plant.

The lower diagram in Figure 2.3 shows the internal structure of the applied FLC. A low pass filter LPF is used for filtering of the photodiode sensor signals $\boldsymbol{S}$. This prevents aliasing and eliminates high frequency process and sensor noises.

The required laser power P is calculated by the FLC by integration over time of a calculated power change $\dot{P}$

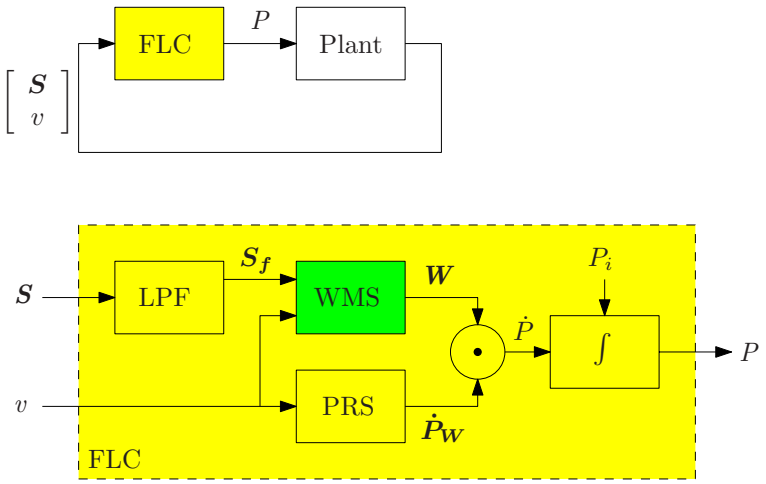

Figure 2.3: *Block diagram of closed loop controlled laser welding process (top) and the Fuzzy Logic Controller (bottom). Note that the* $\odot$ *symbol represents an inner product.*

$$P = \int \dot{P}\, dt, \tag{2.1}$$

where $\dot{P}$ is calculated by the inner product of vector $\boldsymbol{W}$ and $\dot{\boldsymbol{P}}_{\boldsymbol{W}}$

$$\dot{P} = \boldsymbol{W} \cdot \dot{\boldsymbol{P}}_{\boldsymbol{W}}. \tag{2.2}$$

$\dot{\boldsymbol{P}}_{\boldsymbol{W}}$ is a vector which contains a desired change of laser power for every possible welding mode (e.g. "Partial penetration" or "Blowholes"), calculated by the Power Regulator System (PRS). Since the values of $\dot{\boldsymbol{P}}_{\boldsymbol{W}}$ are functions of the welding speed, the PRS has v as input.

The vector $\boldsymbol{W}$ is calculated by the Weld Monitoring System (WMS) and contains as much elements as there are welding modes. These elements can have a value of zero or one, depending on the classified welding mode. By the inner product of $\boldsymbol{W}$ and $\dot{\boldsymbol{P}}_{\boldsymbol{W}}$, $\dot{P}$ receives the desired power change value belonging to the identified welding mode.

2.2 General FLC Framework for Laser Welding Control

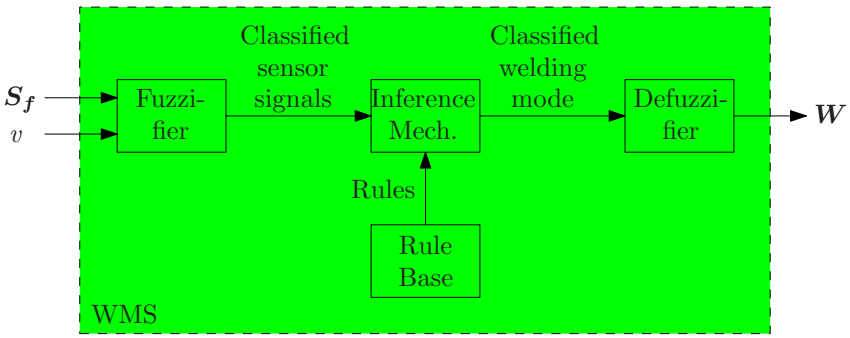

Figure 2.4: *Block diagram of the Weld Monitoring System (WMS).*

The determination of $\boldsymbol{W}$ in the WMS is presented in Figure 2.4, which shows the different parts of the WMS. The functions of these different components are described below [20]:

Rule Base: All the knowledge about how the input signals are linked to specific welding modes (like 'Partial penetration' or 'Conduction welding'), is stored in the Rule Base. This is a set of *IF-THEN* rules that are formulated based on experience of a specialist. For example, in the case of the penetration controller of Postma, one such rule has the following form:

IF sensor signal S_f is 'Low',
THEN the welding mode is 'Partial penetration'. (2.3)

Fuzzifier: The Fuzzifier converts the the numerical signal values S_f and v to fuzzy input values (describing values, rather than numerical inputs). The Fuzzifier uses probability density functions (Membership functions) to determine the appropriate fuzzy values. For instance, in the penetration controller of Postma, $[\boldsymbol{S_f}\ v]^T$ (numerical) can be classified as 'Low' or 'High' (descriptive).

Inference Mechanism: The Inference Mechanism selects the appropriate rules from the Rule Base for the incoming sensor signal. The output of the Inference Mechanism is given by application of the selected rule(s) to the fuzzy input signal(s) provided by the Fuzzifier. In this case the output is again a fuzzy value. For the penetration controller of Postma, such an output can have the values 'Partial penetration' or 'Full penetration'.

Defuzzifier: The Defuzzifier converts the fuzzy output value of the Inference Mechanism to a numerical value, which is used by the controller to calculate the desired laser power P. In the case of the penetration controller, the fuzzy value 'Partial penetration' is converted to $\boldsymbol{W} = [1\ 0]^T$ and the value 'Full penetration' gives $\boldsymbol{W} = [0\ 1]^T$.

In the following section, how the Switching Controller of Postma can be re-written in the FLC framework will be shown.

2.3 The Switching Controller in the FLC Framework

For a good understanding, in this section the switching controller developed by Postma and de Graaf [16, 17, 18] is treated in detail for the Nd:YAG laser welding process of 0.75 mm FeP04 sheets in a butt weld configuration. This controller was re-written in the FLC framework explained in Section 2.2, the details of which are provided in the forthcoming sections.

2.3.1 The Switching Controller

The setup shown schematically in Figure 2.1 is very similar to the setup used for development and testing of the switching controller. For this controller, the Weldwatcher (WW) photodiode system was used, which is positioned at Position 3 in Figure 2.1. Figure 2.5 shows the low-pass filtered WW photodiode signal S_f as a function of the laser power P for a welding speed of 140 mm/s. The graph shows that during the partial penetration welding

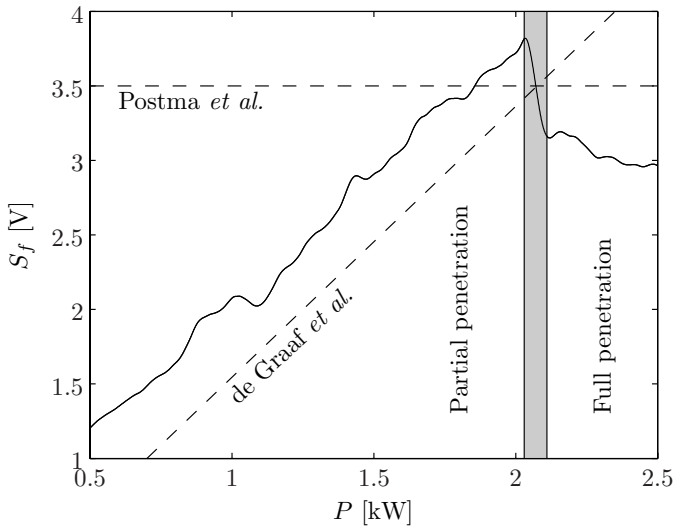

Figure 2.5: *The filtered WW signal S_f as a function of the required laser power P, using v = 140 mm/s for 0.75 mm FeP04 sheets in a butt weld configuration [18]. The gray area indicates the transition region between partial and full penetration and the dashed lines are the reference values used by Postma and de Graaf, respectively.*

mode, the sensor signal is approximately proportional with the laser power, up to about 2.0 kW. At this point, the keyhole starts to fully penetrate the sheet, which results in a drop in the sensor signal. A further increase of the laser power has almost no effect on the signal level. The gray area in Figure 2.5 indicates the transition zone between the partial and full penetration welding modes.

The drop in S_f is used by the switching controller to calculate an appropriate value of the desired laser power P. The goal of this controller is to maintain full penetration keyhole welding, using a minimum of laser power. The output of this controller is the desired laser power P. The appropriate value of P is calculated using a PI-controller

$$P = \begin{cases} -K_{p\uparrow}e + \int K_{i\uparrow}\ dt + P_i & \text{for} \quad e > 0, \\ -K_{p\downarrow}e + \int K_{i\downarrow}\ dt + P_i & \text{for} \quad e \leq 0, \end{cases} \tag{2.4}$$

where

$$e = S_f - S_t. \tag{2.5}$$

Here S_t is a reference or threshold value. Note that Postma defined S_t as a constant threshold level, which is independent of the laser power P. De Graaf defined S_t as a linear function of the laser power P (Figure 2.5). The latter has the advantage that it results in a controller [18] that can direct the laser welding process towards full penetration keyhole welding even when the laser power is very low. If for instance the laser power has a value of 1.5 kW, the controller of Postma will falsely identify the welding mode as full penetration and will subsequently lower the laser power. However the controller of de Graaf will correctly identify this welding mode as partial penetration and will increase the required laser power.

The values of the tuning parameters are dependent on the value of e. If $e \leq 0$ (in other words $S_f < S_t$), the process is in the full penetration welding mode. In this case $K_{p\downarrow}$ and $K_{i\downarrow}$ are used. In order to minimise the amount of laser power, the value of P is decreased slowly. De Graaf demonstrated that good results can be obtained using values of 0.5 kW and -4 kW/s for $K_{p\downarrow}$ and $K_{i\downarrow}$, respectively.

If during this decrease of P the process reaches the border between full and partial penetration, S_f will rise quickly, which results in $e > 0$. When e becomes positive, the controller replaces the previous tuning parameters with the new values $K_{p\uparrow}$ and $K_{i\uparrow}$, that in turn increase P quickly (de Graaf uses $K_{p\uparrow} = 0$ kW and $K_{i\uparrow} = 20$ kW/s). This increase of P is fast enough to prevent loss of penetration by the melt pool and results again in a drop in the sensor signal, changing again the sign of e. When e changes sign again, the controller switches back to $K_{p\downarrow}$ and $K_{i\downarrow}$, which slowly decreases P. This cycle is repeated during the entire welding process.

2.3.2 Reformulation of the Switching Controller

For the formulation of the switching controller in the FLC framework, the WW sensor signal is compared with a reference value S_t, which is a linear function of P (as considered by de Graaf)

$$S_t = a_2 P + a_1. \tag{2.6}$$

For most practical situations, $|a_1| << |a_2 P|$. Therefore, a_1 can be neglected, which gives

$$S_t = a_2 P. \tag{2.7}$$

Comparing S_f with S_t, is identical to comparing $S_f^* = S_f/P$ with $S_t^* = S_t/P = a_2$. Figure 2.6, shows S_f^* for different values of P. In this figure, the transition region between the 'High' sensor values (which corresponds to partial penetration of the weld) and the 'Low' sensor values (which corresponds to full penetration) is indicated with the gray area. The width of this transition zone was determined from a visual examination of the welded samples.

In the FLC framework, the input of the FLC controller is $[S^* \ v]^T$, where S^* is the WW sensor signal divided by the laser power and v is the welding speed. Subsequently S^* is low-pass filtered by the LPF (Figure 2.3). The output of the low-pass filter S_f^*, is directed to the WMS, where it is first converted to a fuzzy value by the Fuzzifier. When $S_f^* > S_t^*$, which also means that $S_f > S_t$, the Fuzzifier outputs the fuzzy value 'High'. Otherwise, the Fuzzifier output is 'Low'. The membership functions for the fuzzy values 'Low' and 'High' are given in Figure 2.7.

The Inference Mechanism selects and applies the appropriate IF-THEN rules from the Rule Base (Equation 2.8). The output of the Inference Mechanism is the fuzzy value 'Partial penetration' or 'Full penetration'.

IF S_f is 'High', THEN The welding mode is 'Partial penetration'.
IF S_f is 'Low', THEN The welding mode is 'Full penetration'.
(2.8)

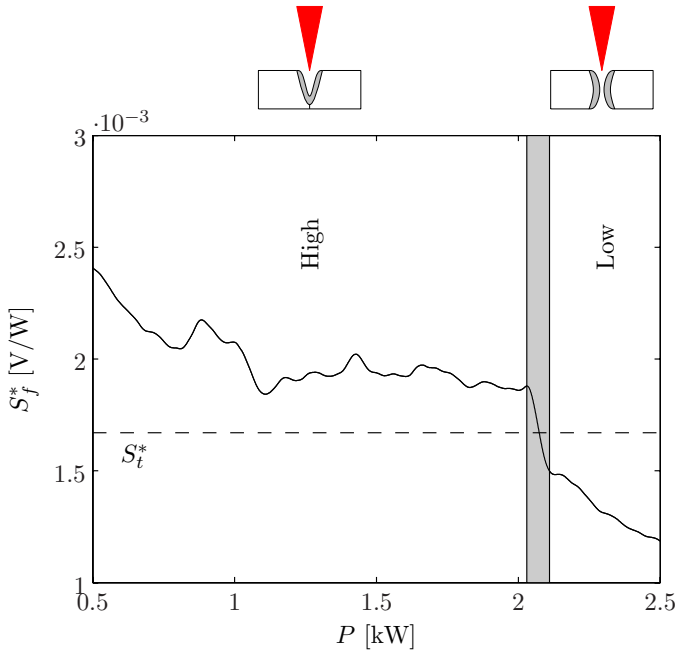

Figure 2.6: *The filtered WW signal divided by the laser power $S_f^* = S_f/P$ as a function of the required laser power P, using $v = 140$ mm/s for FeP04. The gray area indicates the transition region between partial and full penetration and the dashed line is reference value $S_t^* = S_t/P$.*

The Defuzzifier converts this fuzzy value to a numerical output $\boldsymbol{W}$, according to Equation 2.9.

$$\begin{aligned} &\textit{For 'Partial penetration',} \quad \boldsymbol{W} = [1\ 0]. \\ &\textit{For 'Full penetration',} \quad \boldsymbol{W} = [0\ 1]. \end{aligned} \tag{2.9}$$

The laser power change vector $\dot{\boldsymbol{P}}_{\boldsymbol{W}}$, which contains appropriate laser power changes for both possible welding modes ('Partial penetration' and 'Full penetration'), is calculated by the PRS in the following way

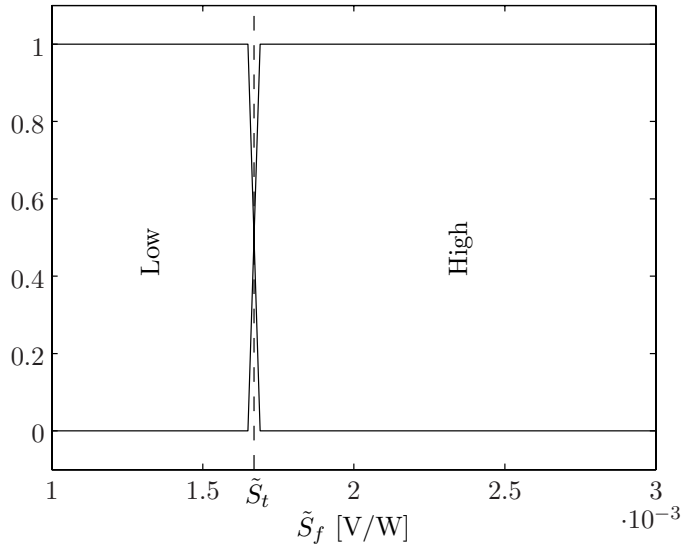

Figure 2.7: *The membership functions for FeP04.*

$$\dot{\boldsymbol{P}}_{\boldsymbol{W}} = \begin{bmatrix} \dot{P}_{W1} \\ \dot{P}_{W2} \end{bmatrix} = \begin{bmatrix} -K_{p\uparrow} & K_{i\uparrow} \\ -K_{p\downarrow} & K_{i\downarrow} \end{bmatrix} \begin{bmatrix} \dot{e} \\ 1 \end{bmatrix}, \tag{2.10}$$

where $\dot{e} = d/dt(\tilde{S}_f - \tilde{S}_t)$. It should be emphasised that for this controller, $\dot{e}$ should be added as an additional input for the PRS block in Figure 2.3.

The values of $K_{p\uparrow}$, $K_{i\uparrow}$, $K_{p\downarrow}$ and $K_{i\downarrow}$ are identical to those used in Section 2.3.1. The output P of the FLC can now be calculated using Equation 2.11

$$
\begin{aligned}
P &= \int \boldsymbol{W} \cdot \dot{\boldsymbol{P}}_{\boldsymbol{W}}\, dt \\
&= \int \begin{bmatrix} W_1 & W_2 \end{bmatrix} \begin{bmatrix} -K_{p\uparrow} & K_{i\uparrow} \\ -K_{p\downarrow} & K_{i\downarrow} \end{bmatrix} \begin{bmatrix} \dot{e} \\ 1 \end{bmatrix} dt \\
&= \int \Big(W_1 \left(-K_{p\uparrow}\dot{e} + K_{i\uparrow}\right) + W_2 \left(-K_{p\downarrow}\dot{e} + K_{i\downarrow}\right) \Big) dt \\
&= -W_1 K_{p\uparrow} e + W_1 \int K_{i\uparrow}\, dt - W_2 K_{p\downarrow} e + W_2 \int K_{i\downarrow}\, dt + P_i.
\end{aligned}
\tag{2.11}
$$

When the WMS identifies the process as 'Partial penetration', $W_1 = 1$ and $W_2 = 0$. When the process is in the 'Full penetration' welding mode, $W_1 = 0$ and $W_2 = 1$ (Equation 2.9). This gives

$$
P = \begin{cases} -K_{p\uparrow} e + \int K_{i\uparrow}\, dt + P_i & \text{when} \quad W = [1\ 0] \\ \\ -K_{p\downarrow} e + \int K_{i\downarrow}\, dt + P_i & \text{when} \quad W = [0\ 1] \end{cases}
\tag{2.12}
$$

This relation is identical to the output of the switching controller, given in Equation 2.4.

2.4 Experimental Setup FLC System

To verify the performance of the FLC systems, tests were performed under various circumstances. Figure 2.1 on page 14 gives a schematic view of the setup used, which is very similar to the setup of Postma and de Graaf. The different components of this setup are detailed in this section.

The experiments were carried out using a 4 kW Trumpf THL4006D industrial Nd:YAG laser [21], with a wavelength of 1064 nm (Figure 2.8). This laser is connected to an optical fiber with a core diameter of 0.6 mm. The laser light is projected on the workpiece using a standard Trumpf BEO D70 welding head with a 200 mm collimator lens and a 150 mm focus lens, which results in a focal diameter of 0.45 mm (Figure 3.1). The laser beam

2.4 Experimental Setup FLC System

Figure 2.8: *Photo of the Trumpf THL4006D industrial Nd:YAG laser.*

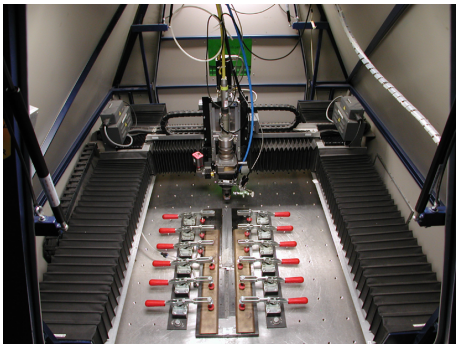

Figure 2.9: *Photo of the gantry manipulator (Courtesy of J. Veenstra).*

has a top-hat intensity distribution in the focal plane. The welding head is moved over the workpiece using a gantry manipulator (Figure 2.9). During the welding process, Ar gas is used for shielding both the top and bottom of the workpiece, using gas flow rates of 22.7 l/min and 5.7 l/min respectively.

The dichroic mirror inside this welding head is used to direct the process light to a system of three photodiodes (position 2 in Figure 2.1). The photodiodes are part of the commercially available Laser Weld Monitor (LWM) system [10, 22, 23, 24] developed by Jurca Optoelectronik GmbH, now part of the Precitec Group [25]. In Figure 2.10 a photo is shown of the LWM system attached to the Trumpf welding head.

The LWM system consists of three photodiodes, each with a different spectral sensitivity. The Jurca P photodiode is sensitive in the wavelength range of 400 to 600 nm (visible light). The Jurca T diode is sensitive to IR process emissions in the range of 1100 to 1800 nm. The third diode, Jurca R, measures the back reflected Nd:YAG radiation (1064 nm). These sensors have a coaxial FOV of about 18 mm in diameter [17].

In addition, a second commercial photodiode-based monitoring system known as the Weldwatcher (WW) system, developed by Laser Zentrum Hannover eV [26, 27] and commercialised by 4D GmbH [28], was also used. This photodiode system is placed in the Nd:YAG laser source housing (po-

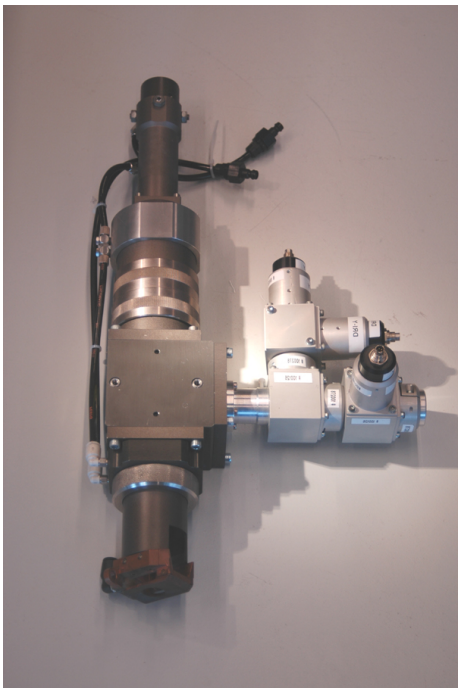

Figure 2.10: *Photo of the LWM sensors attached to the BEO D70 Trumpf laser welding head.*

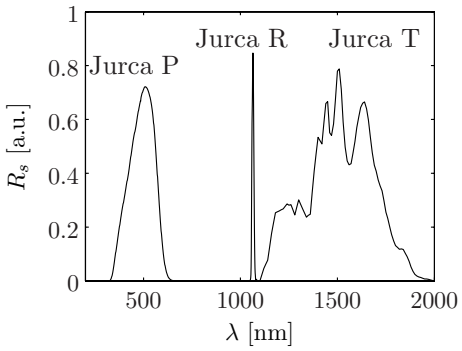

Figure 2.11: *Spectral response of the LWM sensors [17].*

sition 3 in Figure 2.1). It measures the optical emission wavelengths around 360 and 750 nm, back reflected through the beam delivery fiber. Due to this reason, the sensor has a much smaller FOV than the LWM system, and is approximately 0.3 to 0.5 mm in diameter and is placed coaxial with the Nd:YAG laser beam [17]. A neutral density optical filter (Schott NG 5) was placed in front of the the WW sensor to prevent saturation. This filter has a transmittance of about 0.4 for 360 nm and 0.6 for 750 nm.

Figure 2.12: *Photo of the Weldwatcher sensor.*

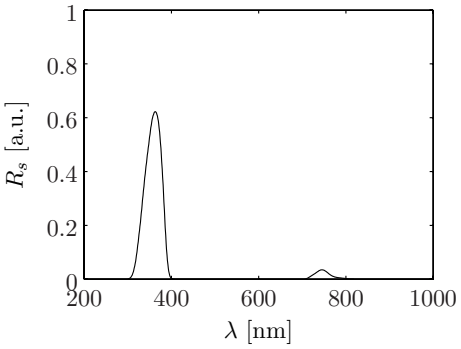

Figure 2.13: *Spectral response of the Weldwatcher sensor [17].*

2.5 Implementation of FLC for Aluminium

The FLC system is implemented and tested for welding of 1.1 mm AA5182 sheets in a butt weld configuration. This configuration is typical for the production of aluminium TWB's. Using the experimental setup described in the previous section, calibration experiments were performed to investigate the relationship between the photodiode sensor signals (three from the LWM system and one from the WW system) and the resulting weld quality. This is done by ramping the laser power during welding process and simultaneously recording the sensor signals. Subsequently, the resulting weld bead is visually examined. The weld penetration is compared and correlated to the four photodiode sensor signals.

2.5.1 FLC Framework

There seems to exist a correlation between the WW photodiode sensor signal and the welding mode. The LWM photodiode signals show no clear correlation with the welding mode. Hence, it was decide to use only the WW signal to monitor the aluminium welding process. Figure 2.14 shows

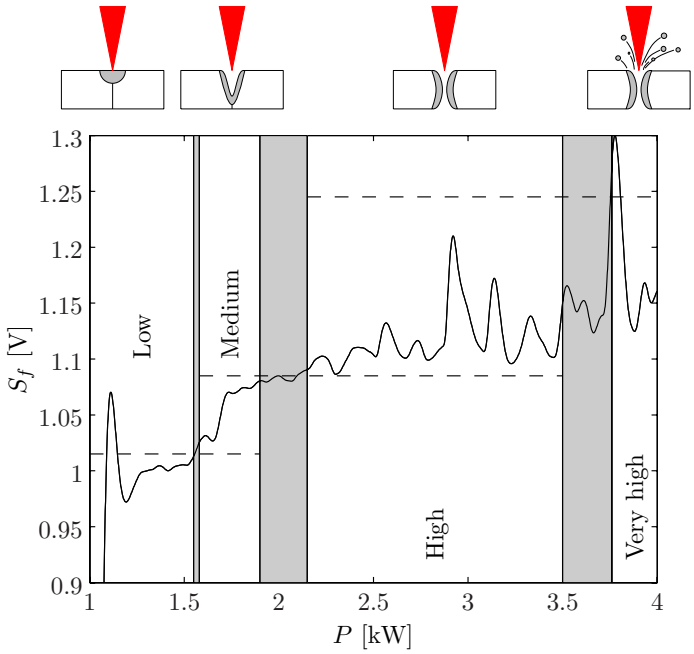

Figure 2.14: *The filtered WW signal S_f as a function of the required laser power P, using $v = 140$ mm/s for welding of AA5182 sheets.*

the low-pass filtered WW signal S_f as a function of the laser power P. In this figure, the different welding modes, which are identified from the resulting weld bead appearences, are indicated. The gray area indicate the transitional regions.

Filtering of the sensor signal is performed using an analog low-pass filter to prevent anti-aliasing and a digital third order low-pass Butterworth filter with a cutoff frequency of 15 Hz, to eliminate process and sensor noises. The corresponding weld quality are indicated schematically in the figure. These experiments are conducted with welding speeds of 70, 140 and 200 mm/s.

At first, the content of the Fuzzifier has to be determined. This Fuzzifier transforms the filtered sensor signal value S_f to a fuzzy value, describing

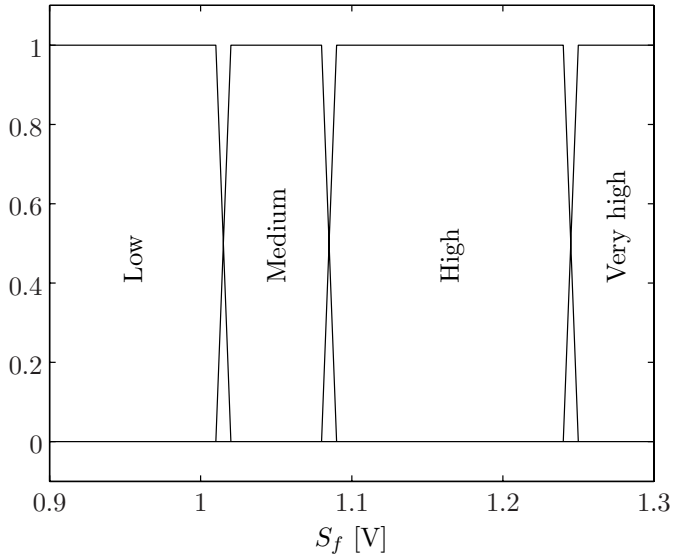

Figure 2.15: *The membership functions for AA5182.*

the sensor signal. In Figure 2.14, four different sensor value ranges can be distinguished: 'Low', 'Medium', 'High' and 'Very high'. For the experiments with the ramped laser power, the transition between the different welding states is not sharp and cannot be linked to a fixed laser power value. Instead they are related to a laser power intervals. These transition ranges are indicated in Figure 2.14 by the gray areas.

In Figure 2.15 the probability density functions or membership functions of the different sensor signal values are given as a function of S_f. Using these membership functions, the Fuzzifier gives the appropriate fuzzy value to the Inference Mechanism.

In the Rule Base it is defined which weld quality is expected for a certain WW signal level. The Inference Mechanism uses the Rule Base to evaluate the weld quality based on the current fuzzy WW signal value. The Rule Base is given in Equations 2.13.

$$\begin{array}{lll} \textit{IF } S_f \textit{ is 'Low',} & \textit{THEN} & \textit{The welding mode is 'Conduction welding'.} \\ \textit{IF } S_f \textit{ is 'Medium',} & \textit{THEN} & \textit{The welding mode is 'Partial penetration'.} \\ \textit{IF } S_f \textit{ is 'High',} & \textit{THEN} & \textit{The welding mode is 'Full penetration'.} \\ \textit{IF } S_f \textit{ is 'Very high',} & \textit{THEN} & \textit{The welding mode is 'Blow holes'.} \end{array} \tag{2.13}$$

Therefore, the output of the Inference Mechanism has one of the fuzzy values 'Conduction welding', 'Partial penetration', 'Full penetration' or 'Blow holes', corresponding to Fuzzifier outputs 'Low', 'Medium', 'High' and 'Very high', respectively. These fuzzy values are converted to numerical values by the Defuzzifier. The output of this Defuzzifier is vector $\boldsymbol{W}$. In Equation 2.14, $\boldsymbol{W}$ is given for each possible output value of the Inference Mechanism.

$$\begin{array}{ll} \textit{For 'Conduction welding',} & \boldsymbol{W} = [1\ 0\ 0\ 0]. \\ \textit{For 'Partial penetration',} & \boldsymbol{W} = [0\ 1\ 0\ 0]. \\ \textit{For 'Full penetration',} & \boldsymbol{W} = [0\ 0\ 1\ 0]. \\ \textit{For 'Blow holes',} & \boldsymbol{W} = [0\ 0\ 0\ 1]. \end{array} \tag{2.14}$$

To calculate the appropriate FLC controller output P, the WMS output $\boldsymbol{W}$ is multiplied with the output of the PRS $\dot{\boldsymbol{P}}_{\boldsymbol{W}}$ using an inner product (Figure 2.3). Figure 2.16 shows how $\dot{\boldsymbol{P}}_{\boldsymbol{W}}$ depends on the welding speed v. The outcome of this inner product is subsequently integrated over time, as indicated in Equation 2.11, to obtain the desired laser power P.

2.5.2 Controller Tests

Several experimental tests were carried out to evaluate the performance of the developed controller. In the first test, the initial laser power was set to 1 kW, using a welding speed of 140 mm/s and the FLC controller disabled to start with. This results in a conduction weld. After 0.2 s, the FLC controller is enabled. Figures 2.17(a) and 2.18(a) show the values of P and S_f during this test. This shows that the controller immediately increases

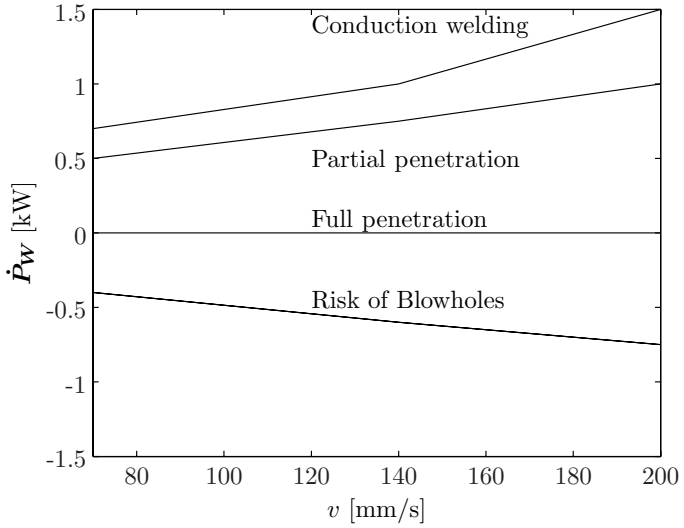

Figure 2.16: *The elements of the output of the PRS, as a function of v for welding of AA5182.*

P in an effort to reach full penetration keyhole welding. This also results in an increase of the Weldwatcher signal. The controller output stabilises around 3.2 kW, which results in a good weld quality. During welding, the Weldwatcher signal slowly decreases after reaching a maximum. Such a decrease was not seen during bead-on-plate experiments. It is probably due to the thermal distortion of the welding plates during welding. These distortions cause a small widening of the gap between the plates, which increases as welding progresses. At $t = 1.36$ s, this signal decrease causes the controller to increase the laser power. This has no visible effect on the resulting weld bead quality.

In the second situation, the initial power is set to 4 kW, at a welding speed of 140 mm/s (Figures 2.17(b) and 2.18(b)). With use of these settings, there is an increased risk of blow hole formation. However, the Weldwatcher signal remains below the critical level and, when the controller is enabled after 0.2 s, the controller output is not altered immediately. Only

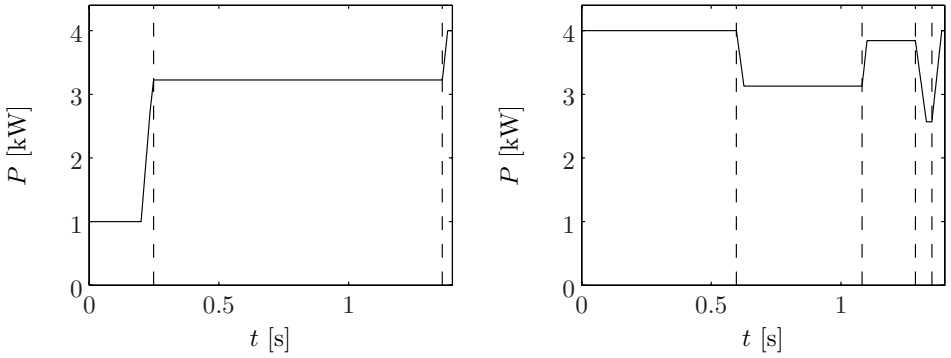

(a) First performance test. (b) Second performance test.

Figure 2.17: *The required laser power P during the performance tests of the controller for AA5182.*

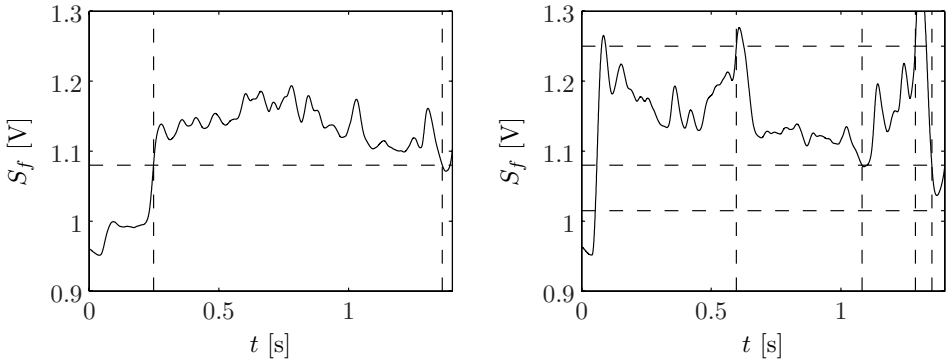

(a) First performance test. (b) Second performance test.

Figure 2.18: *The filtered WW signal S_f during the performance tests of the controller for welding of AA5182 sheets. The vertical dashed lines indicate the time instances when the controller adjusts P and the horizontal dashed lines indicate the threshold value of the sensor signal.*

after 0.6 s the controller corrects the laser power somewhat. The fluctuating laser power values around $t = 0.6$ s and 1.3 s are believed to be caused by strong keyhole wall fluctuations. Furthermore, the sensor signal has a tendency to decrease while the laser power remains constant, which is probably due to the thermal distortions of the sheets.

The performance tests indicate that, when the control parameters are properly tuned, the controller is well able to control and maintain the process in the full penetration keyhole welding mode. However, this system has a serious drawback. Experiments investigating the robustness of this system reveal that it is very sensitive for changes in environmental conditions. Even a small change in the shielding gas supply affects the sensor signal to a large extent. Since these changes are inevitable in an industrial environment, this system is less suitable for industrial implementation. A camera-based system might be a better alternative in this situation. Chapter 3 describes such a camera-based monitoring system, which can be used as a basis for a camera-based process controller.

2.6 Implementation of FLC for Zinc Coated Steel

The developed FLC framework was also tested for the penetration control of two 0.8 mm DX54D-Z GI (zinc coated steel) sheets, welded in an overlap configuration with a preset gap between the sheets of approximately 0.1 mm. Such overlap configuration is often used in the automotive industry. Calibration experiments were performed to determine the sensor signals for each welding mode. This was repeated for various welding speeds. During welding, the laser power was ramped and the resulting weld bead quality was visually examined. Subsequently the weld bead appearance was compared with the four photodiode sensor signals, which is described in the next section.

2.6.1 FLC Framework

Comparison of the weld bead and the sensor signals shows that the welding mode can possibly be determined based on two sensor signals: the WW

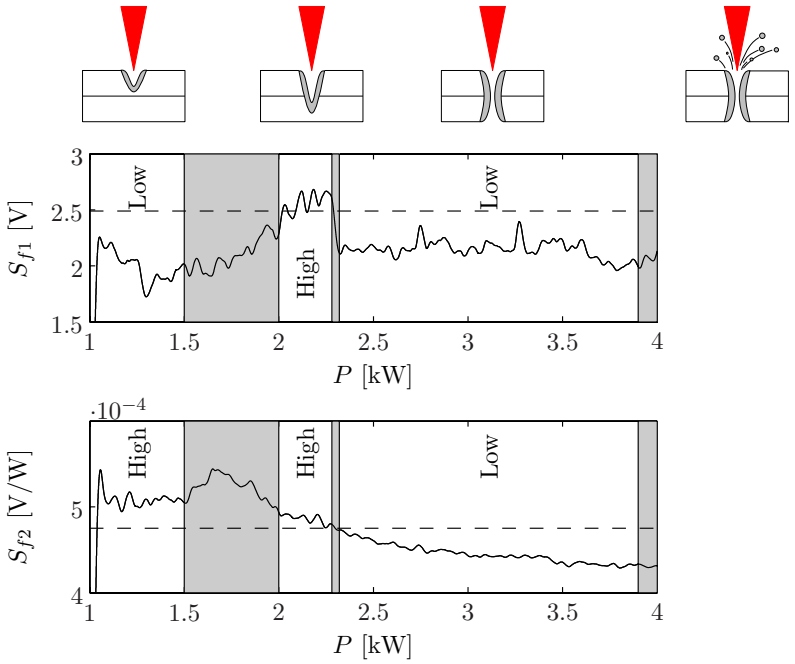

Figure 2.19: *The filtered Weldwatcher signal (S_{f1}) and the filtered Jurca R signal divided by P (S_{f2}) as a function of the required laser power P for welding of DX54D-Z GI sheets.*

signal and the Jurca R signal, divided by the laser power. Figure 2.19 shows these signals recorded during the calibration experiments for a welding speed of 70 mm/s. The input $\boldsymbol{S_f}$ of the WMS (Figure 2.4 on page 19) has the following form

$$\boldsymbol{S_f} = \begin{bmatrix} S_{f1} \\ S_{f2} \\ v \end{bmatrix}. \tag{2.15}$$

The WW sensor signal (S_{f1}) and the Jurca R signal divided by the laser

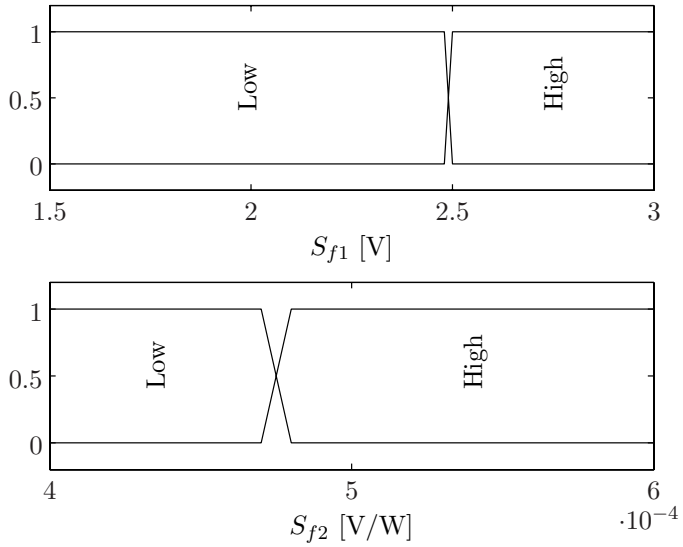

Figure 2.20: *The membership functions for welding of DX54D-Z GI sheets.*

power (S_{f2}) are filtered using an analog low-pass filter to prevent anti-aliasing and a digital third order low-pass Butterworth filter with a cutoff frequency of 15 Hz to eliminate process and sensor noises. The gray areas indicate the transition regions between the different welding modes. These calibration experiments were carried out using welding speeds of 30, 70 and 100 mm/s.

In the WMS, the numerical sensor signals $\boldsymbol{S_f}$ are at first transformed to fuzzy values. Both S_{f1} and S_{f2} can have two possible values: 'High' or 'Low'. The Fuzzifier assigns these values to S_{f1} and S_{f2} using the membership functions given in Figure 2.20. These values are subsequently passed on to the Inference Mechanism.

The knowledge about how the sensor signals are coupled to the different welding modes is stored in the Rule Base (Equation 2.16). The output of the Inference Mechanism is a fuzzy value that can have the values: 'Par-

tial penetration of top sheet', 'Partial penetration of bottom sheet', 'Full penetration' or 'Blow holes'.

$$\begin{array}{lll}
\textit{IF } S_{f1} \textit{ is 'Low' AND } S_{f2} \textit{ is 'High', THEN} & \textit{The welding mode is 'Partial penetration of top sheet'.} \\
\textit{IF } S_{f1} \textit{ is 'High' AND } S_{f2} \textit{ is 'High', THEN} & \textit{The welding mode is 'Partial penetration of bottom sheet'.} \\
\textit{IF } S_{f1} \textit{ is 'Low' AND } S_{f2} \textit{ is 'Low', THEN} & \textit{The welding mode is 'Full penetration'.} \\
\textit{IF } S_{f1} \textit{ is 'High' AND } S_{f2} \textit{ is 'Low', THEN} & \textit{The welding mode is 'Blow holes'.}
\end{array} \tag{2.16}$$

The Defuzzifier converts the fuzzy output value of the Inference Mechanism to a numerical value of $\boldsymbol{W}$ as given in Equation 2.17

$$\begin{array}{ll}
\textit{For 'Partial penetration of top sheet',} & \boldsymbol{W} = [1\ 0\ 0\ 0]. \\
\textit{For 'Partial penetration of bottom sheet',} & \boldsymbol{W} = [0\ 1\ 0\ 0]. \\
\textit{For 'Full penetration',} & \boldsymbol{W} = [0\ 0\ 1\ 0]. \\
\textit{For 'Blow holes',} & \boldsymbol{W} = [0\ 0\ 0\ 1].
\end{array} \tag{2.17}$$

The FLC output P can be calculated by multiplying the WMS output $\boldsymbol{W}$ with the output of the PRS $\dot{\boldsymbol{P}}_{\boldsymbol{W}}$, using an inner product. $\dot{\boldsymbol{P}}_{\boldsymbol{W}}$ is a function of the welding speed, as shown in Figure 2.21.

2.6.2 Controller Tests

To test the controller performance while overlap welding of DX54D-Z GI sheets, the system was subjected to several performance tests. In these performance tests, a different welding head is used due to practical reasons. The coating of lenses of this new welding head is different from the welding head used in the previous experiments. This also influences the absolute value of S_{f1} and S_{f2} during welding, although the shape of the signals is not influenced. Therefore, the transitions between 'High' and 'Low' in the

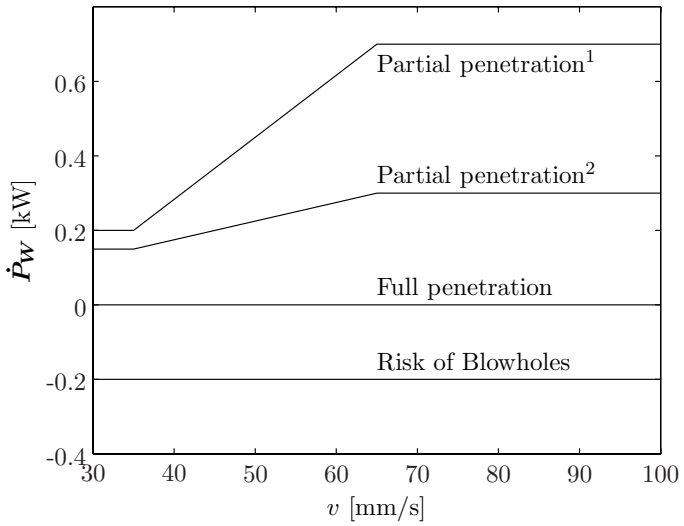

Figure 2.21: *The elements of the output of the PRS, as a function of v for the welding of DX54D-Z GI sheets.*

[1]Partial penetration of the top plate
[2]Partial penetration of the bottom plate

membership functions given in Figure 2.20 has been adapted to this new situation.

In the first test, the initial laser power is set to 1 kW (Figure 2.22(a)), resulting in a weld that partially penetrates the top sheet. After 0.2 seconds, the controller is enabled, which immediately detects the partial penetration through the Weldwatcher and the Jurca R sensor signals (Figure 2.23(a)). In a response, the controller increases the laser power, as can be seen in Figure 2.22(a). Around $t = 0.9$ s, the laser power stabilises around 2.9 kW. In this situation, the keyhole fully penetrates the two sheets. After 1.7 s, the Weldwatcher signals shows a peak which causes the controller to slightly decrease the laser power. After 2.1 s a peak in the Jurca R divided by the laser power signal causes a small increase in the laser power setpoint. Both changes have no influence on the resulting weld quality.

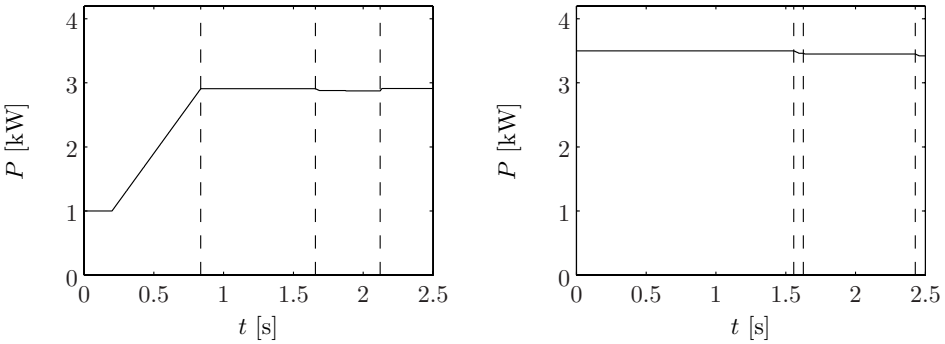

(a) First performance test (b) Second performance test

Figure 2.22: *The required laser power P during the performance tests of the controller for welding of DX54D-Z GI sheets.*

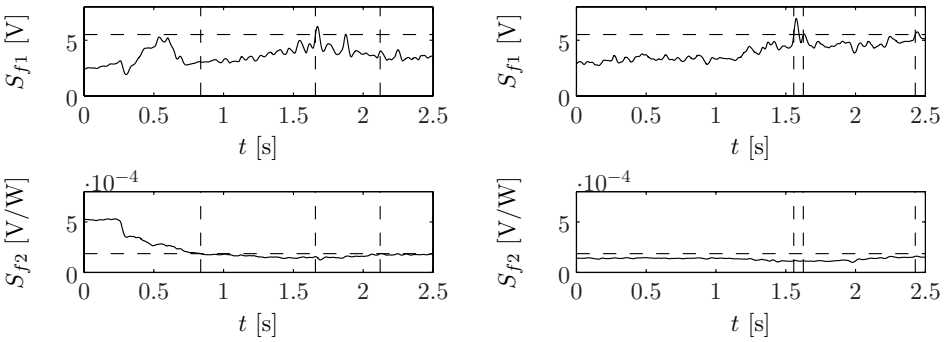

(a) First performance test (b) Second performance test

Figure 2.23: *The signals S_{f1} and S_{f2} obtained during the performance tests of the controller for welding of DX54D-Z GI sheets. The vertical dashed lines indicate the time instances when the controller adjusts P and the horizontal dashed lines indicate the threshold values of the sensor signals.*

2.6 Implementation of FLC for Zinc Coated Steel

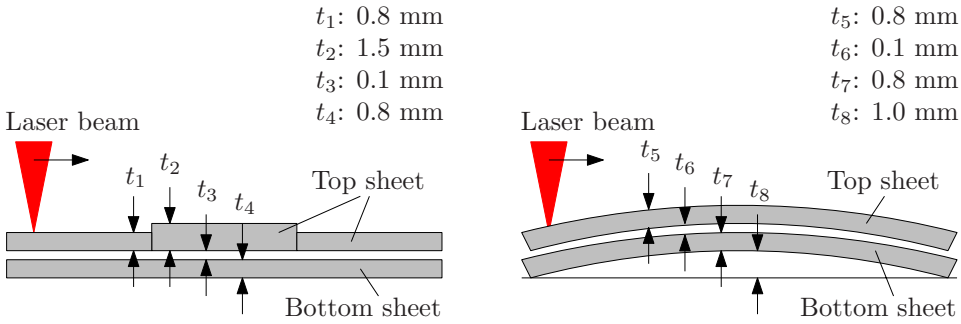

(a) First robustness test (b) Second robustness test

Figure 2.24: *Schematic cross section along the weld seam of the workpiece used with the robustness tests.*

In a second performance test case, the laser power setpoint is set to 3.5 kW at $t = 0$. Again, after 0.2 s the controller is enabled. The controller correctly classifies the process as being 'Full Penetration' and maintains the current laser power setpoint. Only at 1.6 s and 2.4 s, the Weldwatcher signal level is classified as 'High', which results in a slight decrease in the required laser power. The resulting weld quality is good for the entire laser weld.

Also the robustness of the closed loop system was tested. In the first robustness test, the thickness of the top sheet is varied in steps along the length of the weld. Figure 2.24(a) shows a schematic cross section of the workpiece along the weld seam. For this test, a welding speed of 30 mm/s is used. The initial laser power is set to 1.5 kW. After 0.2 s, the controller is activated.

Figure 2.25(a) and 2.26(a) show the required laser power P and the sensor signals S_{f1} and S_{f2} respectively. When the controller is activated after 0.2 s, the laser beam is over the first 0.8 mm thick top sheet (Figure 2.24(a)). The laser power is increased and fluctuates somewhat between 2.1 and 2.7 kW, resulting in a stable full penetration welding process. Between $t = 2.4$ s and $t = 4.1$ s, the laser beam passes over the 1.5 mm top sheet. The thicker sample requires more laser power to be fully penetrated. This

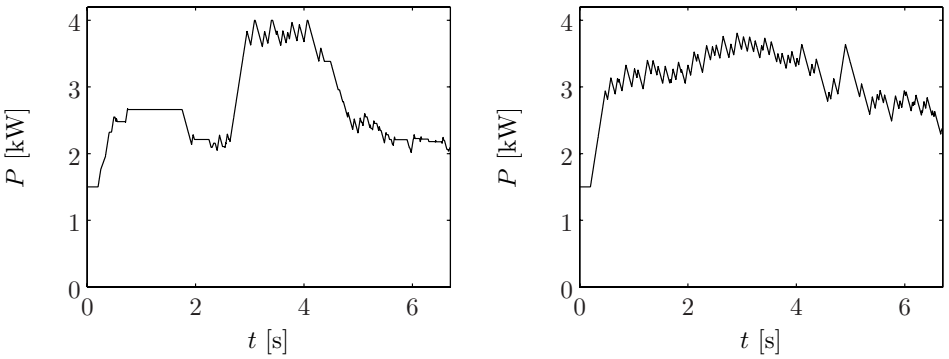

(a) First robustness test. (b) Second robustness test.

Figure 2.25: *The required laser power P during the robustness tests of the controller for DX54D-Z.*

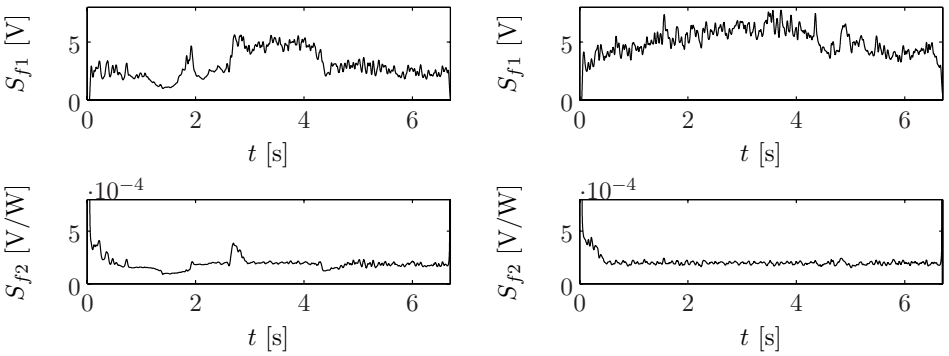

(a) First robustness test. (b) Second robustness test.

Figure 2.26: *The signals S_{f1} and S_{f2} during the robustness tests of the controller for DX54D-Z.*

is detected by the controller, which increases the laser power setpoint to about 3.8 kW in an effort to maintain full penetration. The resulting weld bead is fully penetrated over the entire length of the weld, without any blowholes. This test was repeated for various welding speeds, all showing similar results.

In a second robustness test, the weld sample is bent to simulate a shift in the focus position of the Nd:YAG laser beam relative to the workpiece (Figure 2.24(b)). At the start and end positions of the weld, the laser is at focus on the sample surface. In the middle part of the weld, the laser is out of focus. Again the controller was activated after 0.2 s, starting with a laser power of 1.5 kW. A welding speed of 30 mm/s was used.

During the first three seconds, the laser spot increases in size due to the deformation of the sample. This decreases the irradiance of the laser light at the top surface, which results in a decreased penetration of the keyhole. In a reaction, the controller increases the laser power (Figure 2.25(b)). In the second part of this weld, when the sample surface comes in focus again, the controller slowly decreases the laser power.

Experimental results show that this control system, when properly tuned, is well able to control the welding process towards full penetration keyhole welding. Different test cases show that the system can maintain full penetration keyhole welding under various disturbances, like thickness variations and changes in the focal position relative to the workpiece surface. Although changes in the setup do influence the absolute value of the sensor signals, the signal trend is not affected, as was the case for the control system for the butt welding of AA5182 sheets. This control setup is therefore well suited for implementation in an industrial environment.

2.7 Conclusions

- For the production of Tailor Welded Blanks, it is important that the welds fully penetrate the sheets. A control system that can guarantee full penetration laser welding under all circumstances is of considerable importance and need. The presented FLC control architecture

can translate human operator knowledge into useful control statements.

- The switching controller, which was developed by Postma for the penetration control for the laser welding process of mild steel, can also be written in the developed FLC framework. Therefore, the described FLC system is also well suited for the penetration control of mild steel sheets in a butt weld configuration.
- Performance tests with the FLC system show that it works for penetration control of laser welding of aluminium sheets in a butt weld configuration. However, the system is not robust for environmental changes like shielding gas flow rate variations. For this process, a camera-based system may be a better solution, since this will provide spatial information of the welding process.
- The FLC system is also tested for welding of zinc coated steel sheets in an overlap configuration. These tests show that the penetration during welding can be guaranteed, even in the presence of external disturbances. The developed penetration controller for zinc coated steel sheets is therefore well suited for implementation in an industrial environment.

Chapter 3

Camera-Based Monitoring of Laser Welding

To monitor the laser welding process, a camera-based monitoring system has certain advantages over a photodiode-based system. In contrast with photodiodes, a camera system offers spatial information of the welding process. For an optimal camera system design, it is important to know the spectral content of the light emitted during welding. Therefore, spectral measurements of the laser welding process will be described in Section 3.1. In Section 3.2, the monitoring system is presented, which can make high quality in-situ recordings of the welding area. At the end of this chapter, the most important conclusions are summarised. Parts of the work described in this chapter have been published earlier [29, 30, 31, 32].

3.1 Optical Process Emissions

The laser welding process can be monitored in different ways [1, 33]. In this chapter, camera-based optical sensors are investigated because of their availability, high speed and the possibility to acquire spatially resolved process information.

It is preferred to have a camera system that is mounted on the welding

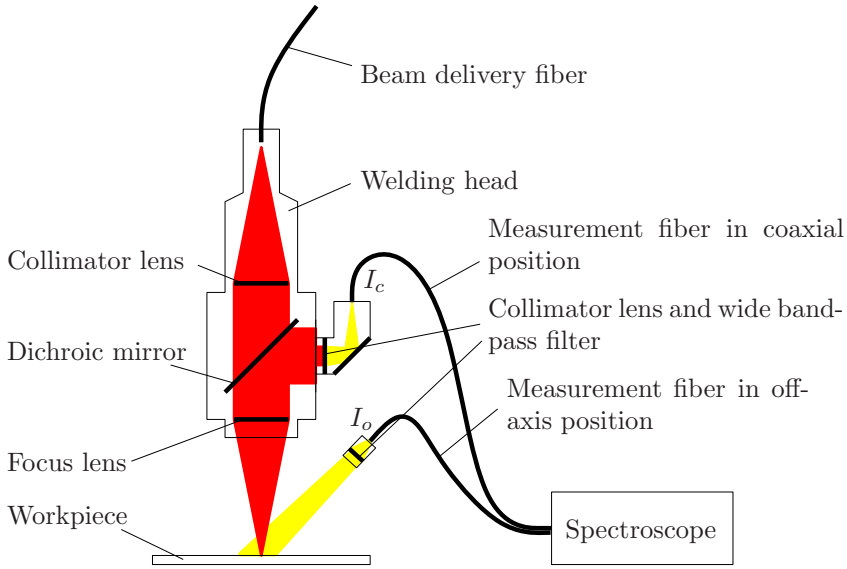

Figure 3.1: *Schematic overview of measurement setup for the spectral measurements.*

head, is focussed on the top surface of the sheet and has a coaxial view of the welding process (position 2 in Figure 2.1). In this way the monitoring system can be compact, and offers the possibility to view into the keyhole. The coaxial view is achieved using the dichroic mirror in the parallel beam inside the welding head (Figure 3.1), which is also used by the photodiode sensor systems described in Chapter 2.

For an optimal design this sensor system, it is important to know the spectrum of the light emitted by the welding process I_o, which is measured in the off-axis position, and of the light reaching the detector I_c, which is measured in the coaxial measurement position (Figure 3.1). Since the emissions heavily depend on the material composition and the welding parameters, spectroscopic measurements are performed under typical welding conditions.

Light emitted by the laser welding process has different sources (Figure

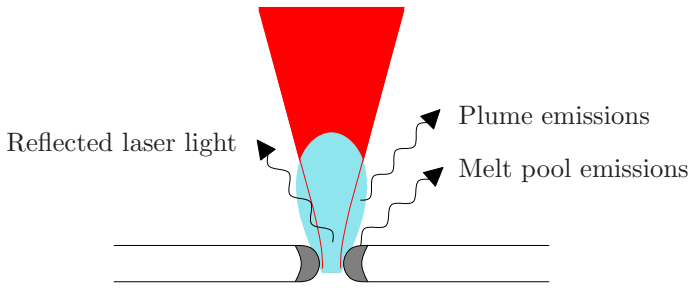

Figure 3.2: *Schematic overview of all optical emissions from the laser welding process.*

3.2). Firstly, Nd:YAG laser radiation is reflected from the workpiece. This light is monochromatic with a wavelength of 1064 nm. A second source is the plume in and above the keyhole. For Nd:YAG laser welding, this plume has a low ionisation degree and mainly emits thermal radiation [34, 35]. Finally, the melt pool has temperatures up to the boiling temperature of the metal and emits infrared thermal radiation.

3.1.1 Experimental Setup for Spectroscopic Measurements

The spectroscopic measurements are performed using the laser source, beam delivery system, manipulator and shielding gas configuration as used in the photodiode-based control system, which is described in Chapter 2 (Page 26). The laser light is projected onto the workpiece using a Trumpf BEO D70 welding head with a 200 mm collimator lens and a 150 mm focus lens, which results in a focal diameter of 0.45 mm (Figure 3.1). Figure 3.3 shows a photograph of the setup.

Wide-band spectral measurements are made using a calibrated HR4000 Ocean Optics spectrometer with a 0.2 mm diameter core optical fiber and a small quartz lens (Figure 3.4). This spectrometer is equipped with a 3648-element CCD array and a grating with 300 lines/mm, sensitive for a wavelength range of 200 to 1050 nm with an optical resolution of 1 nm. During both the coaxial and the off-axis measurements, a wide band-pass

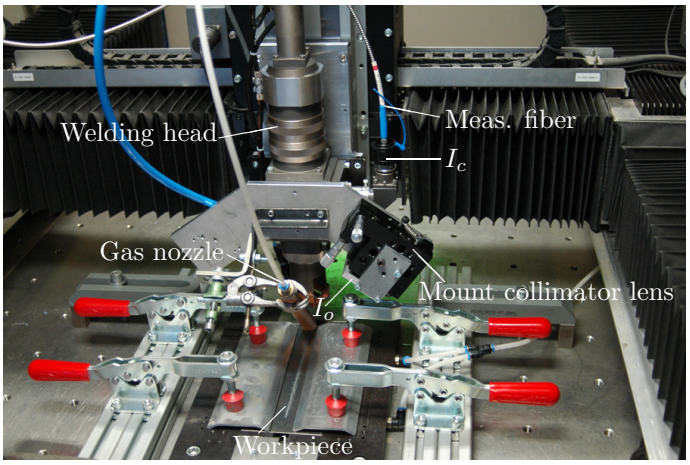

Figure 3.3: *Photo of the BEO D70 Trumpf laser welding head with the coaxially mounted spectroscope measurement fiber, on the gantry manipulator.*

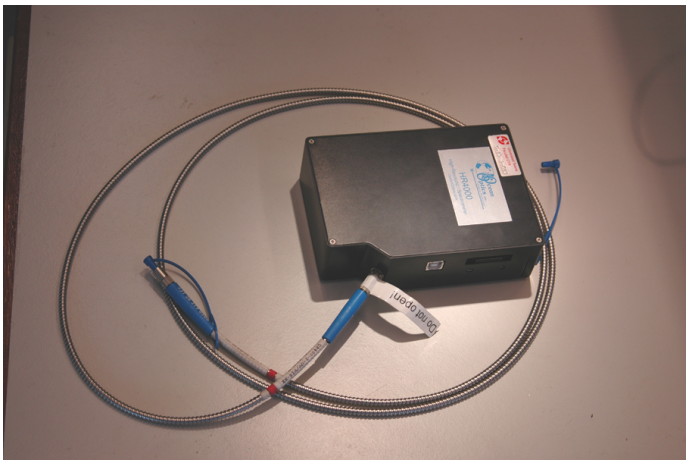

Figure 3.4: *Photo of the Ocean Optics HR4000 spectroscope with measurement fiber.*

AA5182		FeP04/DX54D-Z[1]	
		517.0	Weak
517.5 ± 0.5	Weak		
		526.0	Weak
		527.0	Weak
		533.0	Weak
589.0	Strong	589.0	Fairly strong
640.5	Weak		
670.5	Fairly strong		
766.5	Strong	766.5	Fairly strong
770.0	Strong	770.0	Fairly strong

Table 3.1: *Overview of the peaks detected in the different measurement spectra.*

[1]The spectra of FeP04 and DX54D-Z are similar.

filter with a transmission range of 450 to 950 nm is placed in front of the collimator lens of the spectrometer, to protect the CCD from back-reflected Nd:YAG radiation. Since most potential illumination sources for the monitoring system emit visible and near-IR light (approximately 600 to 1100 nm), the spectral range of 200 to 450 nm is of less interest and can be filtered out without problems. This will be discussed in more detail in Section 3.2.

3.1.2 Spectroscopic Measurement Results

Since the transmittance of the optical wide band-pass filter is known (see Appendix B), the off-axis irradiance I_o and the coaxial irradiance I_c are corrected for this filter. Figure 3.5 shows the corrected I_o and I_c for the laser welding process of 1.1 mm AA5182-O/H111, 1.0 mm FeP04 and 1.5 mm DX54D-Z GI sheets respectively. All experiments were conducted using a welding speed of 100 mm/s and a laser power of 4.0 kW.

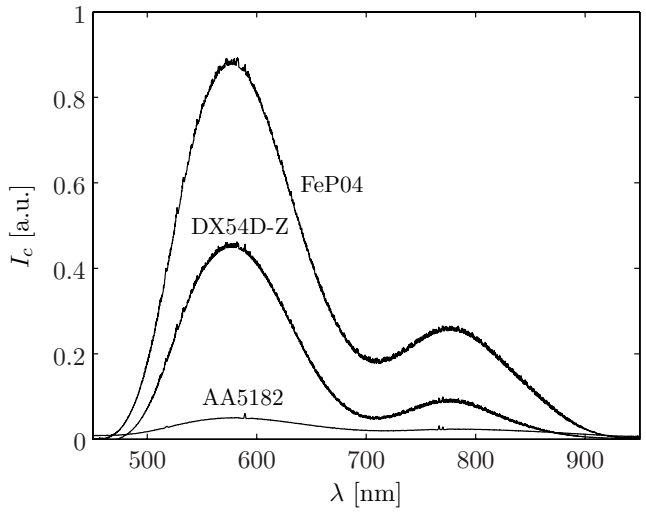

(a) Off-axis measured spectra.

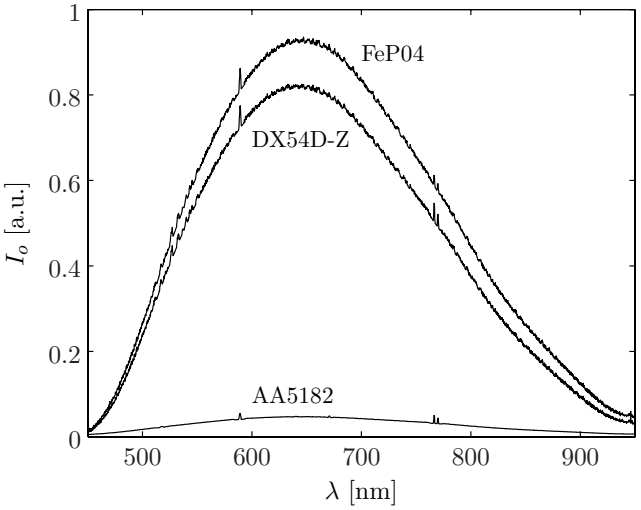

(b) Coaxially measured spectra.

Figure 3.5: *Measurements of the emission spectra, corrected for the wide band-pass filter.*

3.1 Optical Process Emissions

The off-axis spectra show for all materials, that the emitted light has a broadband character, which indicates that the weld plume and keyhole gasses mainly emit thermal radiation. If the emission coefficient of the material is assumed to be constant for the entire spectrum, the maximum temperature of the welding process can be estimated from I_o using Wien's Displacement Law

$$T = \frac{k_W}{\lambda_{max}}, \tag{3.1}$$

where λ_{max} is the wavelength for which the thermal radiation curve reaches it's maximum value and k_W is Wien's displacement constant ($2.897{\cdot}10^{-3}$ m K) [36]. For all three materials, this results in a temperature of about 4500 K. This value is of the same order as found by other researchers [34, 35].

For a more accurate prediction of the plume temperature, the following aspect needs to be taken into account. The spectral content of the thermal radiation is highly dependent on the temperature of the plume. Since the weld plume has a temperature distribution, rather than one homogeneous temperature, the measured curve will have contributions of thermal radiation from the entire temperature range. The parts of the plume with the highest temperatures will be dominant in this spectrum.

Since the estimated temperature is considerably higher than the melt pool temperatures, most of the thermal radiation is emitted by the gasses in the keyhole and/or in the weld plume (for a more detailed discussion of the keyhole wall temperature, see Section 5.2). The level of ionisation for these temperatures can be estimated using the Saha equation [37]. For a gas temperature of 4500 K, the ionisation degree of Al and Fe plasmas is about 0.04 % and 0.1 %, respectively [1]. Despite this low ionisation degree, some peaks have been observed in the the spectra (Table 3.1). The presence of these peaks needs to be taken into account in the design of the camera-based monitoring system.

The coating of the dichroic mirror has a low reflectance in the wavelength ranges of 650 to 780 nm and of 820 to 1100 nm. This causes the low signal value for the coaxially measured spectra shown in Figure 3.5(b). Since a low signal value will increase the required exposure time and de-

crease the signal-to-noise ratio of the camera, these two wavelength ranges are less suited for a coaxial monitoring system.

3.2 Camera-Based Systems

In this section, a newly developed camera-based monitoring system will be discussed. In the following section, the problems with traditional camera systems are described, followed by a treatment of the physical principles of the new monitoring system in Section 3.2.2. Section 3.2.3 describes the developed prototype. Finally, the results obtained using the prototype during the welding of various materials is discussed in Section 3.2.4.

3.2.1 Visualisation of Aluminium Laser Welding

In-situ visual inspection during welding by means of a camera-based monitoring system is required for the understanding of the welding process. The obtained images can also be used to monitor or control the weld quality online. However visualising the laser welding process of aluminium is difficult due to the large temperature range of the melt pool and the accompanying large differences in intensity of the thermal radiation, which are difficult to visualise simultaneously. Also the fact that aluminium is very reflective for the Nd:YAG radiation has a negative influence on the image quality of traditional vision-based monitoring systems.

Though many researchers have addressed this visualisation problem (see for example [38, 39]), an industrial in-situ monitoring system for laser welding of aluminium is still unavailable. In Figure 3.6(a), a typical camera image is shown. This image shows that only a bright white spot is visible where the Nd:YAG laser irradiates the sample. The melt pool and keyhole are not visible in this image. The light reaching the camera chip, is a combination of thermal radiation and reflected Nd:YAG laser radiation. Experimental studies show, that the information that can be extracted from these images (with or without optical filtering) is limited [1].

In this work, a different approach is chosen. By using a monochromatic external illumination source in combination with a narrow band-pass filter

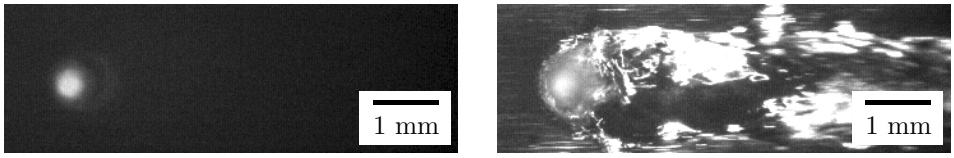

(a) Without illumination. (b) With illumination.

Figure 3.6: *In-situ CMOS camera image of the laser welding process of AA5182, with a narrow band-pass filter placed in the beam path.*

placed in front of the camera, a geometrical image of the welding process can be generated (Figure 3.6(b)). In the following section a more detailed description of this imaging method is given.

3.2.2 Physical Principles Monitoring System

Without external illumination (Figure 3.6(a)), there is hardly any geometrical information obtained of the weld zone around the keyhole. This is due to (i) the large contrast between the keyhole area and it's surroundings and (ii) the blurring of the image by light emitted and scatted in the weld plume. To obtain a good geometrical image of the welding process, external illumination is applied (Figure 3.6(b)). The occurrence of welding defects can be observed directly from these images, which is not possible from images without external illumination.

The irradiance of the external illumination light has to be sufficiently high compared to the irradiance of the light emitted by the welding process itself. By using a narrow band-pass filter with a Central Wavelength (CW) of 806 nm and a Full Width Half Maximum (FWHM) of 4 nm in combination with a matching monochromatic illumination source (λ is 805 nm), like a diode laser, only process light in a very small wavelength range can reach the camera chip. To obtain a clear image, it is important that the CW of the narrow band-pass filter matches with the diode laser light wavelength. This is illustrated in Figure 3.7. The spectra show that the use of a narrow band-pass filter suppresses the light emitted by the process significantly

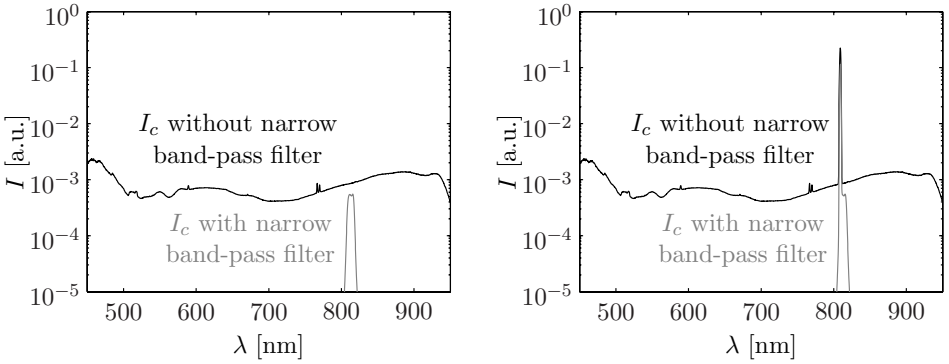

(a) Without illumination. (b) With illumination.

Figure 3.7: *The coaxial spectra of the light reaching the camera, both with and without the narrow band-pass filter in the beam path, for the welding of AA5182 sheets.*

(Figure 3.7(a)), whereas the diode laser light passes the narrow band-pass filter without significant attenuation (Figure 3.7(b)). In this figure, the diode laser light is visible as a sharp peak around 805 nm. In all cases, a broad band-pass filter (Melles Griot 03SWP624) was also used to protect the detector from the high intensity Nd:YAG radiation. For details of the laser and filters see Section 3.2.3 and Appendix B.

3.2.3 Prototype Monitoring System

Based on experimental results, a prototype of a laser weld monitoring system has been developed. In this section, the different elements of this prototype are discussed.

Figure 3.8 gives a schematic overview of the monitoring system. In this prototype a standard Trumpf BEO D70 welding head is used (Figure 3.9). The collimator lens had a focal distance of 200 mm and the system has been tested using focussing lenses of 150 and 200 mm, resulting in focal diameters of 0.45 and 0.60 mm, respectively.

3.2 Camera-Based Systems

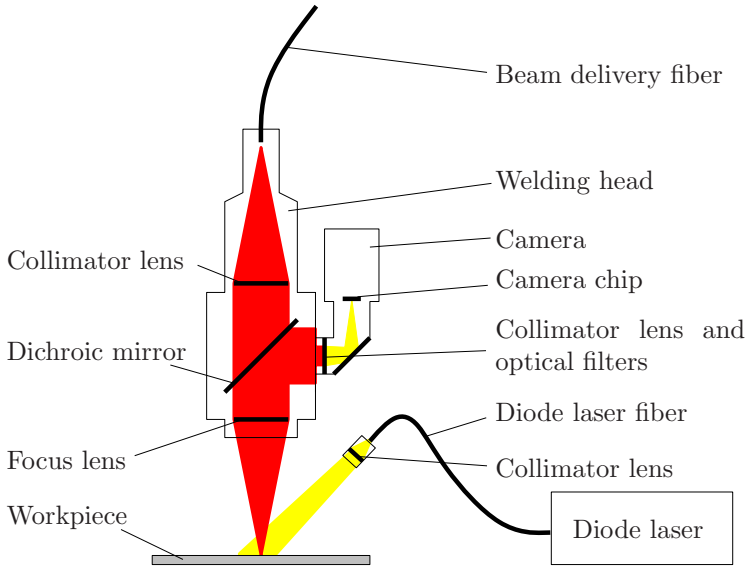

Figure 3.8: *Schematic overview of monitoring system.*

For a good signal-to-noise ratio, it is important that the illumination source is monochromatic, is sufficiently strong and has a wavelength which lies preferably not in the windows of 650 to 780 nm and 820 to 1100 nm. Furthermore, the illumination system connected to the welding head should be compact. Based on these specifications, a fiber coupled 10 W diode laser source (Laserwave LW-3010-HB [40]) with a wavelength of 805 nm is chosen. The laser light is transported to the welding head using a 0.60 mm core optical fiber. A small adjustable collimator lens, which typically has a diameter of 12 mm, is used to collimate the diode laser beam and to adjust the illumination spot size (Figure 3.10). The emission spectrum of this diode laser is shown in Figure 3.11.

A custom made Thorlabs CDI1553 805-4 filter with a CW of 806 nm and a FWHM of 4 nm was used, which is within the given specifications (Figure 3.11). In addition, to suppress the reflected Nd:YAG radiation, a

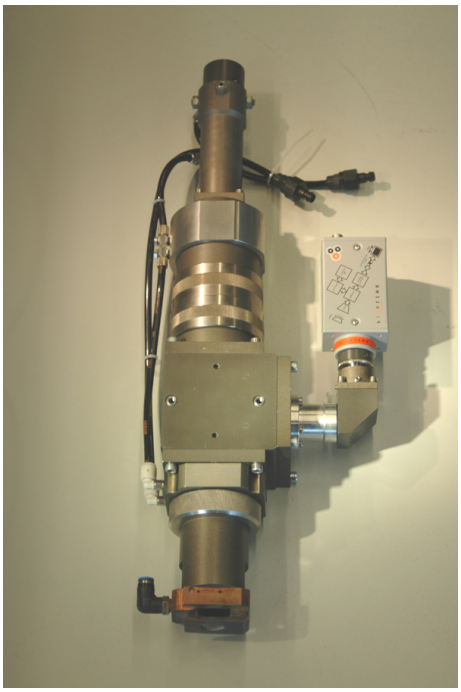

Figure 3.9: *Photo of the BEO D70 Trumpf laser welding head, together with the PixeLINK PL-A741 CMOS camera.*

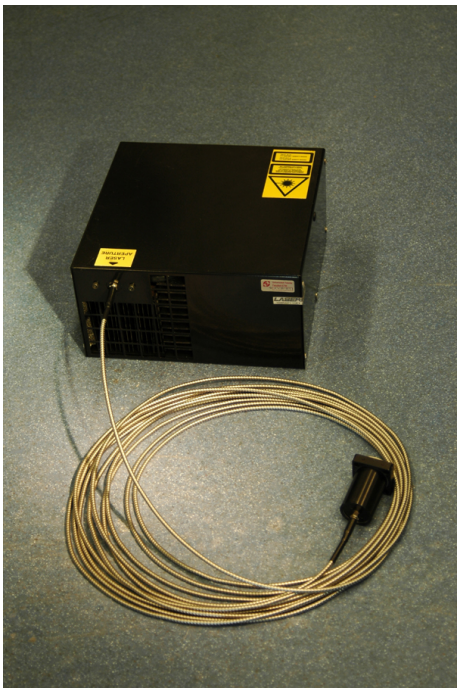

Figure 3.10: *Photo of the Laserwave LW-3010-HB fiber coupled diode laser, together with the optical fiber and the collimator lens.*

wide band-pass filter is placed in front of the camera chip. The Thorlabs FES0950 6704 or the Melles Griot 03SWP624 filter are suitable for this purpose. The transmittance data of these filters can be found in Appendix B.

It is important that the spatial and temporal resolution of the camera are adjustable and that the chip is insensitive for blooming. Therefore, a CMOS camera is preferred over a CCD camera. For this prototype, a PixeLINK PL-A741 monochrome CMOS camera was used, which has

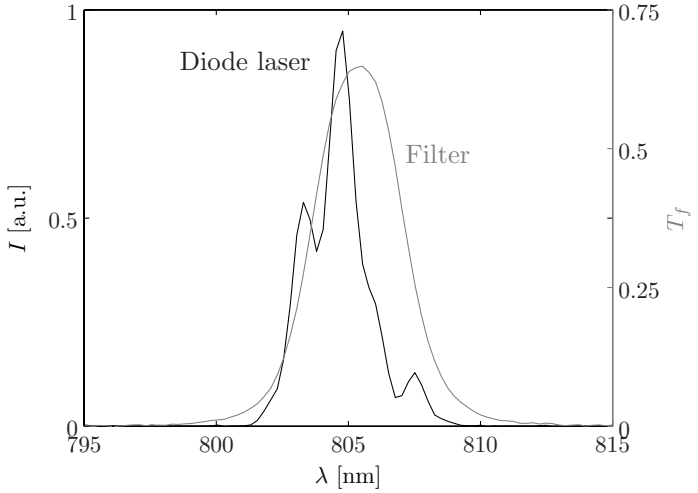

Figure 3.11: *Emission spectrum of the Laserwave LW-3010-HB diode laser, together with the transmittance of the Thorlabs CDI1553 805-4 optical interference filter.*

IBIS5-A-1300 CMOS chip with 1024x1024 pixels (Figure 3.9, 3.12 and 3.13) [41]. For investigation of process dynamics during welding, a high-speed CMOS camera is very suited. In this case, experiments were carried out using a Visible Solutions Phantom V4.2 and V5.0 high-speed camera [42].

3.2.4 Monitoring System Performance

The monitoring system is suited for the laser welding of any material, as long as the illumination irradiance is higher than the irradiance of the process emissions at the camera chip. Spectral measurements showed that the use of filler wire, a twin spot configuration and/or a different shielding gasses, have no significant influence on the emission spectra and therefore will not influence the monitoring system performance. The addition of an arc welding source, in the case of hybrid laser/arc welding adds several strong peaks to the spectrum. In Chapter 6 it will be shown that also in

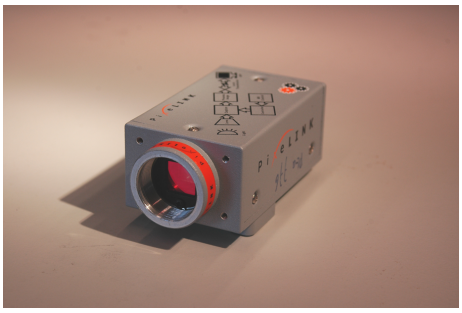

Figure 3.12: *Photo of the PixeLINK PL-A741 CMOS camera.*

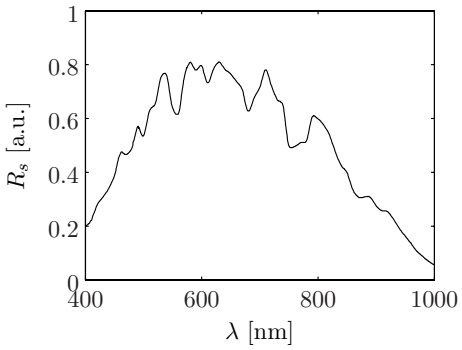

Figure 3.13: *Spectral response of the PixeLINK PL-A741 CMOS camera (Courtesy of PixeLINK).*

this situation, the monitoring system can be used.

For a good image quality, it is important that the image is sharp. There are two factors that influence the image sharpness. Obviously, the camera must be in focus, which can be accomplished easily. Secondly, images of moving objects suffer from motion blur. This effect is caused by the fact that during the exposure time, the object is not stationary. Melt pool fluctuations can be up to several hundred Hz. It was experimentally found that exposure times below 0.3 ms result in sharp images of the melt pool.

Keyhole fluctuations have frequencies up to several kHz. To capture these fluctuations, the exposure time must be lower than approximately 50 μs. The lower limit of the exposure time is determined by the shutter speed, the camera chip sensitivity, the sensor noise level and the illumination irradiance.

The diode laser power and the size of the illumination spot determine the illumination irradiance. The irradiance is inversely proportional to the squared spot diameter. The minimum required spot diameter will depend on the area of interest. In general, an illumination spot diameter of about 12 mm is sufficient to cover the entire welding area for most laser welding

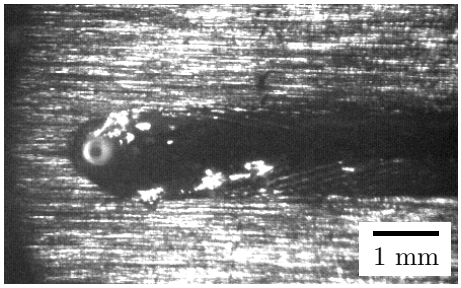

(a) AA1050-H14/H24

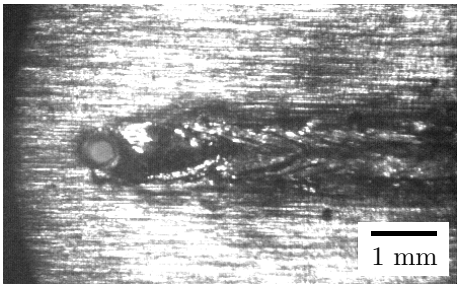

(b) AA5182-O/H111.

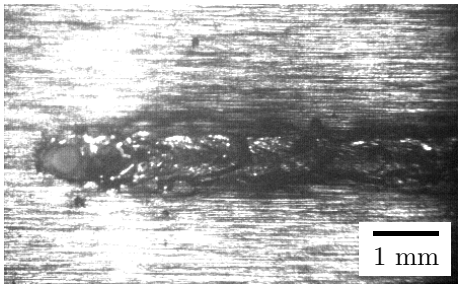

(c) AA7075-T651

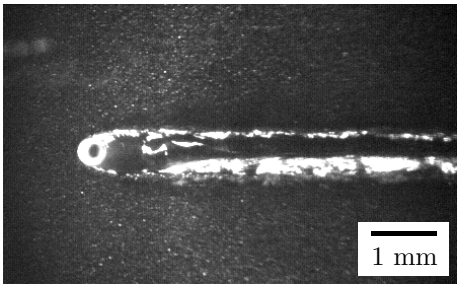

(d) FeP04

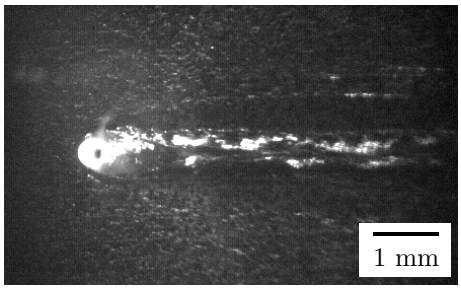

(e) DX54D-Z GI

Figure 3.14: *In-situ camera images of the laser welding process for different materials, using the new monitoring system (bead-on-plate experiments).*

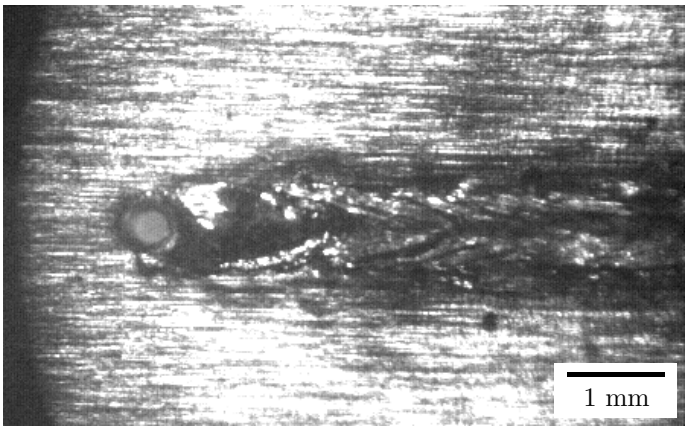

(a) Camera image.

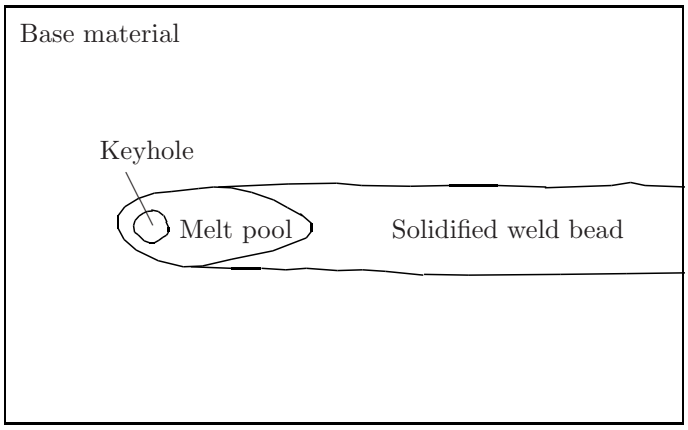

(b) Schematic overview.

Figure 3.15: *Schematic overview of the camera image for the laser welding process of a 1.1 mm AA5182 sheet (bead-on-plate), with a laser power of 4.0 kW and a welding speed of 100 mm/s.*

processes. The maximum power of the diode laser was in this case about 10 W. This results in an illumination irradiance of about 10^5 W/m^2. Using the PixeLINK camera in combination with these illumination settings, the exposure time can be reduced to about 0.1 ms. This camera is therefore suitable for capturing the melt pool contour (Chapter 4). The Phantom high-speed camera has a higher camera chip sensitivity, a lower sensor noise and a faster shutter. Therefore, the exposure time can be reduced to about 30 μs when using this camera, which is sufficient to sharply image the keyhole wall (Chapter 5).

Figure 3.14 shows typical in-situ camera images of the welding process for five different materials. Experiments were performed in a bead-on-plate configuration, using 4.0 kW laser power, a welding speed of 100 mm/s, 0.45 mm diameter spot and Ar shielding gas. In these experiments, the PixeLINK camera was used.

The images show that the monitoring system generates clear images of the weld zone and it's surroundings. For all materials, the base material, the melt pool, the solidified weld bead and the keyhole can be clearly distinguished. In Figure 3.15 the camera image of the AA5182 welding process is enlarged, together with a schematic representation of the weld zone. The white and black areas visible in the melt pool and on the weld bead are caused by the surface texture in combination with the inclined illumination (shadow effect). The streaks on the base material in the welding direction are due to surface roughness caused by the rolling process during sheet production.

3.3 Conclusions

- Spectral measurements of the Nd:YAG laser welding process of aluminium and mild steel show that the light emitted is mainly due to thermal radiation. A few additional small peaks can be observed which most probably are due to emission lines of elements in the plume.

- Based on the thermal radiation of the process, an estimation of the

plume temperature can be made using Wien's law. This gives an estimated plume temperature of about 4500 K.

- Monochromatic illumination, in combination with narrow band-pass filtering results in clear camera images of the welding process and its surroundings. Good results were obtained by using an illumination wavelength of 805 nm.

- A prototype of a camera-based welding process monitoring system has been constructed, using a standard laser welding head, a coaxially mounted standard or high-speed industrial CMOS camera and a 10 W fiber coupled diode laser.

- Tests show that this monitoring system records clear images for the Nd:YAG laser welding process of different aluminium alloys and (zinc coated) steel sheets. This system is also suitable for observing the laser welding of other materials. The tests show the applicability of this system for single and twin spot laser welding, with and without cold wire feeding. This system can also be used to monitor hybrid laser/GMA welding, but the selection of an appropriate illumination wavelength is more critical here (see also Chapter 6).

Chapter 4

Melt Pool Shape

To better understand the different aspects of the laser welding process, experimentally validated simulation models can be of aid. There exist many different modelling methods, all with their specific advantages and limitations. In this chapter, a 2D Finite Element Method (FEM) model, based on work by de Lange [43], is used to model the temperature distribution and the melt flow within the melt pool. FEM calculations and welding experiments have been performed for mild steel FeP04 and for aluminium alloy AA5182. Parts of this work have been published earlier [44].

Section 4.1 provides the motivation why the FEM model of de Lange is used in this work. In Sections 4.2 to 4.4, the FEM model is described. The model calculates the temperature distribution and the fluid flow in and around the weld zone. Sections 4.6 and 4.7 discuss the melt pool shapes calculated using this FEM model for the laser welding process of thin AA5182 and FeP04 sheets, respectively. These shapes are compared to real-time images of the melt pool, which have been recorded using the developed monitoring system discussed in Chapter 3. In Section 4.8, the main conclusions of this chapter are summarised.

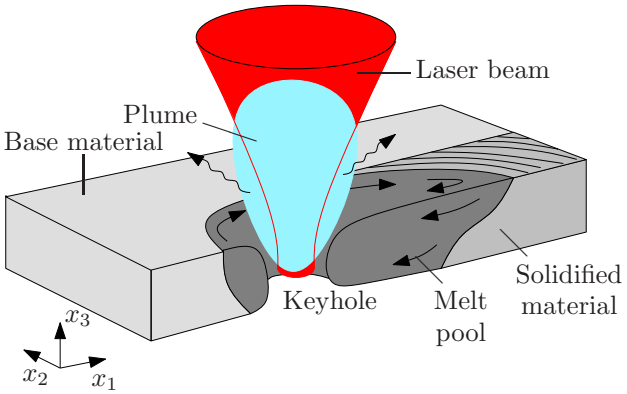

Figure 4.1: *Schematic cross section of the full penetration keyhole laser welding process of a thin sheet.*

4.1 Melt Pool Modelling

In literature, many models have been proposed for the keyhole laser welding process (e.g. [43, 45, 46, 47, 48]). For an accurate description of the keyhole laser welding process, it is important that a model is used which couples the physical phenomena in the different weld domains.

The time-invariant FEM laser welding model developed by de Lange [43] provides a good basis for the modelling of the keyhole welding process of thin sheets, since the different physical phenomena are coupled in a realistic way. Also non-linear effects, like latent heat and temperature dependent material parameters, which can have a large influence on the results of the model, can be incorporated.

Furthermore, by defining different domains the model only calculates the flow field of the melt in the region where molten material can occur. Outside this domain, only the temperature is calculated. This allows the incorporation of many small elements in the keyhole region, which is favourable for the accuracy of the results of the method.

Figure 4.1 gives a schematic overview of the laser welding process of thin metal sheets. In this figure, the spatial directions that will be used

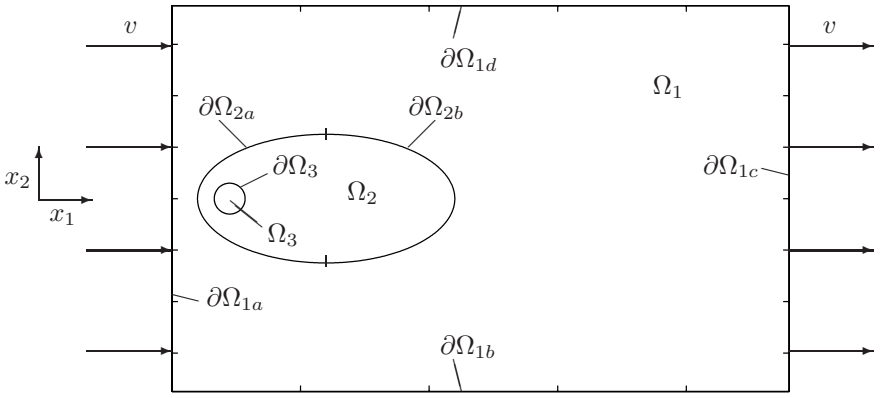

Figure 4.2: *The computational domain of the FEM model. The different domains are indicated with Ω_i and the domain boundaries with $\partial\Omega_i$. The material flows from left to right through the domains.*

in the model are indicated. In the model, variations of the temperature distribution and the melt flow field in the x_3-direction are neglected.

4.2 Computational Domain

The computational domain of the 2D model is given in Figure 4.2. In this model, the material flows from left to right through the computational domain, with a constant speed equal to the welding speed v. The laser spot is at a fixed position in the domain. Note that x_1 and x_2 are two elements of the spatial vector $\boldsymbol{x}$. The domain has been divided into three sub-domains. In domain Ω_1 only solid material is present. Domain Ω_2 represents an area containing both solidified and molten material. This means that the melt pool lies within Ω_2 and possibly for a very small part within Ω_3. Domain Ω_3 represents the laser spot. This is the area where the laser energy enters the computational domain.

The edge of the computational domain is given by boundary $\partial\Omega_1$. The boundary $\partial\Omega_2$ has an elliptical shape and lies entirely within the solid material. Boundary $\partial\Omega_3$ is circular and has the same dimensions as the average keyhole diameter. The boundary of the solid-liquid interface within Ω_2 follows from the calculated temperature distribution, and is indicated by the melt isotherm T_m (not shown in Figure 4.2). This melt isotherm lies within domain Ω_2 and is treated in more detail in Section 4.5.

4.3 Thermal Model

During welding, the temperature has a strong influence on the resulting weld quality. In the model, the energy input due to the laser radiation, the heat diffusion and the convection are taken into account. The viscous dissipation of energy is neglected, the melt is assumed to be incompressible and it is assumed that the pressure inside the melt pool is constant. Therefore, the energy balance equation can be written as

$$\rho c_p^* \frac{\partial T}{\partial t} = q(\boldsymbol{x}, t) z_1(T) + \nabla \cdot k \nabla T - \rho c_p^* \boldsymbol{u} \cdot \nabla T \tag{4.1}$$

where ρ is the density, c_p^* is the specific heat (including the latent heat, see Equation 4.4) and k is the thermal conductivity. The local fluid velocity vector is indicated with $\boldsymbol{u}$. In general, all material parameters are functions of temperature T. The temperature dependency of c_p^* and k is taken into account in the model. A change in density due to a temperature variation is compensated for by an accompanying change in volume due to thermal expansion, thus guaranteeing conservation of mass. Therefore the density is kept constant in this model.

Furthermore, $q(\boldsymbol{x}, t)$ is a heat source as a function of space $\boldsymbol{x}$ and time t. The heat source is multiplied by a dimensionless saturation function $z_1(T)$, which cuts off the energy flux above a certain temperature level, reflecting the loss of energy through the bottom keyhole opening. The temperature dependent function $z_1(T)$ has the value 1 when $T \leq T_k$ and 0 for $T > T_k$, where T_k is the keyhole wall temperature.

Temperature	T_m	$\tilde{T} = \frac{1}{T_m}T$
Velocity	v	$\tilde{\boldsymbol{u}} = \frac{1}{v}\boldsymbol{u}$
Space	$2r_s$	$\tilde{\boldsymbol{x}} = \frac{1}{2r_s}\boldsymbol{x}$ $\tilde{\nabla} = 2r_s\nabla$
Time	$\frac{2r_s}{v}$	$\tilde{t} = \frac{v}{2r_s}t$
Heat source strength	$\frac{P_a}{\pi r_s^2 b}$	$\tilde{q} = \frac{\pi r_s^2}{P_a}q$
Pressure	ρv^2	$\tilde{p} = \frac{1}{\rho v^2}p$
Volumetric force	$\frac{\rho v^2}{2r_s}$	$\tilde{\boldsymbol{F}} = \frac{2r_s}{\rho v^2}\boldsymbol{F}$

Table 4.1: *The characteristic parameters used for normalisation of the FEM model parameters.*

It is computationally favourable to rewrite Equation 4.1 in dimensionless parameters using characteristic values (Table 4.1) for the temperature, the fluid velocity, the spatial coordinates, the density, the heat capacity and the heat source strength. The dimensionless temperature is defined as $\tilde{T} = T_m^{-1}T$, the dimensionless velocity is defined as $\tilde{\boldsymbol{u}} = v^{-1}\boldsymbol{u}$, etc. The dimensionless heat balance equation can be written as

$$c_p^*(T)\frac{\partial \tilde{T}}{\partial \tilde{t}} = \frac{2P_a}{\pi\rho v r_s b T_m}\tilde{q}(\tilde{\boldsymbol{x}},\tilde{t})\tilde{z}_1(\tilde{T}) + \tilde{\nabla}\cdot \mathrm{Pe}(T)^{-1}\tilde{\nabla}\tilde{T} - c_p^*(T)\tilde{\boldsymbol{u}}\cdot\tilde{\nabla}\tilde{T}, \tag{4.2}$$

where the temperature dependent Peclet number $\mathrm{Pe}(T)$ is defined as

$$\mathrm{Pe}(T) = 2\rho v r_s \frac{c_p^*(T)}{k(T)}. \tag{4.3}$$

The Peclet number gives the ratio between the heat transfer due to convection and that due to conduction.

In the present study, a steady-state solution is calculated, which means that the left-hand side of Equation 4.2 is zero.

The effect of latent heat due to the solid-liquid phase transformation is incorporated by increasing the specific heat between the solidus and liquidus temperatures [43] (Figure 4.3, see also Appendix C)

$$\begin{aligned} c_p^*(T) &= c_p(T) + L(T) \\ L_m &= \int_{T_s}^{T_l} L(T) dT, \end{aligned} \tag{4.4}$$

where $L(T)$ is the latent heat as a function of temperature, L_m is the total amount of latent heat of the solid-liquid phase transition and $c_p(T)$ is the specific heat as a function of temperature without the latent heat. Figure 4.3 shows that $c_p(T)$ and $L(T)$ are modelled as smooth continuous functions, which is necessary for stability of the numerical implementation of the model.

To solve the energy balance equation, boundary conditions need to be defined. Since the welding speed is high compared to the speed of heat transport due to conductivity, the material that enters the computational domain is assumed to be unaffected by the heat input through the keyhole. Therefore, boundary $\partial\Omega_{1a}$ is set to room temperature T_r (Dirichlet boundary condition). Since the boundaries $\partial\Omega_{1b..d}$ are assumed to be chosen far away from the the keyhole, the flux due to conduction is expected to be negligible (Neumann boundary conditions). Therefore, the boundary conditions are written as

$$\begin{aligned} T &= T_r && \text{at} \quad \partial\Omega_{1a} \\ \boldsymbol{e_n} \cdot \nabla T &= 0 && \text{at} \quad \partial\Omega_{1b..d} \end{aligned} \tag{4.5}$$

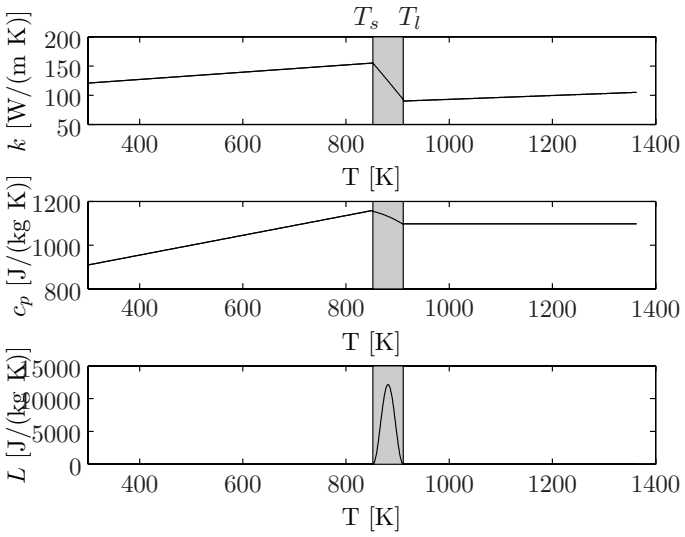

Figure 4.3: *The thermal conductivity k [49, 50], the specific heat c_p [50] and the latent heat L for AA5182 [43, 51], as a function of the temperature. The gray area indicates the melt trajectory [8, 51].*

where $\boldsymbol{e_n}$ is the unit normal vector of the specific boundary, pointing out of the domain.

4.4 Hydrodynamical Model

To incorporate the effects of the melt flow in the model, the velocity field in the melt pool is calculated using the incompressible Navier-Stokes equations for flow of a Newtonian fluid, which is subjected to an external force field $\boldsymbol{F}$

$$\begin{aligned} \rho\frac{\partial \boldsymbol{u}}{\partial t} &= -\rho\boldsymbol{u}\cdot\nabla\boldsymbol{u} - \nabla p + \nabla\cdot\mu\left(\nabla\boldsymbol{u} + (\nabla\boldsymbol{u})^T\right) + \boldsymbol{F} \\ \nabla\cdot\boldsymbol{u} &= 0, \end{aligned} \tag{4.6}$$

where p is the pressure, μ is the dynamic viscosity and $\boldsymbol{F}$ is a vector with the external volume forces. Since a steady-state solution is calculated, the left-hand side of Equation 4.6 is zero. The dimensionless form of Equations 4.6 can be derived by defining additional characteristic quantities for viscosity, pressure and force, yielding

$$\begin{aligned} \frac{\partial \tilde{\boldsymbol{u}}}{\partial \tilde{t}} &= -\tilde{\boldsymbol{u}}\cdot\tilde{\nabla}\tilde{\boldsymbol{u}} - \tilde{\nabla}\tilde{p} + \tilde{\nabla}\cdot\mathrm{Re}^{-1}\left(\tilde{\nabla}\tilde{\boldsymbol{u}} + (\tilde{\nabla}\tilde{\boldsymbol{u}})^T\right) + \tilde{\boldsymbol{F}} \\ \tilde{\nabla}\cdot\tilde{\boldsymbol{u}} &= 0, \end{aligned} \tag{4.7}$$

where the Reynolds number Re is defined as

$$\mathrm{Re} = \frac{2\rho r_s v}{\mu}. \tag{4.8}$$

In Table 4.1 the characteristic values are listed, which are used for normalisation of the parameters in the hydrodynamical equation. In Appendix D, the melt flow around the keyhole during full penetration keyhole welding is shown to be laminar, based on an estimate of the Reynolds number.

To describe the presence of the keyhole, good results were obtained with a rather simple, straightforward model. This keyhole model uses an external force $\boldsymbol{F}$ to describe both the solidification of the melt and the presence of the keyhole. This force $\boldsymbol{F}$ is defined as

$$\boldsymbol{F} = \boldsymbol{K_s}(v\boldsymbol{e}_{x1} - \boldsymbol{u})z_2(T) - \boldsymbol{K_k}\boldsymbol{u}z_3(T), \tag{4.9}$$

where, the temperature dependent functions $z_2(T)$ and $z_3(T)$ are switching functions which activate or deactivate the respective terms. Function $z_2(T)$ switches the first term in Equation 4.9 on when the temperature is below the solidus temperature T_s and off when T is above the liquidus temperature

T_l, showing a smooth behaviour in the region of $T_s < T < T_l$. This smooth transition is implemented for numerical stability of the FEM computations.

When this force is switched on and $\boldsymbol{K_s}$ is relatively, the material is forced to move with speed v in the welding direction through the computational domain, which is fixed to the laser spot. When the force is switched off, the fluid can flow freely. In this way the solid-liquid phase transition is simulated. Physically this transition region can be interpreted as the mushy zone.

The second term in Equation 4.9 introduces a force which pushes the velocity in the melt to zero, causing a zone of stagnant melt. This zone behaves as an object in the melt, representing the keyhole. The function $z_3(T)$ equals 1 for $T > T_b$ and 0 for $T < T_b$, with a smoothed transition around the boiling temperature T_b for numerical reasons. The square 2x2 diagonal matrices $\boldsymbol{K_s}$ and $\boldsymbol{K_k}$ contain tuning parameters, which are used to control the amplitude of the components of the force terms in the two spatial directions.

Since the entire melt pool is inside domain Ω_2 and Ω_3, the Navier-Stokes equations are solved only in these domains. The boundary conditions for the Navier-Stokes equations are thus formulated for the boundary $\partial\Omega_2$, which lies entirely inside solid material. Along the front part of the boundary $\partial\Omega_{2a}$, the material is initially solid, and the speed of the material flow into domain Ω_2 equals the welding speed vector v (Dirichlet boundary condition). Along the rear boundary $\partial\Omega_{2b}$, the material is fully solidified. This means that along this boundary, the pressure can be assumed to be zero. The boundary conditions for the Navier-Stokes equations are defined as

$$\begin{aligned} \boldsymbol{u} &= v\boldsymbol{e}_{x_1} \qquad \text{at} \quad \partial\Omega_{2a} \\ p &= 0 \qquad\quad\ \ \text{at} \quad \partial\Omega_{2b}. \end{aligned} \tag{4.10}$$

4.5 Solution Strategy

The model is implemented using the Comsol Multiphysics$^{\text{TM}}$package [52, 53]. Figure 4.4 shows the mesh used for the FEM calculations, which con-

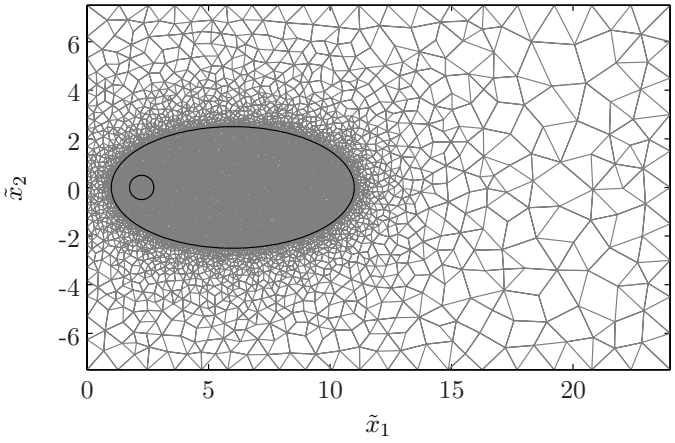

Figure 4.4: *The mesh used in the FEM model.*

tains over 20000 triangular and quadrilateral elements. In this case, the thermal and hydrodynamical models are coupled and temperature dependent material properties are used. The solver solves this steady non-linear problem using an affine invariant form of the damped Newton method [53].

The problem is solved in an iterative manner. First the energy equation is solved under the assumption that there is no fluid flow. The resulting temperature field is used as an initial condition for solving the hydrodynamical problem, under the assumption that the fluid flow has no influence on the temperature field. Finally, the temperature field and flow velocity calculated in these first runs are used as initial conditions for solving the combined thermal and hydrodynamical problem.

In the model the effect of the latent heat L_m is taken into account by increasing the specific heat c_p between T_s and T_l (Figure 4.3). As can be seen in this figure, this results in large values of $\frac{d}{dT}c_p^*$ in this temperature region. This in turn, introduces large non-linearities in the model. Therefore, for the solver to converge, the initial conditions need to be close to the solution. To overcome this, the solution is calculated in several consecutive runs. In the first run, L is added to c_p over a temperature interval much

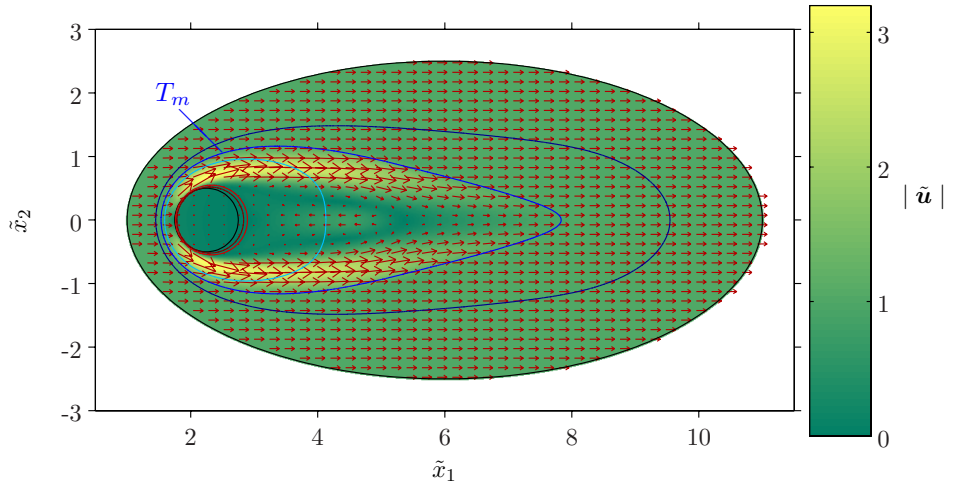

(a) FEM solution.

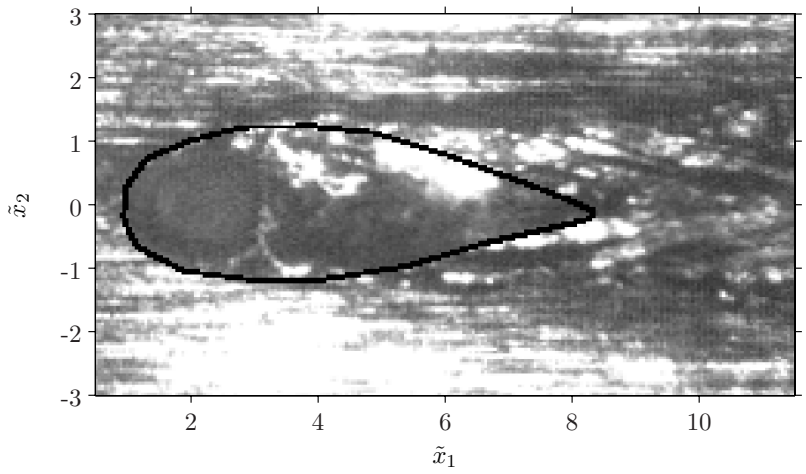

(b) Recorded camera image.

Figure 4.5: *A comparison between the melt contour calculated by the FEM model (upper figure) and observed in the camera images (lower figure) for the laser welding of AA5182, using $P = 4$ kW and $v = 100$ mm/s.*

larger than the actual melt trajectory. This decreases $\frac{d}{dT}c_p^*$ considerably and facilitates finding a converging solution. This solution is subsequently used as an initial condition for a second run, in which the temperature interval for the latent heat is chosen to be somewhat smaller. This is repeated until in the final run L is added to c_p only over the melt trajectory [43]. Figure 4.5(a) shows a typical result of the FEM calculations after the final run. The temperature distribution is indicated with isothermal lines. In Figure 4.5(a) isotherms for $T = 0.9\ T_m$, $T = T_m$, $T = 1.1\ T_m$, $T = 1.5\ T_m$ and $T = T_b$ are shown. The coloured background indicates the local amplitude of the fluid velocity. The arrows show the local direction and velocity of the fluid flow. It is important to note that all parameters are given in their dimensionless form.

4.6 Experimental Verification for Aluminium

The FEM model described above was used to calculate the shape of the melt pool during the laser welding process of aluminium alloy AA5182. This shape is compared to recorded images of this welding process, in which the contour of the melt pool is indicated (Figure 4.5(b)). The recordings of the welding experiments are carried out using the monitoring system described in Section 3.2. The relevant material properties are given in Appendix C.

In Figure 4.5(a) the isotherms and the flow field resulting from a FEM calculation for AA5182 are shown. In this case P is set to 4 kW and the welding speed v is 100 mm/s. The laser power that is absorbed by the workpiece is denoted as P_a and is smaller than the supplied laser power, due to reflections at the keyhole wall. In this model, it is assumed that at maximum 50% of the laser power is absorbed, although the exact amount of reflected laser power is unknown. In the FEM model, the spatial dimensions are scaled using the laser spot diameter $2r_s$.

The outer boundary of the melt pool is defined as the isotherm with the average value of the solidus and the liquidus temperature and is denoted with T_m. The chemical composition of the AA5182 alloy shows that magnesium is present in significant quantities (Table C.1). The boiling tem-

perature of Mg is the lowest of all elements present in the material (Table C.2). Therefore, the recoil pressure is mostly caused by the vaporisation of Mg atoms and the keyhole wall temperature is considered as approximately equal to the boiling temperature of Mg (Chapter 5). Therefore in the FEM model the keyhole wall temperature of AA5182 is set to the boiling temperature of Mg ($T_b = 1363$ K).

Figure 4.5(b) shows an in-situ camera image of the AA5182 welding process obtained using the same welding parameters as where used in the FEM computations shown in Figure 4.5(a) ($P = 4$ kW, $P_a = 2$ kW, $v = 100$ mm/s). Determination of the melt contour from such a single image is not straightforward. By considering a movie of a series of these images, the melt pool contour can be distinguished clearly and is outlined with a black line in Figure 4.5(b). By comparing the size and shape of the melt isotherm in the FEM computations (indicated with T_m) with the melt contour in the camera images, the accuracy of the calculated temperature field can be assessed. It is important to keep in mind that the melt contours calculated by the FEM models are 2D and should be interpreted as the melt contour averaged over the sheet thickness. The schematic cross section of the geometry of the melt pool in the FEM models is 2D and thus constant for the entire sheet thickness. The geometry in reality has a melt contour which varies in size over the sheet thickness. The melt contour observed in the camera images is the melt contour at the top surface. Therefore, the melt contour averaged over the sheet thickness (FEM model) will be different from the melt contour on the top surface (camera images).

The results of three model variations are compared with experimental data. In model I, the thermal and hydrodynamical equations are solved using constant values of the thermal conductivity ($k = 120$ W/(m K)) and the specific heat ($c_p = 1066$ J/(kg K)) over the entire temperature range. Also the effect of latent heat is not taken into account ($L_m = 0$). In model II, again the thermal conductivity is assumed to be constant ($k = 120$ W/(m K)). However, the latent heat is taken into account by adapting the specific heat between the solidus and the liquidus temperatures T_s and T_l, as shown in Figure 4.3 and Equation 4.4. Outside this temperature range, the specific heat is considered constant ($c_p = 1066$ J/(kg K)). Model

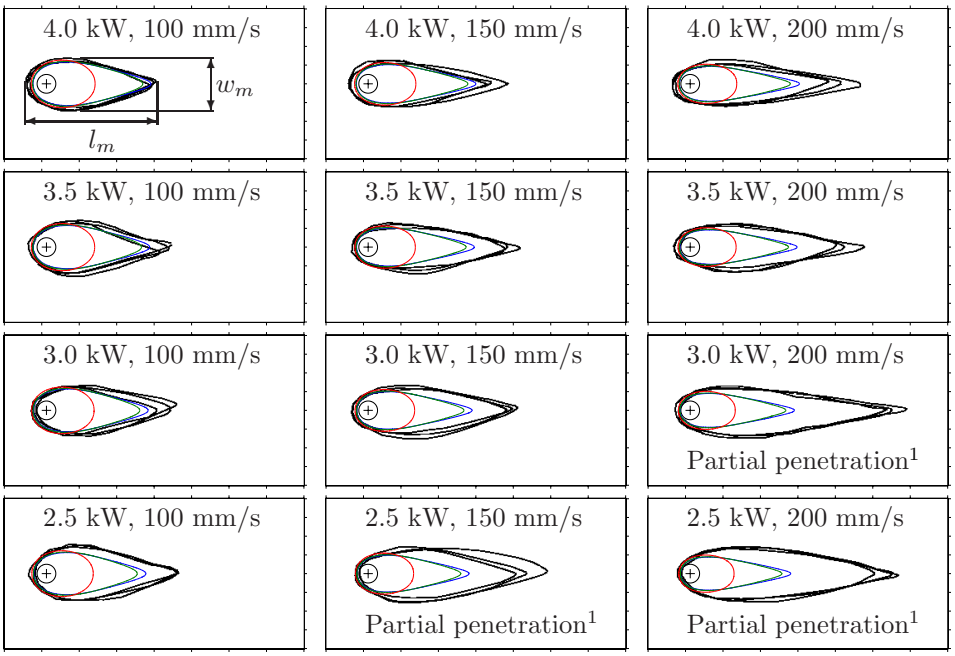

Figure 4.6: *The melt contours as predicted by* ***Model I*** *(constant c_p, constant k, $L_m = 0$),* ***Model II*** *(constant c_p, constant k, $L_m \neq 0$) and* ***Model III*** *($c_p(T)$, $k(T)$, $L_m \neq 0$), compared to the edges of the melt pool observed in three different* ***camera images*** *of the weld, for different values of laser power and welding speed, for 1.1 mm thick AA5182 sheets. The circle with the cross indicates the position and size of the laser spot.*

[1]Partial penetration of the keyhole and the melt.

III includes temperature dependent values of the thermal conductivity and the specific heat, as given in Appendix C, including the latent heat. Figure 4.6 shows the melt contours as predicted by the three 2D models, together with contours of the melt pool extracted from three different camera images for each weld.

Figure 4.6 shows that Model I does not produce an accurate prediction of the melt pool size and shape. The camera images show a typical V-shaped tail of the melt contour, while in the prediction a much shorter rounded shape appears. In the roughness pattern of the solidified weld bead, V-shaped striations are visible, which are consistent with the V-shaped tail of the melt contour. De Lange [43] has found that this V-shape is sharper when T_s and T_l are closer to each other. This observation can be explained as follows. A smaller melt trajectory results in higher values of c_p^* between T_s and T_l, which in turn will result in a large values of the Peclet number (Equation 4.3). This means that around the melt temperature, the convection term is dominant. Due to the welding speed, the convective term has a large component in the x_1 direction, which results in the elongated V-shape of the melt pool. The rounded shape of the other isotherms (Figure 4.5(a)) indicates that for temperatures outside the melt trajectory, the conduction term is more important, which is approximately equal in both the x_1 and the x_2 directions. Since Models II and III include the latent heat of the solid-liquid phase transition, they predict this V-shape more accurately. This demonstrates the importance of incorporating the latent heat in welding models.

Model III results in the most accurate predictions of the melt contour, although the predictions of Model II are nearly as good. Apparently, the temperature dependence of the material parameters has a small influence on the model results for AA5182.

The length and width of the melt pool are denoted with l_m and w_m and are defined in Figure 4.6 (top, left insert). The melt pool dimensions calculated by Models II and III for most values of P and v are smaller than the melt pool length observed in the camera images (Figure 4.7). The camera images also show that l_m increases with the welding speed v, while in the models l_m is almost constant for varying values of v. Figure 4.8

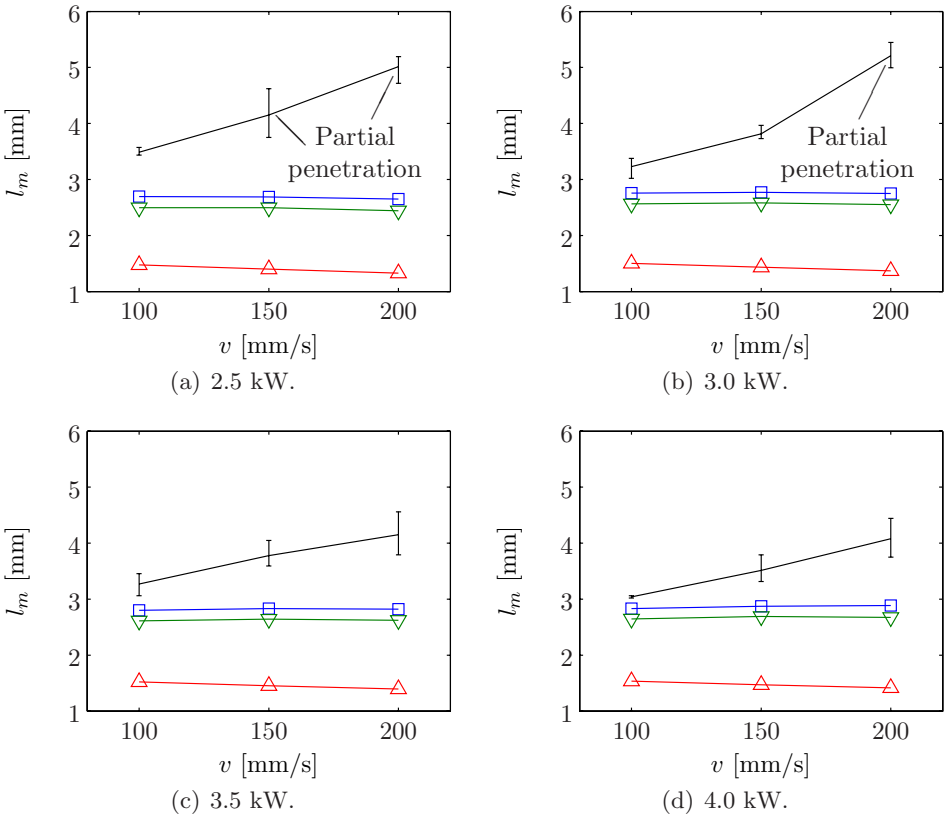

(a) 2.5 kW. (b) 3.0 kW.

(c) 3.5 kW. (d) 4.0 kW.

Figure 4.7: *The melt pool length l_m as predicted by Model I (△), Model II (▽) and Model III (□), compared to the length observed in the camera images (–) for 1.1 mm AA5182 sheets. The variation in the melt pool length calculated from the three different camera images is indicated with an error bar.*

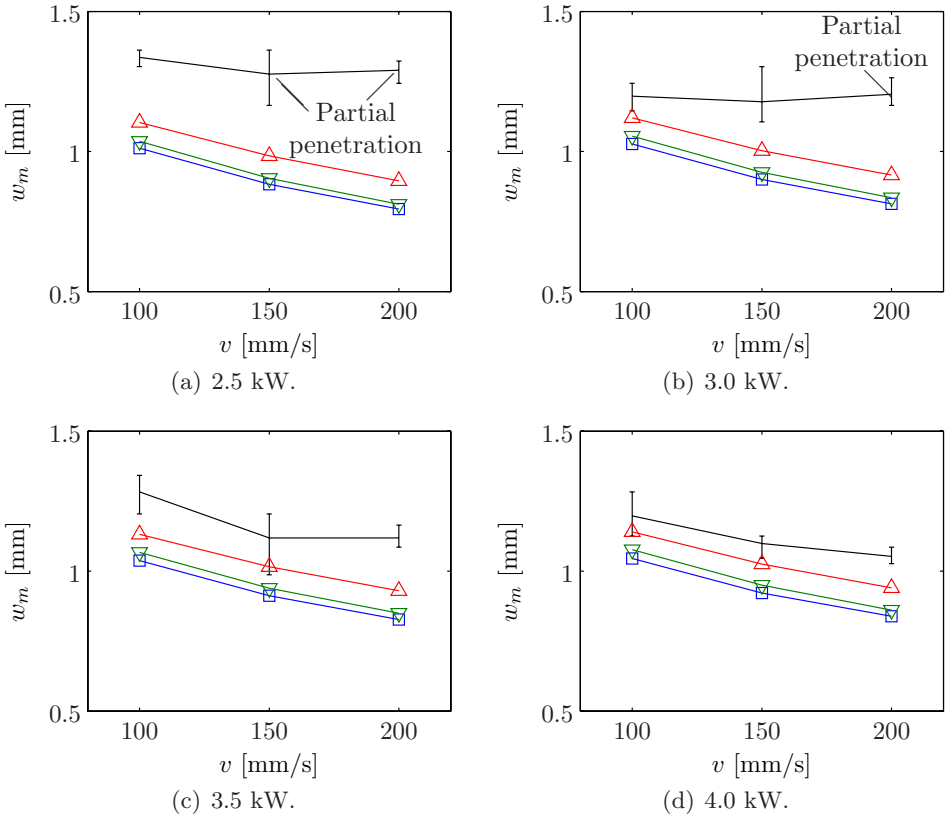

(a) 2.5 kW. (b) 3.0 kW.

(c) 3.5 kW. (d) 4.0 kW.

Figure 4.8: *The melt pool width w_m as predicted by Model I (△), Model II (▽) and Model III (□), compared to the width observed in the camera images (–) 1.1 mm AA5182 sheets. The variation in the melt pool width calculated from the three different camera images is indicated with an error bar.*

shows that an increase of v results in a decrease of w_m, in the case of full penetration keyhole welding. This trend is accurately predicted by the FEM models.

The differences between the computed and the observed melt contours may be caused by several factors. First of all, it is not known how much of the laser power is absorbed during welding. In the models, it is assumed that under all welding conditions, maximally half of the supplied laser power is absorbed by the material ($P_a \leq 0.5P$). The amount of absorbed laser power is also influenced by the function $z_1(T)$ (Equation 4.1), which saturates the amount of absorbed laser power when the calculated temperature is larger than the keyhole wall temperature. It is well possible that in reality, the maximum value of P_a is a function of P and v, which would explain the strong dependance of l_m on v.

A second difference is that the melt contours computed with the FEM models are averaged over the sheet thickness. In the camera images, only the top contour of the melt pool is observed, which will be different from the melt pool dimensions below the sheet surface. Especially for large values of v, the melt contour may significantly vary over the sheet thickness.

Figure 4.6 shows that when the keyhole and melt pool do not penetrate the sheet (partial penetration), the contour of the melt pool on the top surface as observed in the camera images is larger than for full penetration keyhole welding. This indicates that the flow in the melt pool is different in the case of partial and full penetration keyhole welding. This effect is even more pronounced in the mild steel welding experiments, which are treated in the following section.

4.7 Experimental Verification for Mild Steel

FEM calculations using the three described model variations were also performed for mild steel (FeP04), using the same computational domain and mesh as where used for the computations for AA5182. Results of the calculations were compared to camera images of the welding process as well.

From the pressure balance at the keyhole wall for FeP04, the keyhole

wall temperature is approximately equal to the boiling temperature of Fe, which will be explained in Section 5.2. Therefore, in the FEM model calculations for FeP04, the keyhole wall temperature was set to the boiling temperature of Fe.

The results of the FEM model variations I ($L_m = 0$, $k = 40$ W/(m K), $c_p = 645$ J/(kg K)), II ($L_m = 2.67{\cdot}10^5$ J/kg, k and c_p idem) and III ($L_m = 2.67{\cdot}10^5$ J/kg, k and c_p are as given in Appendix C) are compared to the melt contour extracted from the camera images for twelve different combinations of P and v. Figure 4.9 compares the calculated and the observed melt contours.

As with the welding of aluminium, the melt contour calculated by Model I does not show a pronounced V-shaped tail which is seen in the camera images. The melt contours calculated with Models II and III do show this V-shape. This confirms the conclusion that the latent heat of the solid-liquid phase transition needs to be taken into account if a realistic estimation of the melt pool shape is desired [43].

Figure 4.9 shows, that the use of temperature dependent values of k and c_p (Model III) results in an estimated melt contour that is closer to the contour observed in the camera images, than when k and c_p are assumed to be constant (Model II). This shows that for FeP04, it is advisable to use temperature dependent values of k and c_p in the FEM model. This is probably due to the fact that for FeP04, c_p has larger relative variations as a function of the temperature than for AA5182. This becomes apparent when Figures C.1 and C.2 of Appendix C are compared.

Figure 4.9 also shows that the melt pool dimensions (l_m and w_m) estimated by the FEM models are close to the dimensions that are observed in the camera images. What little deviations noticed may be due to the fact that the melt contour of the models is an average over the entire sheet thickness, where as the camera images show the melt contour at the top surface. Figure 4.10 shows that the FEM calculations predict a small decrease in l_m with v when P is 2.5 or 3.0 kW, whereas l_m is constant with varying v when P is 3.5 or 4.0 kW. The actual sizes based on camera measurements indicate an increase in l_m with increasing values of v. When the penetration is partial, then l_m estimated from the images increases even

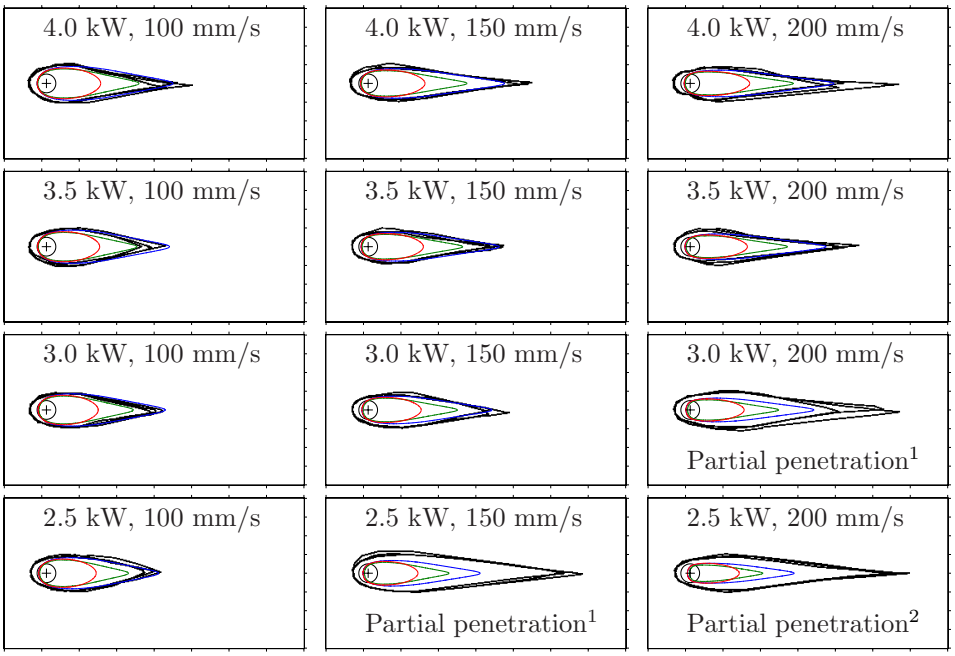

Figure 4.9: *The melt contours as predicted by* ***Model I*** *(constant c_p, constant k, $L_m = 0$),* ***Model II*** *(constant c_p, constant k, $L_m \neq 0$) and* ***Model III*** *($c_p(T)$, $k(T)$, $L_m \neq 0$), compared to the edges of the melt pool observed in three different* ***camera images*** *of the weld, for different values of laser power and welding speed, for 1.0 mm thick FeP04 sheets. The circle with the cross indicates the position and size of the laser spot.*

[1] Partial penetration of the keyhole, full penetration of the melt.
[2] Partial penetration of the keyhole and the melt.

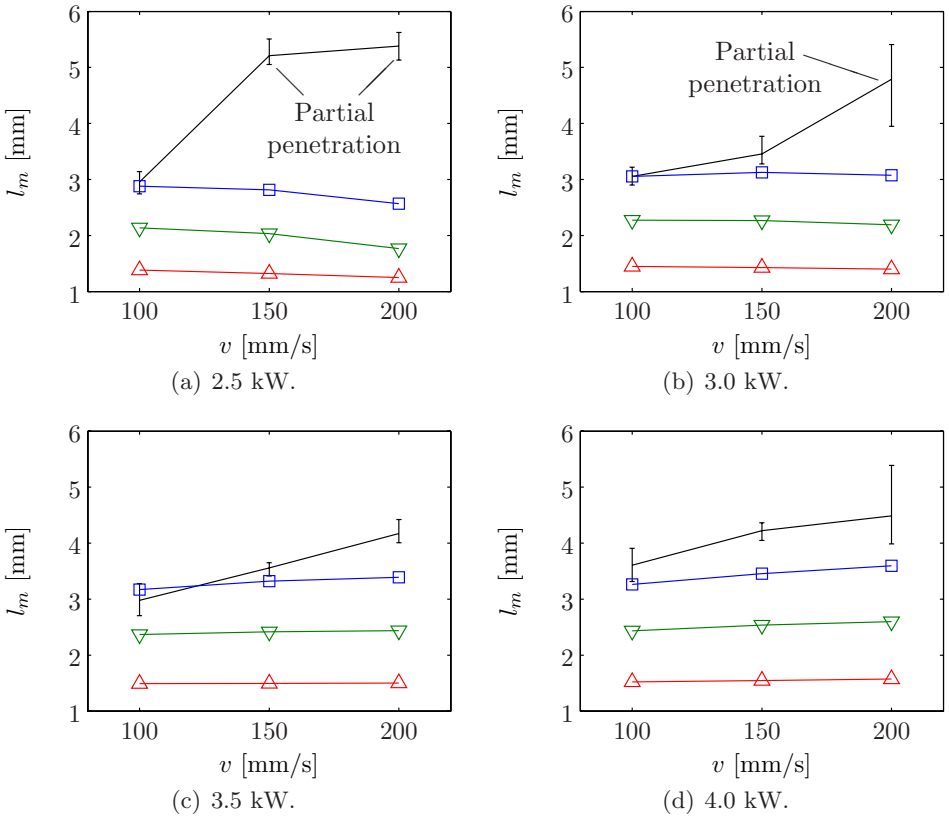

(a) 2.5 kW. (b) 3.0 kW.

(c) 3.5 kW. (d) 4.0 kW.

Figure 4.10: *The melt pool length l_m as predicted by Model I (△), Model II (▽) and Model III (□), compared to the length observed in the camera images (–) for 1.0 mm FeP04 sheets. The variation in the melt pool length calculated from the three different camera images is indicated with an error bar.*

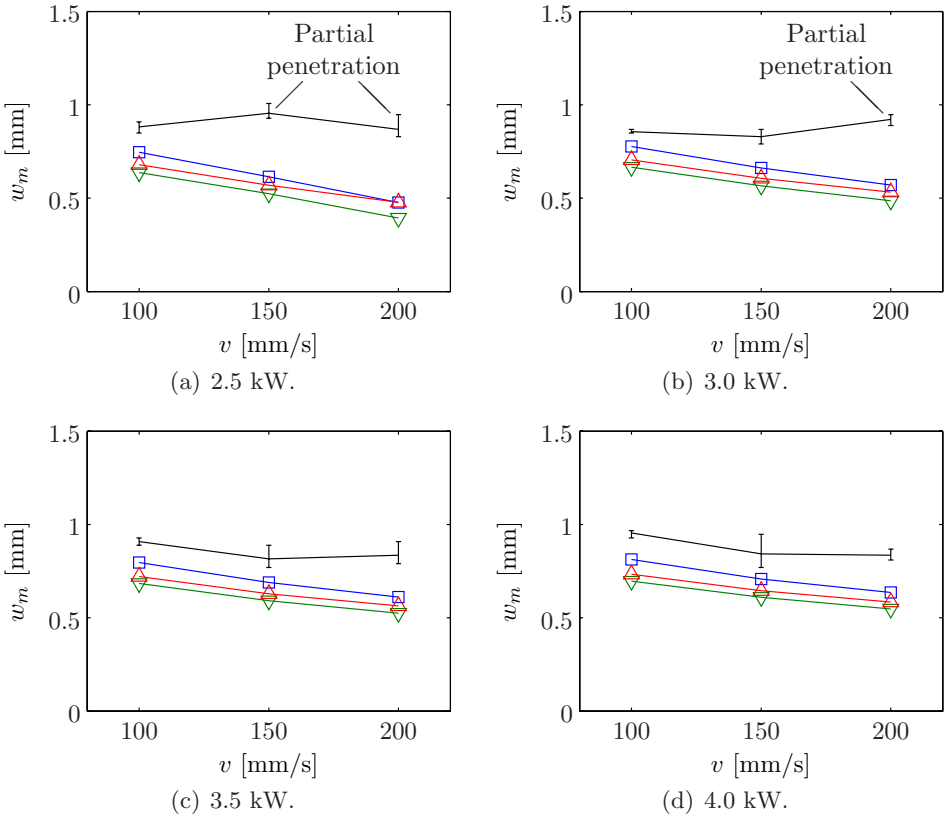

(a) 2.5 kW. (b) 3.0 kW.

(c) 3.5 kW. (d) 4.0 kW.

Figure 4.11: *The melt pool width w_m as predicted by Model I (△), Model II (▽) and Model III (□), compared to the width observed in the camera images (–) for 1.0 mm FeP04 sheets. The variation in the melt pool width calculated from the three different camera images is indicated with an error bar.*

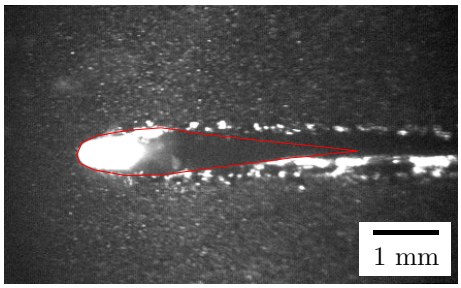

(a) $P = 3.0$ kW, $v = 200$ mm/s, partially penetrated keyhole.

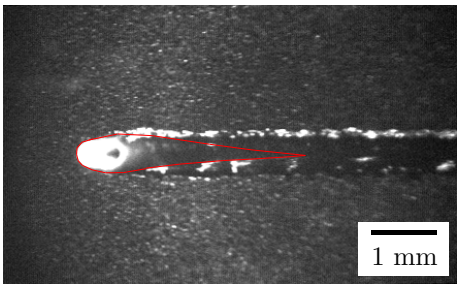

(b) $P = 3.5$ kW, $v = 200$ mm/s, fully penetrated keyhole.

Figure 4.12: *Camera images of the laser welding process of a 1.0 mm FeP04 sheet, with and without a fully penetrated keyhole. For both welds, the melt has fully penetrated the sheet. The dark spot inside the bright white area (right figure) indicates full penetration of the keyhole. The red lines indicate the melt contour.*

more.

Both the FEM model results and the camera image measurements show a decreasing value of w_m for increasing values of the welding speed, for the full penetration keyhole welding situation (Figure 4.11). When the keyhole does not penetrate the sheet, the width estimated from the camera images is much larger. In all cases the estimated melt pool width is smaller that observed in the camera images.

In general, for full penetration keyhole welding, the temperature distribution and melt flow predicted by the FEM models give a good insight in the physical processes that are present in the melt pool.

Figure 4.12 shows two camera images of the welding process. During the welding process shown in Figure 4.12(a), $P = 3.0$ kW and $v = 200$ mm/s. In Figure 4.12(b), these values are $P = 3.5$ kW and $v = 200$ mm/s. Examination of the resulting welds shows that in both cases the melt zone completely penetrates the sheet. However, from Figure 4.12(a) it can be seen that for $P = 3.0$ kW, there is no dark spot (image of the keyhole exit at the root surface of the sheet) visible inside the bright white area (the

place where the Nd:YAG laser directly irradiates the material). This means that in that case, the keyhole does not fully penetrate the sheet [17, 38]. In Figure 4.12(b) this dark spot is visible, which indicates that the keyhole does penetrate the sheet fully.

In Figures 4.9, 4.10 and 4.11 it can be seen that when the keyhole only partially penetrates the sheet, the melt pool dimensions on the top surface (determined from camera images) are significantly larger than in welds where the keyhole fully penetrates the sheet. This indicates that the melt flow is different during partial and full penetration keyhole welding. More precisely with the insight from Figure 4.12, this difference is directly related to the full penetration of the keyhole. It is suspected that this is caused by a stronger upward flow in the melt pool in the case of partial penetration of the keyhole, which is caused by the different shape of the keyhole when the keyhole fully or partially penetrates the sheet.

4.8 Conclusions

A FEM model has been developed, which calculates the temperature distribution and the fluid flow in and around the weld zone, assuming 2D flow. For the keyhole laser welding process for both AA5182 and FeP04, this model can predict the melt pool contours in a qualitative way.

- The latent heat of liquid-solid phase transition causes the distinctive V-shape of the melt pool, which is observed in camera images of the welding process. The V-shape is caused by a combination of a locally increased heat capacity of the material around the melt temperature due to the liquid-solid phase transition and the convection due to the welding speed. Only the isotherms within the melt trajectory have this V-shape.

- The use of a temperature dependent thermal conductivity and specific heat improves the predictions of the melt contour. For AA5182 (Figure 4.6), the improvement is small, but for FeP04 (Figure 4.9) the melt contour prediction improves significantly. This may be caused

by the fact that for FeP04, the specific heat varies more as a function of the temperature than for AA5182.

- Partial penetration of the keyhole through the melt pool, results in a significantly enlarged melt contour at the top surface compared to the melt pool contour in the case of full keyhole penetration. This is probably due to a stronger upward flow in the melt pool, in the case with a partially penetrated keyhole.

Chapter 5

Keyhole Shape

During the keyhole laser welding process, the shape of the keyhole and surrounding melt pool has a very important influence on the resulting weld quality. Welding experiments show that the state of the laser welding process can change dramatically for relatively small changes in process settings. As will be outlined in Section 5.1, the resulting top and bottom weld surfaces show very distinct structures. When certain welding parameters are used, the welding process is quite susceptible for holes in the resulting weld bead. The presence of these holes is strongly related to the keyhole shape.

To understand which forces drive keyhole shape changes, the different pressure components at the keyhole wall have been investigated. An estimation of the order of magnitude of the different pressure terms at the keyhole wall is described in Section 5.2. Section 5.3 discusses on how an imbalance between the pressure components can lead to an elongation of the keyhole. In Sections 5.4 and 5.5, the model is compared with camera images of the keyhole shape during welding of aluminium and mild steel sheets, respectively. Finally Section 5.6, summarises the conclusions of this chapter. Parts of this work have been published earlier [54, 55].

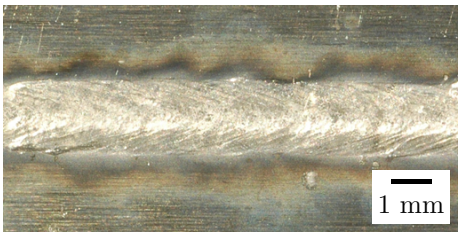

(a) Weld bead with V-shaped striations (circular keyhole during welding).

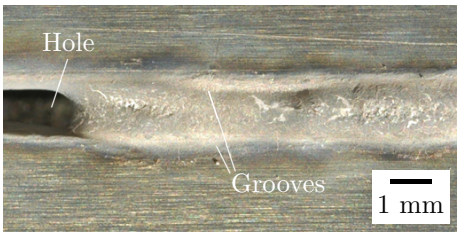

(b) Weld bead with smooth surface, grooves and holes (elongated keyhole during welding).

Figure 5.1: *The appearance of top surfaces of weld beads obtained, with different keyhole shapes during welding (1.1 mm AA5182 sheets).*

5.1 Keyhole Shape Variations

Full penetration keyhole laser welding experiments of aluminium sheets show that the top surface of the weld bead can have two distinct appearances, based on the welding parameters used. Most welds have a weld bead with distinctive V-shaped striations (Figure 5.1(a)). Occasionally, the bead is smoother but shows grooves along the side of the bead (Figure 5.1(b)). This latter welding mode is subjectable to holes in the weld bead.

The origin of these different weld bead appearances has been investigated using the camera-based monitoring system described in Chapter 3. It was found that these differences are related to the keyhole shapes formed during welding. For the traditional welds with the V-shaped striations, the top view of the keyhole is approximately circular, whereas for welds with the smoother surface, an elongated keyhole geometry is observed. Figures 5.2 and 5.3 show camera images of the circular and the elongated keyholes formed during the bead-on-plate welding of AA5182 sheets.

Using the developed monitoring system, high-speed recordings of the circular and elongated keyhole welding modes have been made. Figures 5.4 and 5.5 show images recorded using a frame rate of 10 kHz and an exposure time of 90 μs. These welds were performed with a welding speed of 80 mm/s

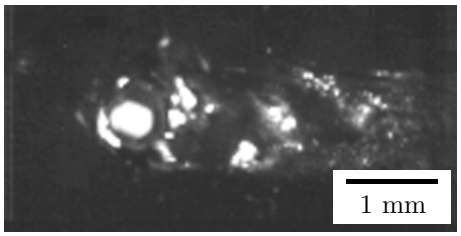

(a) Camera image.

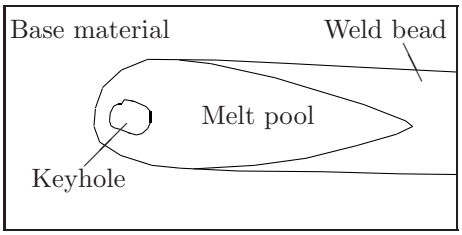

(b) Schematic overview.

Figure 5.2: *Camera image of the laser welding process, with a circular shaped keyhole.*

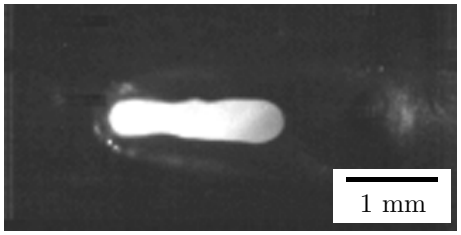

(a) Camera image.

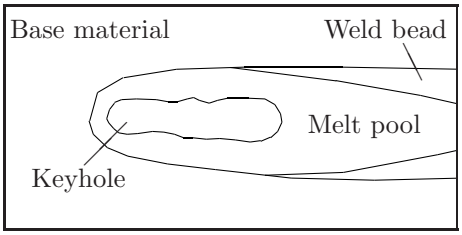

(b) Schematic overview.

Figure 5.3: *Camera image of the laser welding process, with an elongated keyhole.*

and 3 kW of laser power. Due to small changes in the illumination setup and different camera settings, these images have a slightly different appearance as the high speed camera images shown in Figures 5.2 and 5.3.

The images in Figure 5.4 show that the keyhole elongates slowly, compared to the time scale of the keyhole and melt pool surface oscillations (the elongation continues for several hundreds of milliseconds, whereas keyhole fluctuations have time scales typically smaller than one millisecond). In Figure 5.4(c) the keyhole length is approximately 2.6 mm, and the width of the keyhole is 1.0 mm. The laser focal diameter is 0.45 mm. The focus position of the laser beam is placed 1 mm above the top surface, which results in a laser spot diameter on the top surface is 0.59 mm.

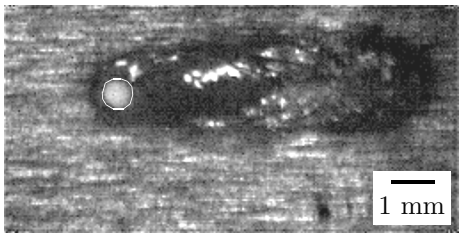

(a) t = 0 ms

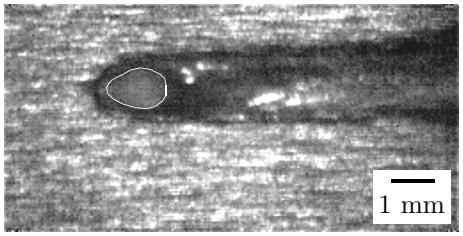

(b) t = 100 ms

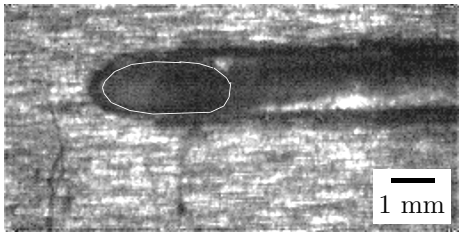

(c) t = 200 ms

Figure 5.4: *High-speed images of the transition from the circular to the elongated keyhole welding mode. The white lines indicate the keyhole outline.*

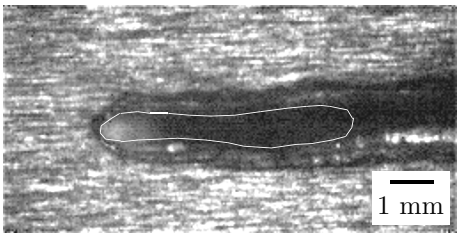

(a) t = 0 ms

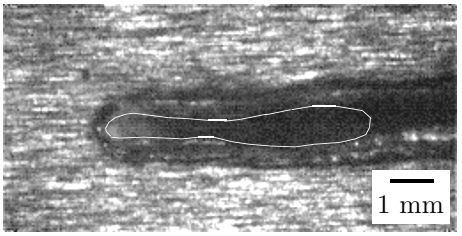

(b) t = 5.0 ms

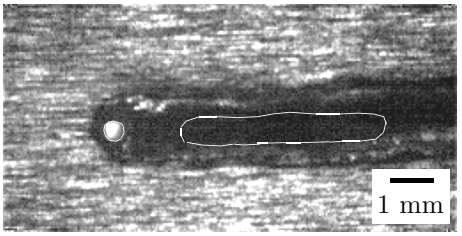

(c) t = 10.0 ms

Figure 5.5: *High-speed images of the transition from the elongated to the circular keyhole welding mode. The white lines indicate the keyhole outline.*

When the keyhole is elongated (Figure 5.5), the fluid flows on both sides of the keyhole are subjected to small capillary surface waves, which originate at the front keyhole wall. While the keyhole elongates, the probability that two surface waves at each side of the keyhole collide increases. When this happens, the elongated keyhole will break into two sections (Figure 5.5(c)): a leading circular keyhole at the position of the laser spot and a lagging elongated keyhole. The lagging keyhole does not close and will remain as a welding defect after solidification. As Figure 5.5 shows, the transition from the elongated to the elongated keyhole welding mode takes only about 10 ms. In the next section, the process conditions that govern elongation are considered.

5.2 Pressure Terms at the Keyhole Wall

Since the keyhole elongates slowly compared to the other keyhole dynamics like capillary surface waves, the process is considered quasi-static. The keyhole is surrounded by a pool of molten metal. The keyhole and melt pool are separated by a free moving surface. The quasi-static behaviour of the keyhole is studied by considering the pressure balance at this surface.

A model has been developed that describes the pressure balance at the keyhole wall for the full penetration keyhole welding of thin sheets. The key difference of this model compared to existing keyhole models, is the incorporation of the doubly curved shape of the keyhole and melt pool surface. The surface tension pressure term consists of two parts. One part tries to close the keyhole and the second part tries to open the keyhole. When the plate thickness becomes comparable to the keyhole diameter, this second part of the surface tension pressure term becomes dominant and causes the keyhole elongation, eventually resulting in holes.

5.2.1 Pressure Balance

For a stationary keyhole with a high aspect ratio, the pressure balance is given by Duley [1]

	AA5182	FeP04
P [kW]	4.0	
v [mm/s]	100	
r_s [mm]	0.225	
I [W/m^2]	$2.5 \cdot 10^{10}$	
r_1[1] [mm]	0.15-0.30	0.10-0.18
r_2[2] [mm]	0.55	0.50
c_2[3]	0.9-1.2	0.6-0.8
b [mm]	1.1	1.0

Table 5.1: *Values of the process parameters used for the evaluation of the different pressure terms.*

[1]Determined from camera images.
[2]Using the approximation that $r_2 = b/2$.
[3]Calculated using $c_2 = r_1/r_s$.

$$p_i + p_d + p_r - p_s - p_\gamma = 0, \tag{5.1}$$

where p_i is the radiation pressure, p_d is the hydrodynamical pressure, p_r is the recoil pressure, p_s is the hydrostatical pressure and p_γ is the surface tension pressure.

The surface tension pressure p_γ depends on the surface tension γ and the radius of curvature r of the free surface. In many models, the keyhole is often approximated as a cylinder, with a radius approximately equal to the laser spot radius r_s [56, 57, 58]. In that case, p_γ can be written as [1]

$$p_\gamma = \frac{\gamma}{r_s}. \tag{5.2}$$

However, for thin sheets, a second radius needs to be taken into account. As illustrated in Figure 5.6(a), the keyhole surface can be described as the inner part of a toroid. The curvature is described by two radii r_1 and r_2, both of which contribute to the surface tension pressure term

5.2 Pressure Terms at the Keyhole Wall

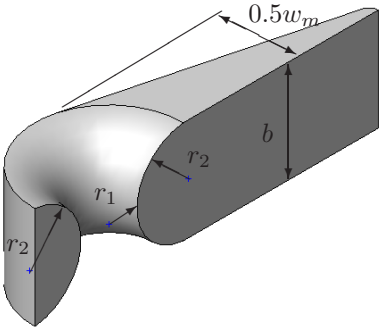

(a) Circular keyhole shape.

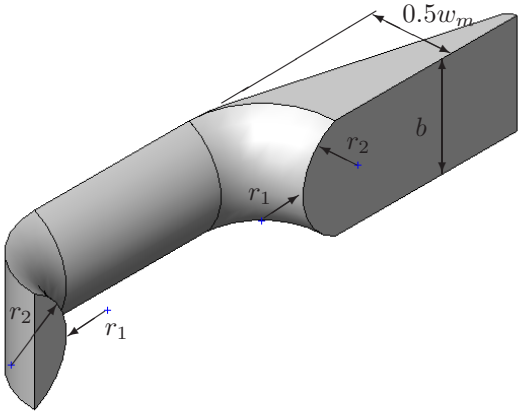

(b) Elongated keyhole shape.

Figure 5.6: *Cross section of the approximate melt pool shapes in the different welding modes.*

$$\begin{aligned} p_{\gamma c} &= \frac{\gamma}{r_1} \\ p_{\gamma o} &= \frac{\gamma}{r_2} \\ p_{\gamma} &= p_{\gamma c} - p_{\gamma o}, \end{aligned} \tag{5.3}$$

where r_1 and r_2 describe a concave and convex curvature contribution respectively. Hence their contributions to p_γ will have opposite signs. For full penetration keyhole welding of thin plates, the pressure balance given in Equation 5.1 now becomes

$$p_i + p_d + p_r + p_{\gamma o} = p_s + p_{\gamma c}, \tag{5.4}$$

where the right-hand terms try to close, and the left-hand terms try to open the keyhole.

All six pressure terms are estimated for a combination of laser power P and welding speed v. Table 5.1 gives typical process settings. Relevant material parameters can be found in Appendix C. Some of the entries in this table will be discussed later in this section. The resulting pressures are summarised in Table 5.2. It appears that p_i, p_d and p_s are significantly smaller than $p_{\gamma c}$, $p_{\gamma o}$ and p_r. Therefore the former are neglected in this model, simplifying the pressure balance to

$$p_r + p_{\gamma o} = p_{\gamma c}. \tag{5.5}$$

5.2.2 Surface Tension Pressure

The surface tension γ of a material depends on its chemical composition. For AA5182, which contains a significant amount of magnesium (4.9%), the surface tension approximately equals 0.6 N/m [59]. The surface tension of steel is dependent on the amount of oxygen and sulfur in the melt. Since the welding process is shielded from the environment using an inert shielding

	AA5182	FeP04
p_i [Pa]	67	53
p_d [Pa]	$1.0{\cdot}10^2$	$2.7{\cdot}10^2$
p_s [Pa]	26	66
p_r [Pa]	$1.8{\cdot}10^3$	$8.5{\cdot}10^4$
$p_{\gamma c}$ [Pa]	$3.0\cdot10^3$	$1.2\cdot10^4$
$p_{\gamma o}$ [Pa]	$1.0\cdot10^3$	$3.2\cdot10^3$

Table 5.2: *Order of magnitude of the maximum value of the different pressure terms.*

gas, the oxygen level in the molten material is low. For FeP04, which contains 0.013% sulfur, γ is approximately 1.6 N/m [59].

The closing surface tension pressure term $p_{\gamma c}$ depends on the smallest keyhole radius r_1 (Figure 5.6(a)) and has been determined from camera images. Typical values are given in Table 5.1. For the opening term $p_{\gamma o}$, the radius r_2 needs to be known. Based on observations of the melt flow around the keyhole from camera images, r_2 is approximately half of the sheet thickness b. The resulting surface tension pressure terms are given in Table 5.2.

5.2.3 Radiation Pressure

The radiation pressure p_i is given by [1]

$$p_i = \frac{I}{c}(A + 2R), \tag{5.6}$$

with I the irradiance of the laser light at the surface, c the speed of light, A the absorptivity of the laser light at the surface and R the reflectivity at the surface. Since all incident laser radiation is either absorbed or reflected by the workpiece, the following holds

$$A + R = 1, \tag{5.7}$$

which gives

$$p_i = \frac{I}{c}(2 - A). \tag{5.8}$$

For the proposed welding conditions, p_i will be about 67 Pa and 53 Pa for AA5182 and FeP04, respectively.

5.2.4 Hydrodynamical Pressure

The melt flow around the keyhole is assumed to be non-rotational, incompressible, and laminar (Appendix D). Then, the hydrodynamical pressure term p_d can be expressed as [1, 60]

$$p_d = \frac{1}{2}\rho\left(v_A^2 - v_B^2\right). \tag{5.9}$$

Here ρ is the density and v_A and v_B are the melt flow velocities at two positions in the melt flow around the keyhole on the same streamline. For both the laser welding processes of AA5182 and FeP04 sheets, the flow velocities around the keyhole are between one and three times the welding speed, as shown in Figure 4.5(a) on page 73. This means that at maximum p_d is about $1.0{\cdot}10^2$ Pa and $2.7{\cdot}10^2$ Pa for AA5182 and FeP04, respectively.

5.2.5 Hydrostatical Pressure

The hydrostatic pressure p_s is defined as [1]

$$p_s = \rho g x_3, \tag{5.10}$$

where g is the gravitational acceleration and x_3 is a spatial coordinate parallel to the gravitational field (Figure 4.1 on page 64). For the considered AA5182 sheets, p_s can have a maximum value of 26 Pa. For FeP04, p_s is always smaller than 66 Pa.

5.2.6 Recoil Pressure

For an ideal gas, the recoil pressure p_r is related to the surface temperature T_k according to [37, 61]

$$p_r = c_0(p_v - p_a), \tag{5.11}$$

with p_v the vapour pressure

$$p_v = p_0 e^{c_1(1-\frac{T_b}{T_k})}. \tag{5.12}$$

Here p_a is the ambient pressure, p_0 the atmospheric pressure, T_b the normal boiling temperature and $c_1 = L_v/(RT_b)$. L_v is the latent heat of evaporation and R is the molar gas constant. The constant c_0 represents the pressure reduction at the surface due to recondensation from the vaporised cloud near the surface. For high pressures, this value is approximately 0.5 [62].

Under normal welding conditions, it is assumed that the ambient pressure equals the atmospheric pressure ($p_a \approx p_0$). Equation 5.12 is valid for $T_b \leq T_k \leq T_c$, where T_c is the critical temperature of the material. It can be simplified by application of the Trouton-Hildebrand-Everett rule [63]

$$\frac{L_v}{RT_b} = 4.0 + \ln T_b. \tag{5.13}$$

Figure 5.7 shows p_v as function of the keyhole surface temperature T_k for Al, Mg and Fe using Equations 5.11, 5.12 and 5.13. This figure shows that p_v depends strongly on the surface temperature T_k. Since T_k is unknown, it is not possible to give a direct estimate of p_r using this approach. However, for the proposed welding conditions, the keyhole is not elongated and the pressure terms that tend to open the keyhole are balanced by the pressure terms that try to close it. Since all terms but p_r are known, p_r can be estimated using Equation 5.4. For AA5182, this gives $p_r = 1.8 \cdot 10^3$ Pa (relative pressure), which means that $p_v = 1.036 \cdot 10^5$ Pa (absolute pressure), which is only slightly above p_0 ($p_0 = 1.0 \cdot 10^5$ Pa). This results in a surface temperature which is just above the normal boiling temperature. Due to the high Mg content of this alloy and the low boiling temperature of Mg (T_b = 1363 K), it is assumed that the vapour pressure is mainly caused by Mg atoms. In this case the surface temperature is estimated to be 1367 K. For FeP04, $p_v = 1.170 \cdot 10^5$ Pa (absolute pressure), which results in a surface temperature of 3175 K. This is just above the boiling temperature of Fe.

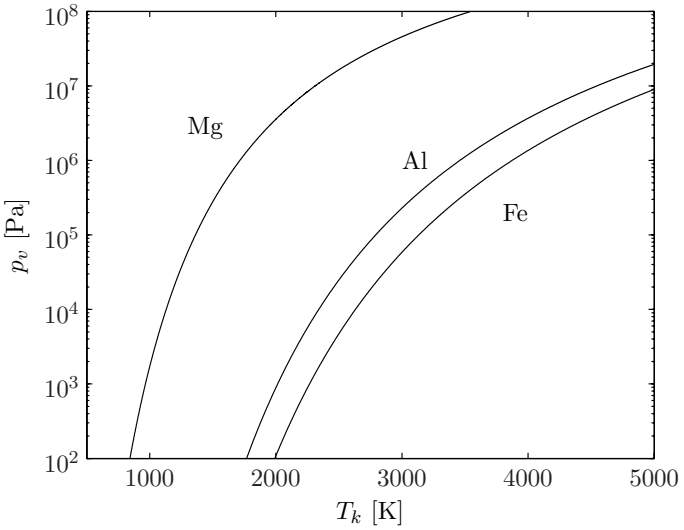

Figure 5.7: *The recoil pressure p_v as a function of the keyhole surface temperature T_k for various materials.*

5.3 Keyhole Elongation and Weld Bead Formation

The keyhole radius r_1 (Figure 5.6) has the same order of magnitude as the spot radius r_s. To incorporate small differences between the keyhole and the spot radii, r_1 is expressed as a fraction of r_s: $r_1 \approx c_2\ r_s$. The proportionality constant c_2 will have a value close to one and can be determined from camera images. The radius r_2 is expressed as a function of the sheet thickness: $r_2 \approx b/2$. Then Equation 5.3 can be rewritten as

$$\begin{aligned} p_{\gamma c} &= \frac{\gamma}{c_2 r_s} \\ p_{\gamma o} &= \frac{2\gamma}{b}, \end{aligned} \tag{5.14}$$

and that the pressure balance in Equation 5.5 can be written as follows

$$p_r + \frac{2\gamma}{b} = \frac{\gamma}{c_2 r_s}. \tag{5.15}$$

One immediate observation from this analysis is that a large laser spot radius r_s will result in a small $p_{\gamma c}$. When the sheet thickness remains unchanged, the right-hand side of Equation 5.15 can no longer balance the left-hand side. This means that the keyhole wall is not stationary and will move away from the laser spot. At the front wall, the keyhole surface cannot move due to the solid-liquid interface. Instead, the liquid film is pressed against the solid material, which locally will increase r_2 (and r_2 becomes larger than $b/2$) until a stationary geometry is reached. However, at the rear keyhole wall, the surface can move away and the keyhole will elongate. This elongation can be considerable, as shown in Figure 5.5 on page 92.

The weld bead formation can be understood from the resulting fluid flow. Figure 5.1 shows the appearance of the top bead of welds with a circular and an elongated keyhole formed during welding. The elongated keyhole weld bead shows distinctive grooves along the sides of the weld bead length. These grooves are clearly visible in the cross sections (Figure 5.8). The formation of these grooves is explained in Figure 5.9, which shows schematically the top view of the welding process with the elongated keyhole (bottom figure) and the cross section at different positions (top figures). When the keyhole is elongated, the molten material has to travel a longer way along the length to the end of the keyhole. In this part of the melt pool (between cross sections I and II), the melt will start to cool down. Some of the material will solidify before the rear keyhole wall is reached, as illustrated in cross section II. The shape of these solidified layers on each side of the weld is the initial stage of the groove formation. When the two flows come together, the melt pool will have a shape as indicated in Cross section III. After solidification of the rest of the melt the weld has the shape as shown in Figure 5.8(b).

Figure 5.1 also shows that the top surface is rather rough when the keyhole is circular. From movies of the camera images it can be seen that

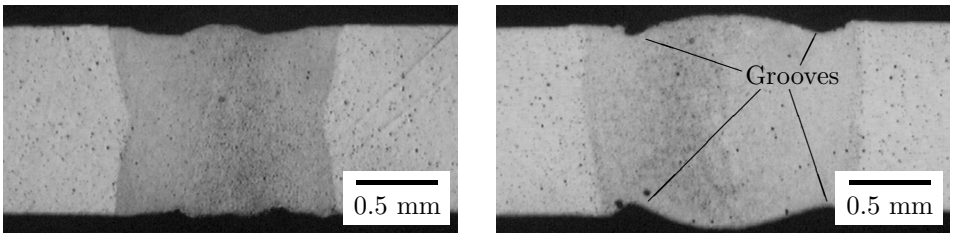

(a) Circular keyhole during welding. (b) Elongated keyhole during welding.

Figure 5.8: *Cross sections of a welded 1.1 mm AA5182 sheet, with different shapes of the keyhole during welding.*

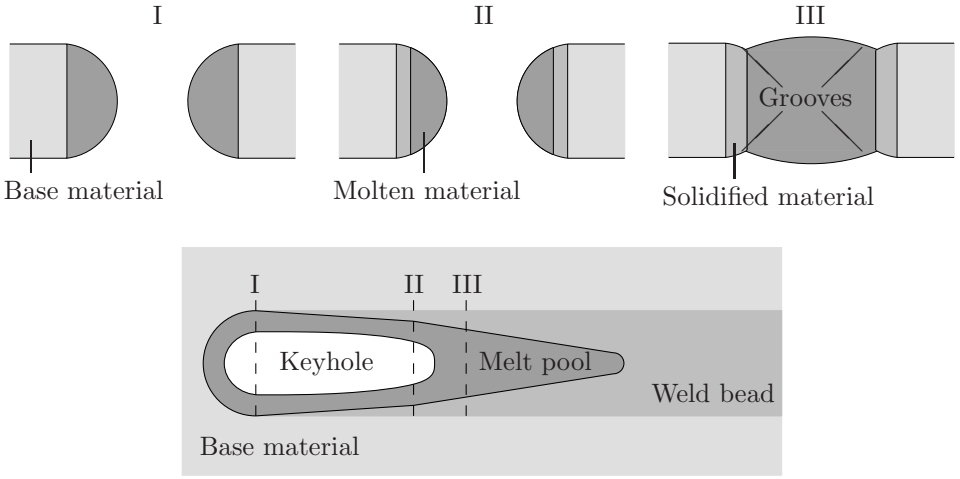

Figure 5.9: *Schematic drawing of the welding process to illustrate the formation of the grooves along the side of the elongated keyhole weld bead.*

in this case, the rear part of the keyhole oscillates strongly. This causes strong capillary surface waves on the melt pool. These waves are "frozen" in the weld bead when the melt pool solidifies and this creates the V-shaped striations. This unstable behaviour of the keyhole rear wall has already been treated in other publications [64]. In case of the elongated keyhole, the keyhole rear wall moves away from the front keyhole wall and no longer oscillates in and out of the laser beam. This reduces the surface waves considerably and results in a smoother weld bead. Additionally, surface waves generated by the front keyhole wall need to travel much further and are damped more before they reach the melt pool. The difference in surface waves of the melt pool can also be observed in Figures 5.2 and 5.3, where the circular keyhole melt pool shows much more bright spots alternated with dark shadows that are caused by an uneven surface due to surface waves.

When the keyhole is elongated, capillary surface waves travel along the keyhole side wall. In Figure 5.3, these waves can be observed. As mentioned before, when two surface waves at each side of the keyhole collide, the two sides will form a new rear keyhole wall. This hole will not close due to the surface tension pressure and will remain as a hole in the weld bead after solidification. Therefore, the keyhole welding process becomes more susceptible to welding defects when the keyhole elongates.

5.4 Experimental Verification for Aluminium

To verify the keyhole elongation model, in-situ camera images were recorded during the Nd:YAG laser welding process of thin AA5182 sheets. Bead-on-plate welding experiments were carried out using a laser power of 4 kW and a welding speed of 100 or 150 mm/s. The experiments were performed using the same laser welding setup which is described in Section 2.4 on Page 26. The monitoring system described in Section 3.2 was used to visualise the keyhole during the welding process. To quantify the keyhole elongation, the ratio R_k of the keyhole length l_k to width w_k is defined as

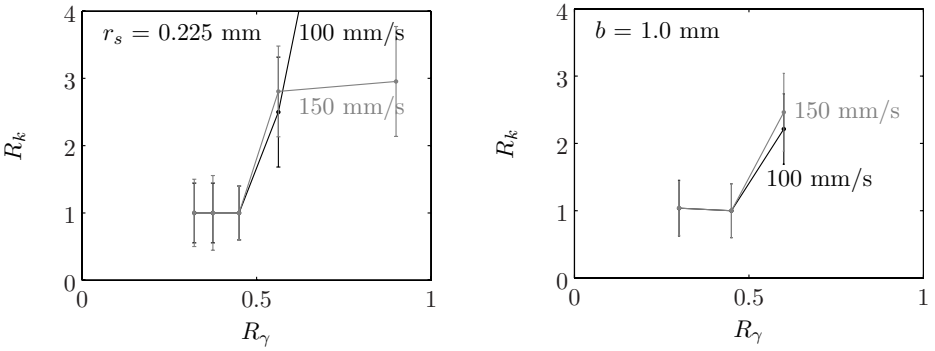

(a) Various thicknesses. (b) Various spot diameters.

Figure 5.10: *The ratio R_k of the keyhole length l_k and width w_k for different values of R_γ during the welding of AA5182. The error bars indicate the fluctuation in keyhole geometry during welding.*

$$R_k = \frac{l_k}{w_k}, \tag{5.16}$$

which was determined for each experiment from the camera images. When this ratio is larger than one, the keyhole is no longer circular but has an elongated shape.

To verify if the keyhole elongation is indeed caused by the doubly curved nature of the rear keyhole wall, R_k can be evaluated for different values of the ratio r_1/r_2 (Figure 5.6(a)). Experimentally, r_1 and r_2 can be determined directly using a camera-based monitoring system. To develop guidelines for welding parameters that are directly applicable, the ratio r_1/r_2 is approximated. As mentioned in Section 5.3, $r_1 \approx c_2\ r_s$ and $r_2 \approx b/2$. So r_1/r_2 can be approximated by

$$R_\gamma = \frac{2c_2 r_s}{b}. \tag{5.17}$$

For AA5182, c_2 is approximately 1.0. R_γ as defined in Equation 5.17, contains parameters (the laser spot radius and the sheet thickness) which

can be determined easily for most situations.

In a first set of experiments, a fixed spot radius $r_s = 0.225$ mm is used for welding sheets with thicknesses b ranging from 0.5 to 1.4 mm (Figure 5.10(a)). The graph shows how the values of R_k become significantly larger than one as R_γ becomes larger than 0.5. An extreme case is found for v = 100 mm/s and $R_\gamma = 0.9$ ($b = 0.5$ mm and $r_s = 0.225$ mm), where the melt flows around the laser spot, along the two sides of the sheet, but the flows do not join again in a combined melt pool. This means that the laser welding process becomes more a laser cutting process. This results in a very high value of R_k (in Figure 5.10(a), R_k is off the scale for these welding conditions).

In a second set of experiments, three different values for the spot radius were used (0.15 mm, 0.225 mm and 0.30 mm), in combination with 1.0 mm thick sheets. Figure 5.10(b) shows that also under these conditions, R_k is significantly larger than one when R_γ is larger than approximately 0.5.

These experiments show that for AA5182, keyhole elongation is observed when $r_s > 0.25\ b$. This is valid both when the thickness b is varied while keeping the laser spot radius r_s constant, and when r_s is varied while keeping b constant. This confirms the predictions of the keyhole elongation model.

5.5 Experimental Verification for Mild Steel

To verify the predictions of the keyhole elongation model for FeP04, camera images were recorded during laser welding experiments in a similar way as performed for AA5182. Bead-on-plate welding experiments were carried out for thin FeP04 sheets, using 4 kW of laser power and a welding speed of 100 or 150 mm/s. The keyhole elongation is again evaluated by comparing R_k (Equation 5.16) and R_γ (Equation 5.17). For FeP04, c_2 is approximately 0.7, which was determined by comparing the keyhole radius observed in camera images with the radius of the laser spot.

Figure 5.11 shows that for $v = 150$ mm/s, R_k is larger than one (elongated keyhole) for values of R_γ larger than about 0.4 to 0.5. In these

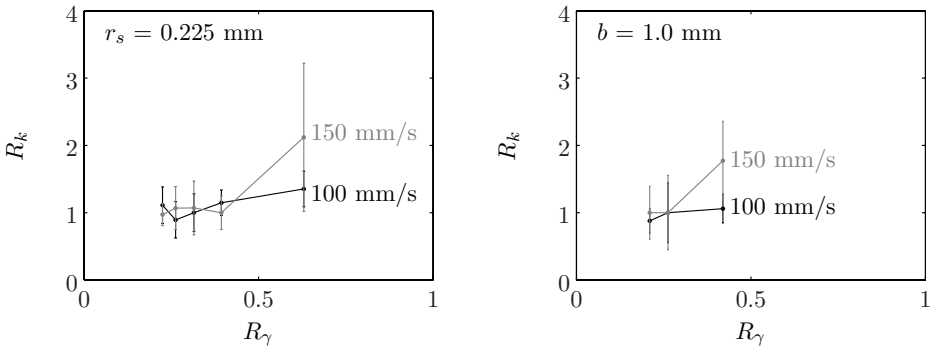

(a) Various thicknesses. (b) Various spot diameters.

Figure 5.11: *The ratio R_k of the keyhole length l_k and width w_k for different values of R_γ during the welding of FeP04. The error bars indicate the fluctuation in keyhole geometry during welding.*

experiments therefore a keyhole elongation occurs if $r_s > 0.4\ b$. For a welding speed of 100 mm/s, the elongation is less pronounced. It is expected that for higher values of R_γ the keyhole elongation will also manifest at welding speeds below 150 mm/s. This dependency of the elongation on the welding speed can be caused by a contribution of the hydrodynamical pressure term. This contribution is neglected in the current model. For AA5182 this dependency could not be observed, which may be due to the fact that the hydrodynamical pressure term is significantly smaller in the case of AA5182 compared to FeP04 (see Table 5.2).

The experiments show, that also for FeP04, keyhole elongation is observed, either when the spot size is increased while the material thickness is kept constant, or when the sheet thickness is decreased at a constant spot size. This observation is similar to that seen for AA5182. In general it may be concluded that the observed keyhole elongation effect is indeed caused by the surface tension pressure as described in Section 5.3. Therefore, if thin sheets and foils are to be welded, the laser spot needs to be sufficiently small to prevent keyhole elongation.

5.6 Conclusions

- The top view keyhole shape is monitored with the developed camera system (Chapter 3). As long as the keyhole is approximately circular in shape, this results in a weld bead with distinctive V-shaped striations. Occasionally, the keyhole is more elongated. This results in a weld bead which is smoother, yet shows grooves along the side of the bead. Furthermore, this welding mode results in holes in the weld bead and is hence not preferred.

- An evaluation of the different pressure terms acting on the keyhole wall show that the surface tension and recoil pressure terms are dominant.

- Since the keyhole shape is doubly curved, the surface tension pressure term has two contributions. One tries to close the keyhole and the other tries to open it. If the keyhole diameter is large compared to the sheet thickness, the latter is dominant and the keyhole elongates.

- Evaluation of the recoil pressure indicates that the keyhole wall temperature is just over the normal boiling temperature of the element in the alloy (present in significant quantities) with the lowest boiling temperature. For AA5182, this element is Mg and for FeP04 this is Fe.

- Keyhole elongation occurs if $r_s > 0.25b$ for AA5182 or $r_s > 0.4b$ for FeP04, where r_s is the laser spot radius and b is the sheet thickness.

Chapter 6

Gap Bridging with Laser-Based Welding Processes

In the case of a butt weld configuration, the small dimensions of the focussed laser spot imposes strict geometrical tolerances on the sheet edges to be welded. The welding process is very sensitive for gaps between the sheets. The gap bridging capability of a welding process is the ability of a this process to deliver sound welds in the presence of gaps between the sheets. A laser welding process with improved gap bridging capabilities would increase the applicability of laser welding in industry, which in turn will improve the production speed and weld quality.

In this chapter, several laser welding techniques are discussed, which can be used for the welding of aluminium Tailor Welded Blanks (TWB's). The gap bridging capabilities of these processes will be evaluated. The conventional Single Spot laser welding (SS) process has already been discussed in Chapter 1. The Twin Spot laser welding (TS) technique is reported to be better suited for the laser welding of aluminium sheets [65, 66, 67]. Section 6.1 discusses how twin spot laser welding can be used for the aluminium TWB production and what the specific advantages and disadvantages are.

In Section 6.2 how the SS and TS processes can be combined with cold wire feeding will be explained. It is expected that this can increase the tolerance of these welding processes for gaps between the sheet edges [1, 68, 69].

In recent years much research has been conducted in combining the laser welding process with the GMA welding process [70, 71, 72]. These authors report that the combined process, the so-called Hybrid Laser/GMA welding (HLG) process, is more tolerant for seam gaps and that high processing speeds are possible. In Section 6.3 the application of the hybrid laser/GMA welding process for aluminium TWB production will be discussed.

In Section 6.4, the different laser-based welding processes will be tested for their gap bridging capabilities during welding of thin aluminium sheets. The weld quality of sheets welded with a preset gap between the sheet edges, is tested using testing methods like visual inspection of the weld bead, microscopic inspection of the cross sections, microhardness measurements, tensile tests and Erichsen cupping tests. In this way, the applicability of the different processes for the aluminium TWB production will be evaluated. Some of the results of this work have been published earlier [29, 30, 73].

6.1 Twin Spot Laser Welding

In this section, a description will be given on the Twin Spot laser welding (TS) equipment that was used. Also the most important properties of the TS process are discussed.

For the Twin Spot laser welding (TS) process, the same Nd:YAG laser, beam delivery fiber and manipulator are used as done for the Single Spot laser welding (SS) process (Page 26). However, the welding head is different in the case of the TS process. Inside the twin spot welding head (Figures 6.1 and 6.2), the diverging laser beam coming from the optical fibre is collimated by the collimator lens. A prism is placed in a part of the collimated beam. This splits the beam into an unadjusted part (that part of the beam that does not pass through the prism) and another part that is deflected by a few degrees (that part of the beam that passes through

Figure 6.1: *Photo of the BEO D70 Trumpf twin spot laser welding head.*

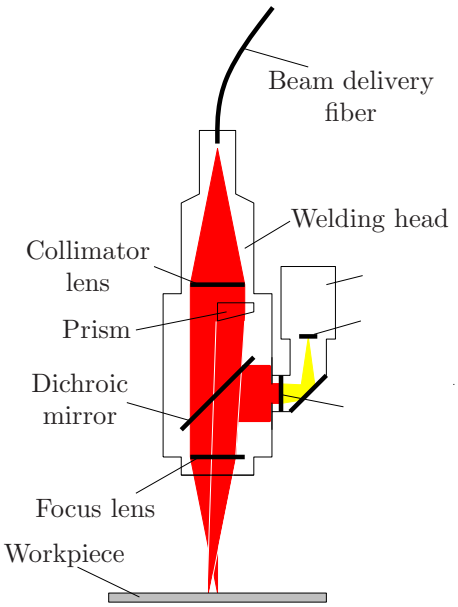

Figure 6.2: *Schematic overview of a TS head.*

the prism). Both the deflected and the undeflected parts of the beam then pass through the dichroic mirror and the focus lens. At the workpiece, both parts of the beam form separate laser spots of 0.45 mm in diameter. For the laser welding of aluminium, the use of two laser spots is reported to have advantages over the use of a single spot [65, 66, 67].

With regard to the gap bridging capabilities, it may be advantageous to use a TS process with a parallel configuration (Figure 6.4). If a gap is present between the sheet edges, a part of the laser light will escape through this gap in case of the SS process (Figure 6.5). This reduces the amount of laser light effectively used for welding. By using the TS process with a

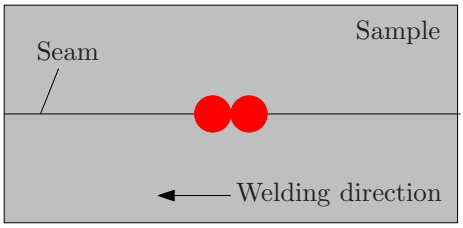

Figure 6.3: *Laser spot placement in the serial twin spot welding configuration.*

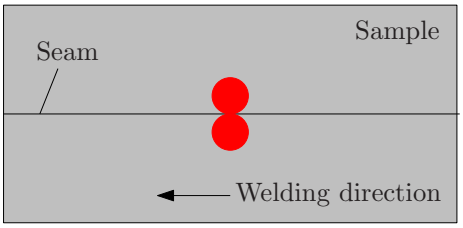

Figure 6.4: *Laser spot placement in the parallel twin spot welding configuration.*

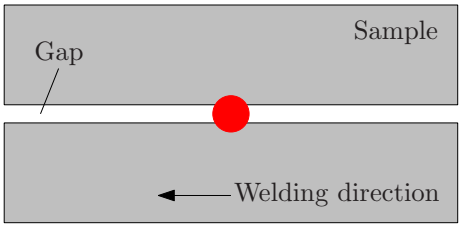

Figure 6.5: *Laser light escapes through the gap for the SS process.*

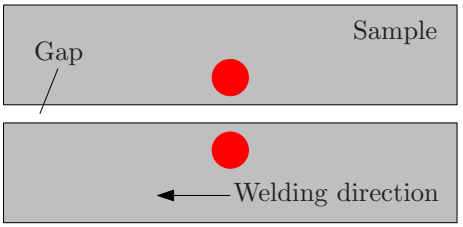

Figure 6.6: *No laser light escapes through the gap in the TS process with a parallel configuration and a large inter-spot distance.*

parallel configuration, where the inter-spot distance is about two to three times the spot diameter, the laser light can be projected on both sides of the seam (Figure 6.6). In this way, no laser light escapes through the gap between the sheets.

If the inter-spot distance is in the order of two to three times the spot diameter, two separate keyholes will be formed. This means that, when the laser power is equally distributed over the laser spots, each spot has only half the irradiance compared to the SS process. During twin spot welding, the processing speed will therefore have to be reduced or the applied laser power will have to be increased to obtain a penetration depth comparable

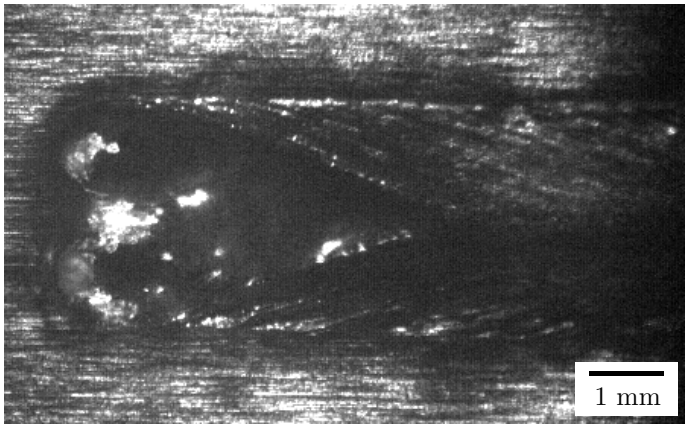

(a) Camera image.

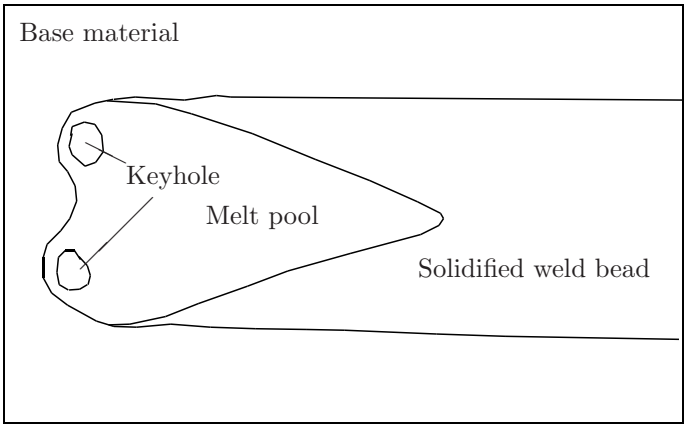

(b) Schematic overview.

Figure 6.7: *In-situ CMOS camera image of a bead-on-plate TS process of AA5182 sheets, using the developed camera-based monitoring system.*

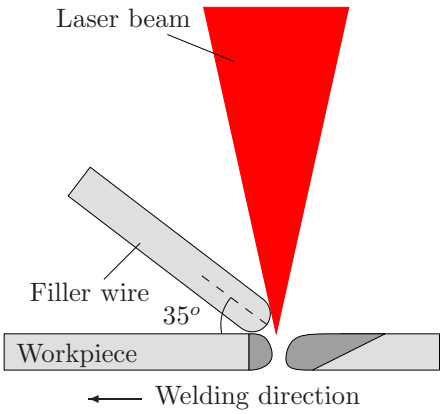

Figure 6.8: *Schematic overview of the SSCW process.*

with the SS process.

Spectral measurements of the TS welding process show that the optical emissions are comparable to those of the SS welding process. This means that the camera-based monitoring system described in Chapter 3, can also be used for this process. Figure 6.7(a) shows an image of a TS welding process made with this monitoring system. In the image, both keyholes can be distinguished. The heart shaped melt pool is also clearly visible and is significantly larger than that for the SS process.

In Section 6.4, the gap bridging capabilities of the TS process will be investigated.

6.2 Laser Welding with Cold Wire Feeding

Because of the small dimensions of the laser spot (0.45 mm in diameter) and melt pool, the laser welding process in a butt weld configuration is in general quite sensitive for gaps between the sheet edges. To compensate for the lack of material due to the air gap, wire feeding can be used [1, 68, 69]. By using a filler wire, one can also compensate for the loss of volatile elements from

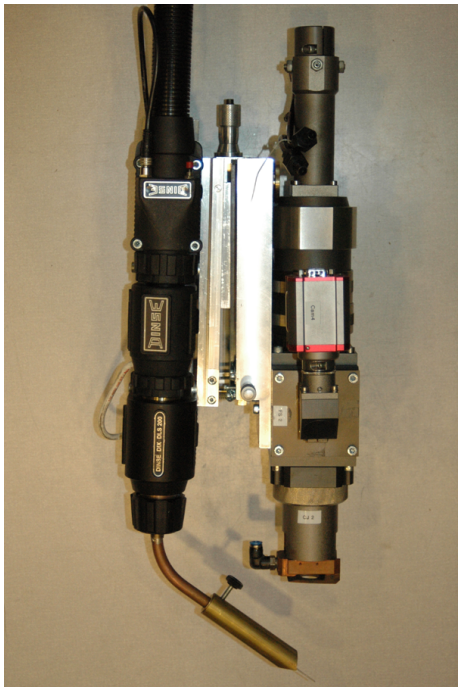

Figure 6.9: *Photo of the SSCW head, consisting of a BEO D70 Trumpf laser welding head, combined with a Dinse DIX WDE 315 wire feeding torch.*

Figure 6.10: *Photo of the Dinse DIX WDE 315 wire feeder.*

the base material during welding. The wire feeding equipment used in this work will be introduced in this section.

The equipment used for the Single Spot laser welding with Cold Wire feeding (SSCW) process is identical to that of the SS process (Page 26), with an additional wire feeder. For the experiments in this work, a Dinse DIX WDE 315 push-push wire feeder is used (Figures 6.9 and 6.10). Figure 6.8 shows a schematic view of the SSCW process setup.

As shown in the overview, the wire feeding torch is usually leading the laser welding head and the wire is supplied from the front side, under an angle of about 20^o to 60^o with respect to the workpiece [68, 69]. The torch of the Dinse wire feeder has an angle of 35^o with the workpiece. For the welding experiments of AA5182 sheets, a standard commercially available 1.2 mm AA5356 (AlMg5) wire was used.

The positioning of the wire with respect to the laser spot is very important [68, 69]. Even a small misalignment of the wire and the laser beam can result in a welding defect.

Spectroscopic measurements of the SSCW process of AA5182 sheets using a AA5356 wire show that the optical emissions are essentially the same as for the SS welding process. This means that the monitoring system described in Chapter 3 is also suited for the SSCW process. In Figure 6.11(a) an typical in-situ camera image of this process is shown. In this image, the wire entry is from the left. Since the 10 W diode laser illuminates the surface from one side, the wire casts a shadow on the sample surface. The image shows that the wire is aligned with the welding direction and is directed exactly to the laser spot.

As with the SS process, the TS process in parallel arrangement can also be combined with wire feeding. For this purpose, the Dinse DIX WDE 315 wire feeder described in Section 6.2 is mounted to the Trumpf BEO D70 twin spot laser welding head. All remarks about the SSCW welding process regarding the accurate alignment of the wire and the laser beam and the requirements for lower welding speeds are also applicable to the Twin Spot laser welding with Cold Wire feeding (TSCW) process. The monitoring system can also be used for observations of the TSCW process (Figure 6.12(a)).

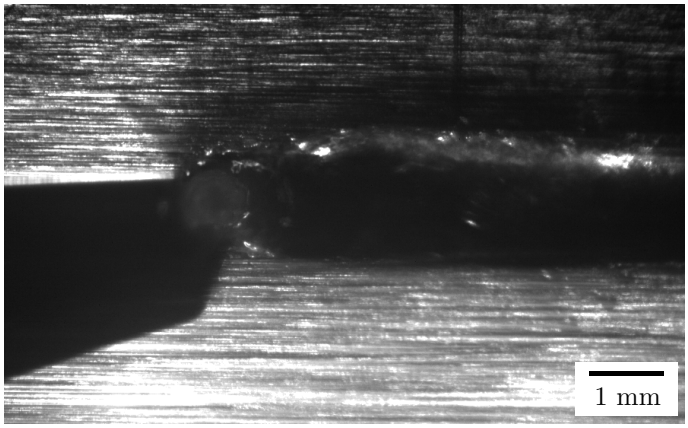

(a) Camera image.

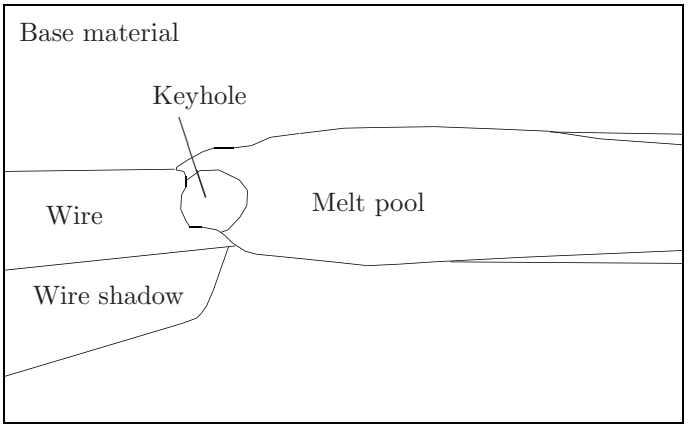

(b) Schematic overview.

Figure 6.11: *In-situ CMOS camera image of a butt weld SSCW process of AA5182 sheets, using the developed camera-based monitoring system.*

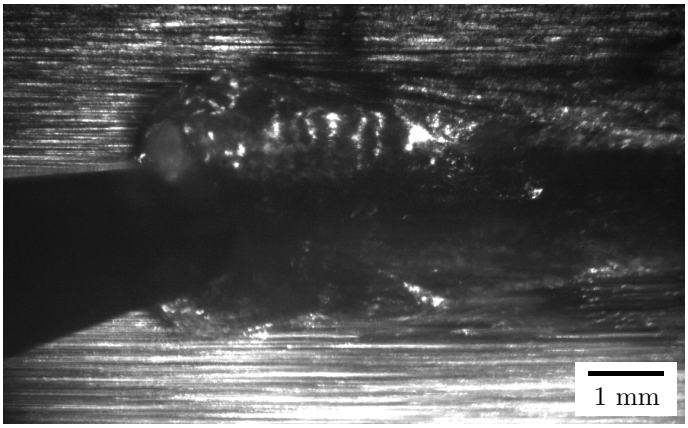

(a) Camera image.

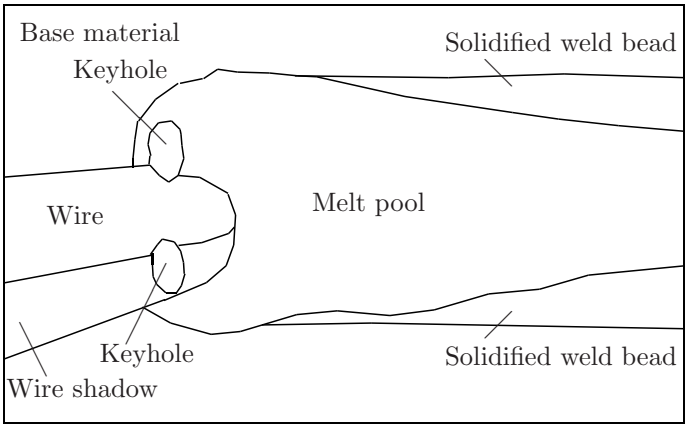

(b) Schematic overview.

Figure 6.12: *In-situ CMOS camera image of a butt weld TSCW process of AA5182 sheets, using the developed camera-based monitoring system.*

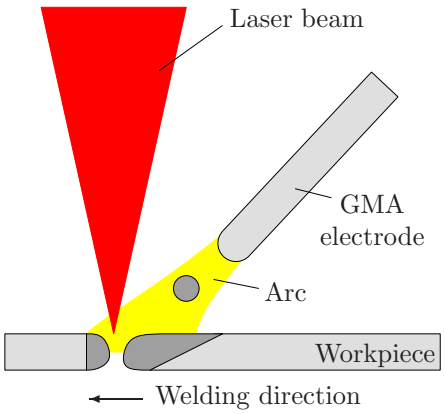

Figure 6.13: *Schematic overview of the HLG process.*

The gap bridging capabilities of the SSCW and the TSCW will be treated in Section 6.4.

6.3 Hybrid Laser/GMA Welding

The combination of the laser welding process with the Gas Metal Arc (GMA) welding process has become popular in the last few years [70, 71, 72]. In this section, the Hybrid Laser/GMA welding (HLG) process and equipment used in this work will be discussed, with a focus on the welding of thin aluminium sheets.

The HLG process as used in this work is the so-called arc assisted laser welding process, where the Nd:YAG laser beam is the primary and the arc is the secondary heat source. As with the SS process, the laser beam is focussed on the sample surface and forms a keyhole (Figure 6.13). The GMA welding process is the secondary heat source, which is trailing the laser beam. By bringing these two heat sources close together, the processes will interact, resulting in a combined melt pool.

The HLG equipment used consists of a standard BEO D70 Trumpf laser

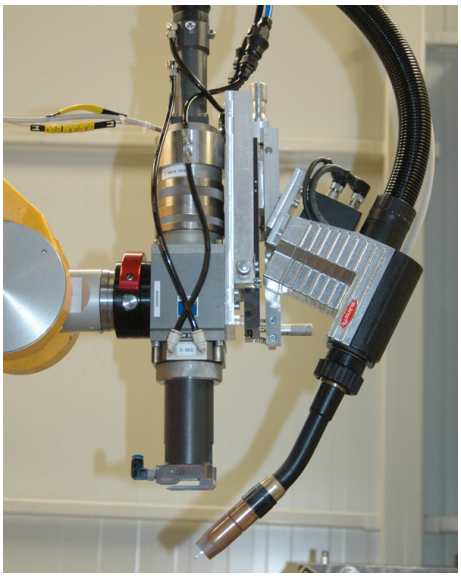

Figure 6.14: *Photo of the HLG head, consisting of a BEO D70 Trumpf laser welding head, combined with a Fronius Robacta Drive CMT torch.*

Figure 6.15: *Photo of the Fronius TPS 3200 CMT current source (Courtesy of Fronius).*

welding head, combined with a Fronius GMA welding system [74] (Figure 6.14). This Fronius GMA welding system consists of a Robacta Drive CMT torch, connected to a VR7000-CMT wire feeder and a TransPulse Synergic 3200 CMT current source (Figure 6.15). The HLG welding head is manipulated using a six axis industrial Stäubli RX130 robot. Argon is used to shield the welding process from the environment. In all experiments a standard AA5356 wire, with a diameter of 1.2 mm, was used.

Research has shown that the HLG process is more tolerant for seam gaps than the SS process. With the HLG process, the relatively wide melt pool and the added material from the wire are able to compensate for possible air gaps [70, 71, 72].

The laser weakly ionises the plume in and above the keyhole, which

locally increases the electrical conductivity. In this way the plume provides a well defined arc root [75]. This facilitates a stable arc even for high welding speeds. The combination of robustness for gaps and high welding speeds makes this process potentially very suited for industrial use.

The higher power densities of the HLG process also have some negative effects. First of all, the thermal deformations of the workpiece are larger than those in the case of the SS process. Especially for thin metal sheets, this can be a problem. Secondly, the HLG melt pool and weld bead are significantly wider, which may result in less deformability of the material in the weld zone. This is an important drawback for the welding of TWB's, which require joints which can withstand large deformations during the forming stage. A wide weld bead may also be undesirable for aesthetic reasons.

To visualise how the weld quality varies as a function of different parameters, so-called process windows can be of aid. These process windows give a quick overview of which parameter combinations result in a good weld quality. Process windows will be treated in more detail in Section 6.4.1.

In Figure 6.16 two process windows are given, where the weld quality is given as a function of the laser power P and the mean GMA power P_g. For 1.1 mm sheets, it is possible to obtain a good weld quality, but the parameter range is very small and the process is very sensitive for external disturbances. For 2.1 mm sheets, the process is more robust and much more parameter settings yield a good weld quality. This indicates that the HLG welding is less suited for sheet thicknesses below 2 mm.

Figure 6.17 shows the spectrum of light that reaches the camera chip during the the HLG process of AA5182 sheets. During the spectral measurements a broad band-pass filter (Thorlabs FES0950 6704, see Appendix B) was used to protect the detector from the high intensity Nd:YAG radiation. The spectrum shows that the emissions are different from the SS process.

With the SS process, the thermal radiation is dominant, which has a broad-band spectrum. For the HLG process besides the thermal radiation, also emission lines are important. These emission lines are caused by the arc of the GMA process and are visible as strong peaks in the spectrum of

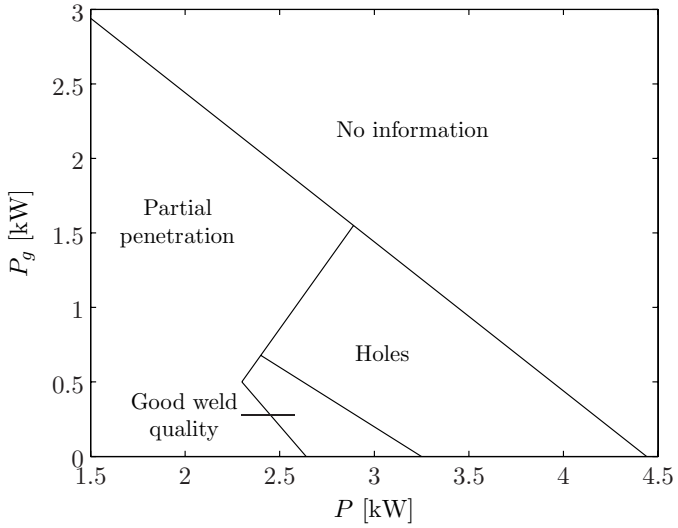

(a) 1.1/1.1 mm thickness

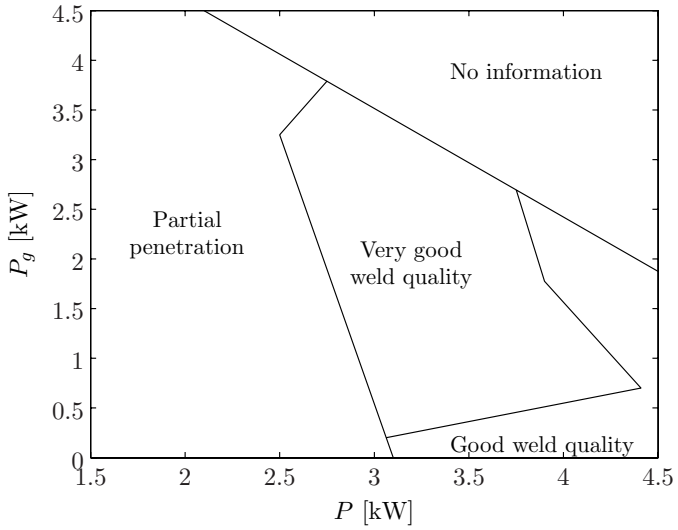

(b) 2.1/2.1 mm thickness

Figure 6.16: *Process windows for butt welds of AA5182 sheets, with the HLG process.*

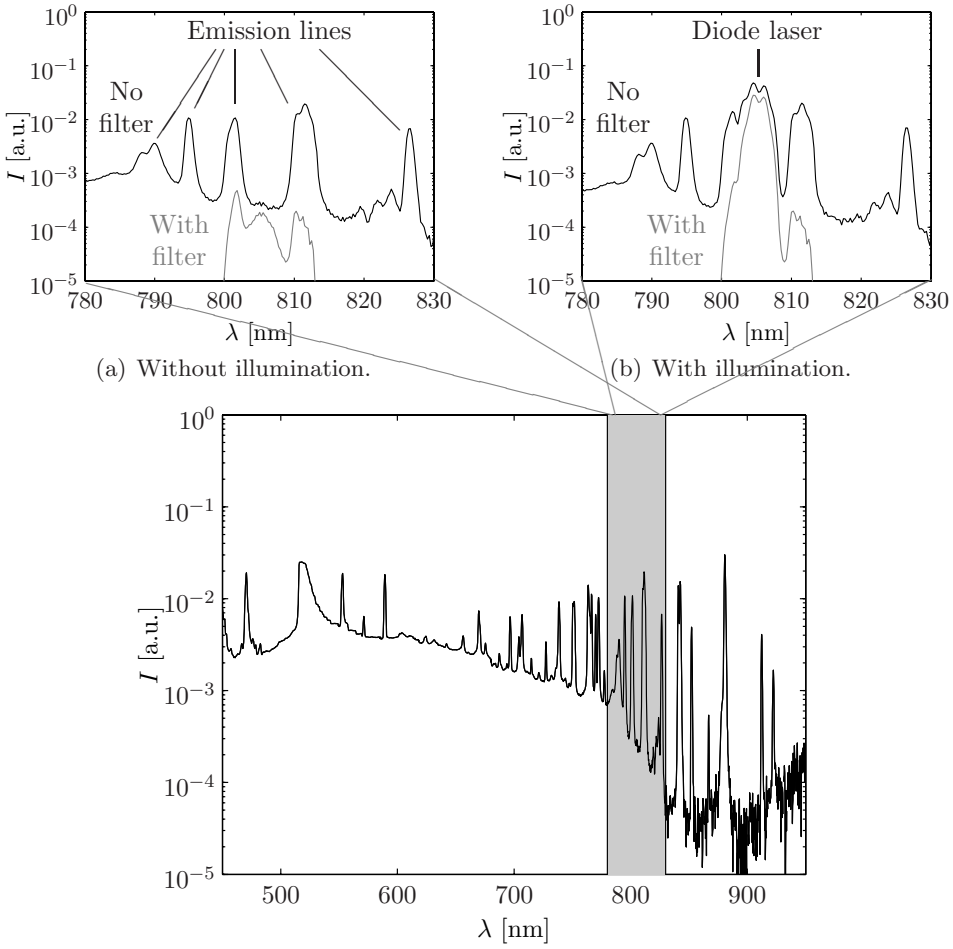

(a) Without illumination.

(b) With illumination.

Figure 6.17: *The spectra at the camera position, both with and without the narrow band-pass filter in the beam path.*

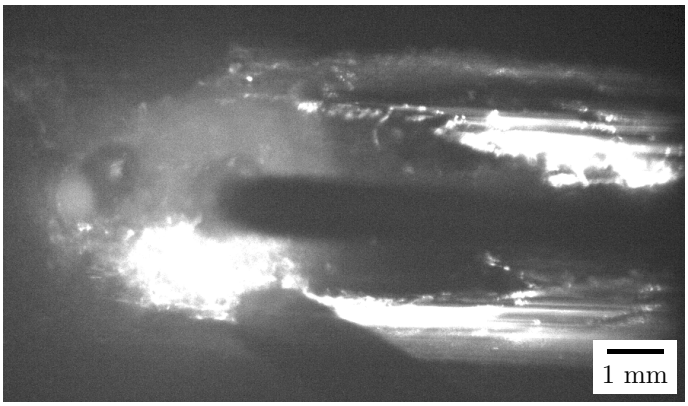

(a) Camera image.

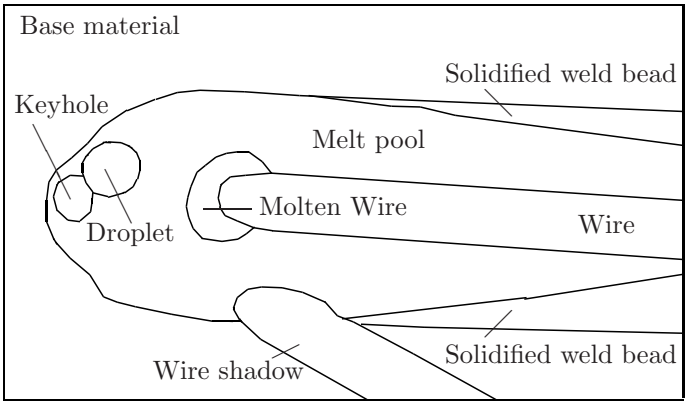

(b) Schematic overview.

Figure 6.18: *In-situ CMOS camera image of a bead-on-plate HLG process of AA5182 sheets, using the developed camera-based monitoring system.*

Element		λ [nm]
Al	Aluminium	806.597
		807.535
Ar	Argon	801.4786
		805.3308
Fe	Iron	804.374
		806.570
Mg	Magnesium	804.773
		804.985
		805.423
Si	Silicon	803.5619
Sn	Tin	803.05
		803.93
Ti	Titanium	802.484
		806.824

Table 6.1: *Overview of elements which can be encountered during most welding applications and which have emission lines between 801 and 809 nm [49].*

Figure 6.17. This means that with the selection of the illumination wavelength for this process, these emission lines need to be taken into account. If one of these emission lines falls within the transmittance band of the narrow band-pass interference filter, it will reach the camera chip without significant suppression. In the camera image, the arc will then appear as a blinding white area, which will hide the melt pool from the camera.

However, in Figures 6.17(a) and 6.17(b) it can be seen that with the 10 W 805 nm diode laser and matching narrow band-pass filter (Thorlabs CDI1553 805-4), none of the emission lines near the transmittance band of the narrow band-pass filter pose any significant problem. The selected equipment is therefore also suited for this welding process, as can be seen in Figure 6.18(a). In this figure a real-time camera image of the HLG

welding process is shown. In this image the GMA wire and a metal droplet are visible, while the arc is present. A small residue of the emission lines near the transmittance band of the narrow band-pass filter can faintly be distinguished around the wire end and the keyhole.

The emission lines in the spectrum are dependent on the chemical elements in the plume and therefore also on the chemical composition of the material and on the shielding gas composition. In Table 6.1 an overview is given of elements which can be encountered during most welding applications and which have emission lines in the wavelength range of 801 to 809 nm (the transmittance band of the narrow band-pass filter) [49]. The fact that an element in the plume has an emission line in the transmittance band of the filter does not automatically mean that the monitoring system adversely be affected. For instance, in the experimental results presented in this work, the emission lines from Al, Ar and Mg listed in Table 6.1 pose no problems. Spectral measurements or camera images recorded during these welding processes can confirm the applicability of the chosen illumination wavelength (805 nm).

6.4 Gap Bridging Capabilities

In this section, the gap bridging capability of five different laser-based welding techniques is compared for 1.1 mm and 2.1 mm AA5182 sheets. The gap bridging capability of the Single Spot laser welding with Cold Wire feeding process (SSCW), the Twin Spot laser welding with Cold Wire feeding process (TSCW) and the Hybrid Laser/GMA welding process (HLG) were compared to that of the Single Spot laser welding process and the Twin Spot laser welding process without filler wire (SS and TS respectively). The resulting weld quality is assessed by means of visual inspection of the weld bead, microscopic inspection of cross sections, micro-hardness measurements, tensile test measurements and Erichsen cupping test measurements.

To investigate the gap bridging capabilities of the different welding processes, two butt weld configurations will be tested. In the first configuration

	SS		TS		SSCW	
b [mm]	1.1	2.1	1.1	2.1	1.1	2.1
P [kW]	4.0	4.0	4.0	4.0	4.0	4.0
d_s [mm]	0.45	0.45	0.45	0.45	0.45	0.45
v [mm/s]	160	100	140	60	160	80
v_w[1] [mm/s]	-	-	-	-	100-165	100-215
P_g [kW]	-	-	-	-	-	-
q_i [J/mm]	25	40	29	67	25	50

	TSCW		HLG	
b [mm]	1.1	2.1	1.1	2.1
P [kW]	3.5	4.0	2.5	3.5
d_s [mm]	0.45	0.45	0.60	0.60
v [mm/s]	100	60	120	100
v_w[1] [mm/s]	110-190	45-170	40	115
P_g [kW]	-	-	0.5	2.0
q_i [J/mm]	35	67	25	55

Table 6.2: *The welding parameters used during the gap bridging experiments for the different welding processes on AA5182 sheets.*

[1]For cold wire feeding, the optimal wire speed depends on the gap width.

two 1.1 mm sheets and in the second configuration two 2.1 mm sheets are joined. The welds are always parallel to the rolling direction of the sheets.

Both configurations have a constant pre-set gap between the sheets. For every configuration, optimised values for the laser power, welding speed, and arc power are used, which were determined from earlier experiments. In Table 6.2 an overview of the optimal welding parameters for the different processes is given. Here d_s is the focal diameter of the laser spot, v_w is the feeding wire speed, P_g is the average power of the GMA arc and q_i is the total heat input during welding, which is calculated as

$$q_i = \frac{P + P_g}{v}. \tag{6.1}$$

To obtain a satisfactory weld quality, the wire speed v_w needs to be adjusted for each value of the pre-set gap. This indicates that for realistic welding situations, where the seam gap is usually not known in advance, an on-line seam gap measurement system can be beneficial. Based on these seam measurements, v_w can be adjusted online. Such systems have been a subject of study in the past [76].

During the SS, TS, SSCW and TSCW experiments, Ar shielding gas is used with a top flow of 1360 l/h and a back flow of 340 l/h. During the HLG experiments the weld was shielded using a Ar top flow of 900 l/h and a Ar back flow of 480 l/h. The focal position is placed on the top surface of the sheets.

6.4.1 Visual Inspection of the Weld Bead

When large quantities of welds have to be evaluated, a first qualification by visual inspection is helpful. Different weld quality aspects can be assessed. For instance, in the case of aluminium TWB's, weld penetration, the presence of blow holes, the weld bead surface roughness and the amount of spatter are quite important. Not every aspect of the weld quality is equally important. For instance, for TWB's the penetration of the weld is much more important than the amount of weld spatter.

Figure 6.19 shows a process window which gives an indication of the visually observed weld quality for different values of the laser power P and the welding speed v, for butt welds of 1.1/1.1 mm and 2.1/2.1 mm AA5182 sheets respectively. The lines in Figure 6.19 indicate the approximate boundaries in the process windows of the regimes with a comparable weld quality. The gray area indicates the region with the best trade-off between process speed, laser power and weld quality.

Although this visual inspection of the weld quality is not entirely objective, in general it provides for a good qualitative overview of the influence of the parameters on the weld quality. In Figure 6.19, process windows for

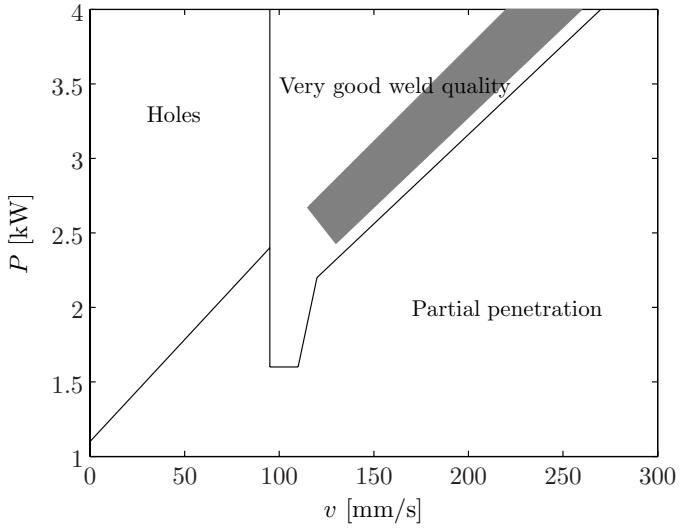

(a) 1.1/1.1 mm thick sheets

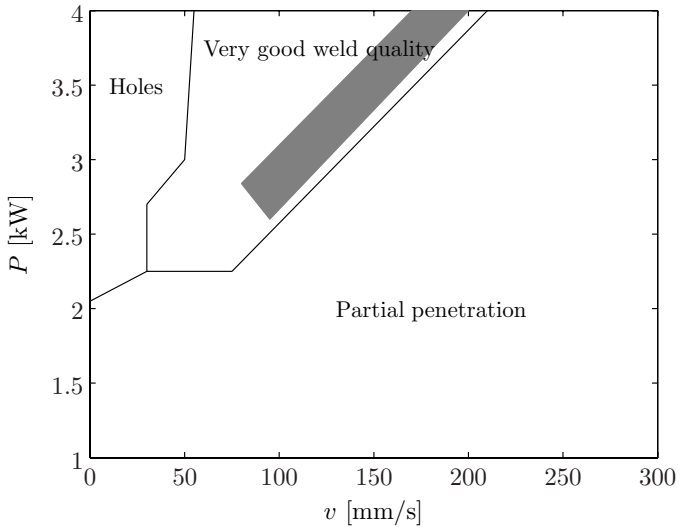

(b) 2.1/2.1 mm thick sheets

Figure 6.19: *Process windows for the laser welding process of butt welds of AA5182 sheets. The gray area indicates the recommended settings.*

different values of P and v are given. It is also possible to present a process window with other parameters on the axes, as was already demonstrated in Section 6.3. The most suitable parameters for the two axes of the process window will differ per situation.

Figure 6.20 shows typical appearances of weld beads for each of the five welding processes. The pre-set gap width s for each specific weld is indicated in the figure. It can clearly be seen that the weld beads resulting from the SS and SSCW welding processes are narrower than those of the TSCW welding process. For the twin spot processes, the parallel placement of the laser spots results in a wider melt pool (Figures 6.7 and 6.12).

The weld bead of the TS process is wider than that of the TSCW process. This is caused by the fact that in the TS process, the sheets absorb most of the laser power, whereas in the TSCW process, a large part of the energy is used to melt the wire. Therefore less laser power is available to melt the sheets, which results in a narrower weld bead.

A comparison of the bead of the HLG process with those resulting from the other processes shows that the former also has a wider melt zone. With the HLG process the interaction zone of the arc with the workpiece is much larger than the interaction zone of the laser, causing a wider melt pool at the top surface.

In Figure 6.20(e), the top bead resulting from the HLG welding process is shown. In this figure, a black deposit is visible next to the weld bead. The other welding processes do not show this, but do show a gray deposit covering the bottom surface of the weld. These deposits mostly contain aluminium oxide and magnesium oxide, with some traces of metallic aluminium and magnesium [77], and is formed by evaporation of aluminium and magnesium elements from the welding process. Since the temperatures in the arc of the HLG welding process are higher than those in the plume and keyhole of the laser welding process, the evaporation will be stronger. Near the interaction zone of the laser and arc with the material, the shielding gas prevents oxidation of these metallic elements. Further away, the aluminium and magnesium will oxidise and condens on the colder base material. Normally, these oxides are white. However, in this case the particle size is so small, that the deposit entraps light, which gives it it's dark

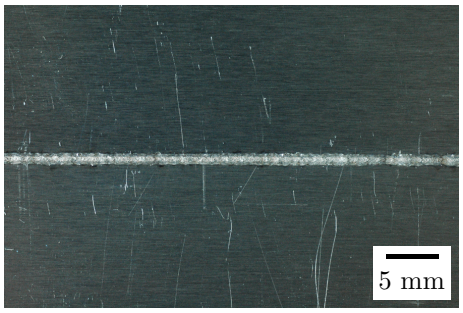

(a) SS process, $b = 1.1$ mm, $s = 0.2$ mm.

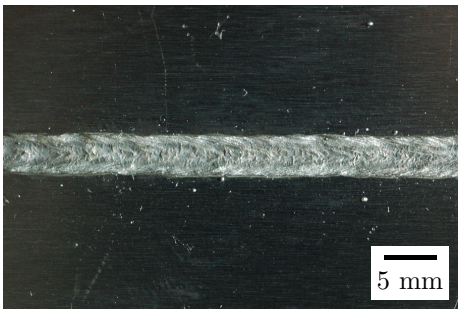

(b) TS process, $b = 2.1$ mm, $s = 0.2$ mm.

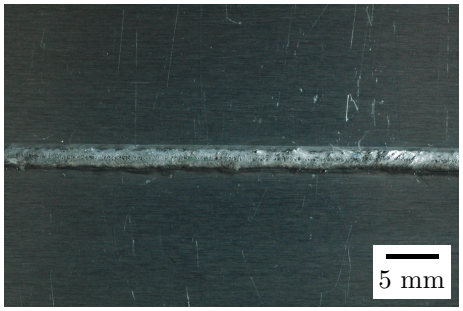

(c) SSCW process, $b = 1.1$ mm, $s = 0.0$ mm.

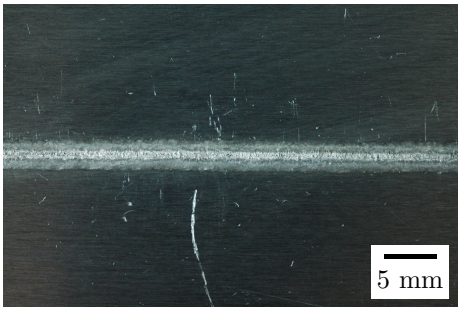

(d) TSCW process, $b = 1.1$ mm, $s = 1.0$ mm.

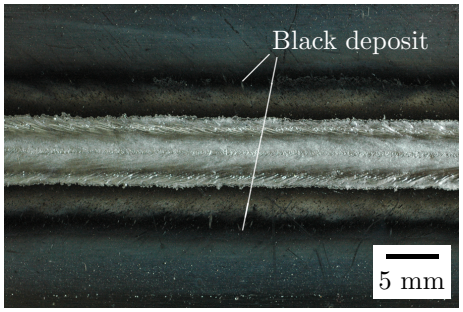

(e) HLG process, $b = 2.1$ mm, $s = 1.0$ mm.

Figure 6.20: *Typical weld beads for the different laser-based welding processes. For each weld, the pre-set gap width s and the material thickness b are indicated.*

	SS	TS	SSCW	TSCW	HLG
1.1/1.1 mm	0.2 mm	0 mm	0.4 mm	0.6 mm	-
2.1/2.1 mm	0.2 mm	-	0.6 mm	0.6 mm	1.0 mm

Table 6.3: *The gap bridging capabilities of the different processes based on a visual inspection of the weld.*

appearance. The gray deposit on the bottom surface of the laser welds indicates that the gas shielding on the bottom can be improved. The deposits have no direct effect on the weld strength and performance [77, 78].

Visual inspection of the weld samples also gives a first indication of the gap bridging capabilities of the different processes, since welding defects, like holes or excessive undercut, can easily be detected (Figure 6.21).

In Table 6.3, the maximum allowable gaps for each of the different welding process are given. These values have been determined from visual inspections of welds with different pre-set gap sizes, ranging from 0 to 1.2 mm. In this evaluation, the weld is regarded acceptable if no or only a few minor welding defects are present. The samples were welded over a length of 220 mm, without using a tag weld. Since start and stop effects of the welding processes fall out of the scope of this research, the first and last 20 mm of the welds are not included in the evaluation.

The SS welding experiments show a dramatic decrease in weld quality when the gap is over 0.2 mm. An important cause for welding defects in this case is the lack of gap filling by molten metal. Since the SS melt pool is small (about 1.5 mm wide), compared to other welding processes, there is only a limited amount of liquid metal available to fill the gap. This results in deep undercuts and holes.

It is difficult for the SS process to initiate a stable welding process. Since the laser spot is symmetrically aligned with the seam, at the start of the weld a large part of the laser radiation escapes through the gap between the sheets, as illustrated in Figure 6.5 on page 112. Only after some time, enough liquid metal is formed to fill the gap in front of the laser beam, preventing this escape of laser radiation.

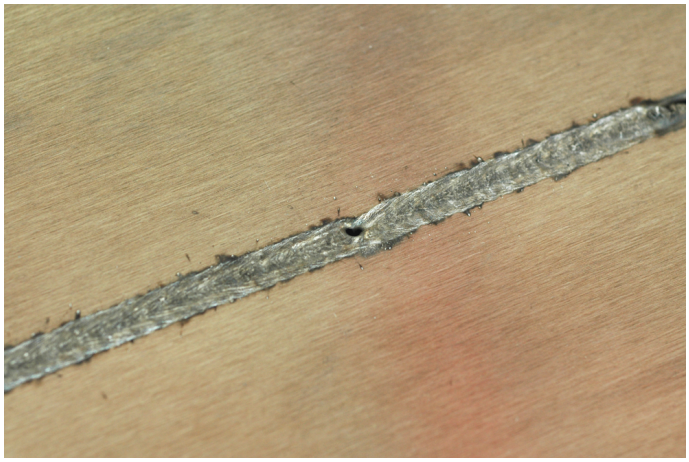

(a) A hole.

(b) Undercut.

Figure 6.21: *Photos of two possible welding defects that can be distinguished with visual inspection of the weld bead.*

With the TS welding experiments, the 1.5 mm distance between the spots ensures that all laser light is projected on the base material and that the startup of the welding process is less problematic. Although the melt pool of the TS process is wider, this process shows an unacceptable weld quality due to undercut and holes for even the smallest gap. A gap will decrease the amount of molten metal between the two keyholes, which will join into a single large keyhole. Such a large keyhole will start to elongate due to the surface tension pressure, as explained in the previous chapter. This elongated keyhole shape is not stable and will result in holes in the weld bead. This demonstrates that the TS process with a parallel configuration is not suited for laser welding of AA5182 sheets and that the use of filler wire is essential to bridge gaps. For the TSCW process, the wire assures that the two keyholes do not join, which results in a stable welding process.

By applying wire feeding, the gap tolerance of the welding process increases significantly. The SSCW welding is especially suited if a high processing speed is required and the maximum gap size is not larger than 0.4 mm in the case of 1.1 mm sheets and 0.6 mm in the case of 2.1 mm sheets. For larger gaps, not enough base material is molten to form a good joint, especially at the weld root. For the TSCW welding process the gap bridging capability is 0.6 mm for both 1.1 mm and 2.1 mm sheets, at the cost of welding speed. Experiments show that for both the SSCW and the TSCW processes it is occasionally possible to bridge gaps up to 1.0 mm, but these results can not be reliably reproduced.

Although the SSCW and TSCW are significantly more tolerant for gaps, both processes are quite sensitive for wire misalignments. The sensitivity of these processes for alignment deviations of the wire with respect to the laser spot increases with an increasing gap width. For gaps over 0.6 mm, the required positioning accuracy of the wire is very high. In this case, even the smallest variation in wire position will cause a welding defect. This problem could be overcome by actively actuating the wire laterally [76].

Experiments with the HLG welding process for 1.1 mm sheets show that it is possible to achieve a good weld quality. However, the parameter range is very small (Figure 6.16). The resulting weld quality for these sheet thicknesses, even without a gap, is lower than that of the other processes.

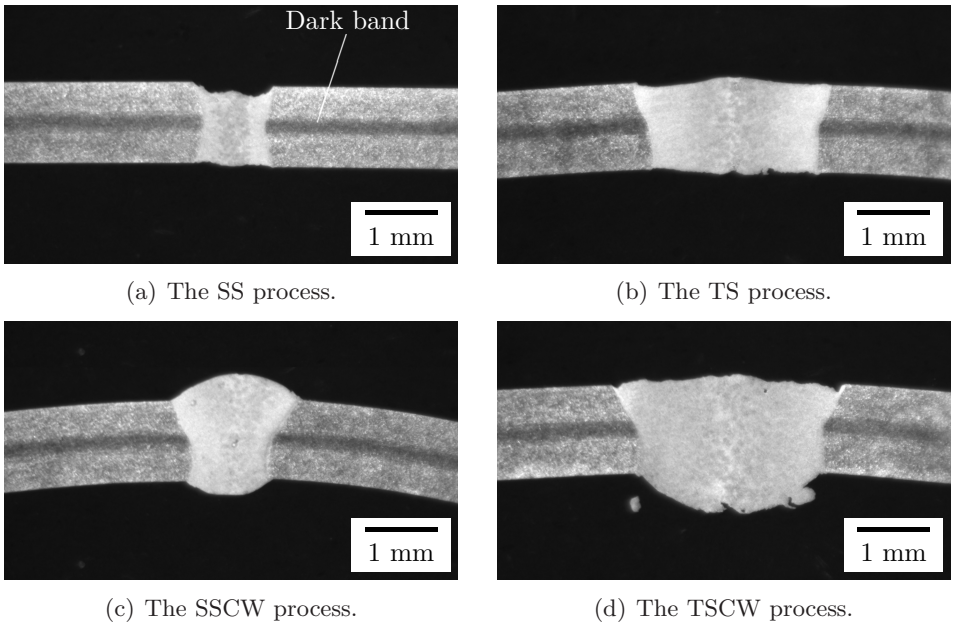

(a) The SS process. (b) The TS process.

(c) The SSCW process. (d) The TSCW process.

Figure 6.22: *Photos of cross sections of the welds of the different processes for 1.1 mm thick AA5182 sheets.*

For 2.1 mm sheets the HLG welding process gives a much better weld quality. Gaps up to 1.0 mm could be bridged without problems.

6.4.2 Microscopic Inspection of Cross Sections

The weld bead geometry, porosity content and the micro-structure in and around the weld, can be evaluated by visual inspection of cross sections of a welded sample. Small parts of a sample are cut, embedded in bakelite, ground and polished. To reveal the Melt Zone (MZ) and Heat Affected Zone (HAZ), the sample is etched using a Keller-Wilcox agent. In the cross section shown in Figure 6.23(a) the base material, HAZ and MZ are indicated.

In Figures 6.22 and 6.23, cross sections of welds resulting from the

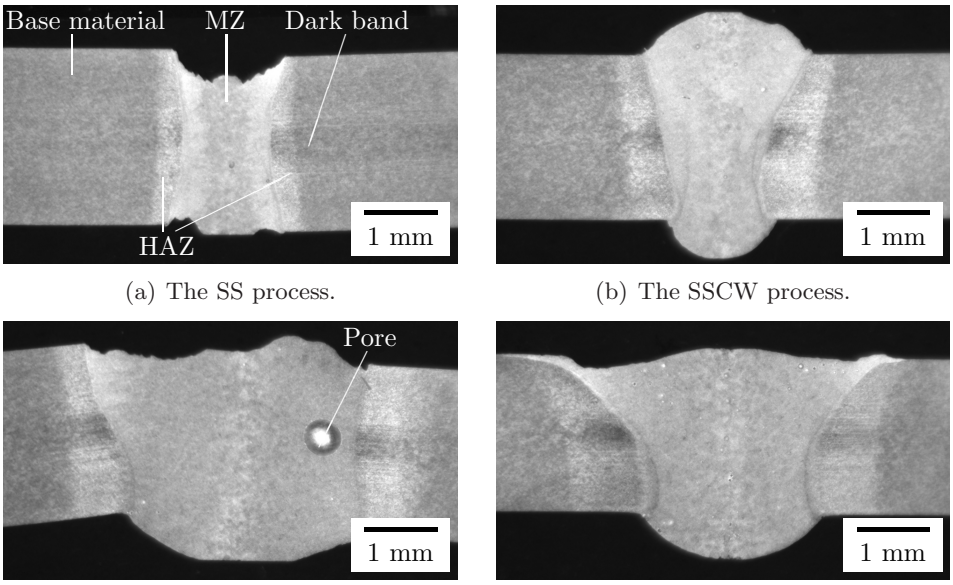

(a) The SS process.

(b) The SSCW process.

(c) The TSCW process.

(d) The HLG process.

Figure 6.23: *Photos of cross sections of the welds of the different processes for 2.1 mm thick AA5182 sheets.*

different welding processes are shown for 1.1 mm and 2.1 mm AA5182 sheets, respectively. Some of the samples are slightly bent due to thermal deformations of the sheets during welding or embedding process. In these figures a dark band at the centre of the sheets is visible. This band is caused by a difference in microstructure at and near the surfaces and at the sheet centre. Such differences are mainly due to an inhomogeneous plastic deformation of the material during the cold rolling process [79, 80]. Segregation in castings could also contribute to this. The effect is more pronounced with 1.1 mm thick sheets.

For all welds, the base material and the Melt Zone (MZ) can be clearly distinguished. During the welding of the 2.1 mm sheets the heat input q_i is much higher than that for the 1.1 mm sheets, resulting in a larger Heat

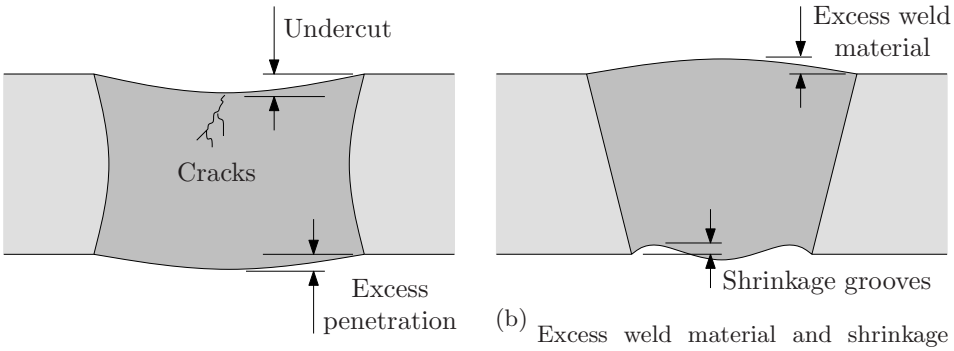

(a) Cracks and undercut.

(b) Excess weld material and shrinkage grooves.

Figure 6.24: *Schematic overview of the selected geometrical criteria from ISO norm 13919-2.*

Affected Zone (HAZ). For the 2.1 mm sheets the HAZ is visible in the cross sections. For the welds in 1.1 mm sheets, there hardly is any HAZ present.

Figures 6.22(a) and 6.23(a) show that the melt zone of the SS process has the same width at the top and bottom surface, as was already observed in Section 5.3 (page 100). For the TS, SSCW and TSCW processes, the MZ is a little bit wider at the top than at the bottom. For the HLG process, the MZ is much wider at the top than at the bottom. This is mainly due to the fact that in the GMA process, the heat input is much greater at the surface region and the keyhole formation is entirely due to the laser process alone.

The amount of undercut and overfill can be compared with relevant criteria from the ISO 13919-2 norm [81]. A weld can be qualified as quality level B (stringent), C (intermediate) or D (moderate). Since the norm states weld imperfections for all sorts of weld configurations, only a number of criteria are useful in the context of butt welds. In this work, the following criteria from ISO norm 13919-2 are selected: (1) Cracks, (11) Undercut, (12) Excess weld material, (13) Excess penetration and (18) Shrinkage grooves, which are schematically shown in Figure 6.24. The cross sections also show some pores. Most of these pores are very small (micro pores) and are

	b	s					
	[mm]	0 mm	0.2 mm	0.4 mm	0.6 mm	0.8 mm	1.0 mm
SS	1.1	D	x				
TS		B					
SSCW		B	C	C			
TSCW		D	C	D	D		
SS	2.1	x	D				
SSCW		B	C	x	-		
TSCW		B	C	D	D		
HLG		C	C	-	D	D	D

Table 6.4: *The overall quality levels (B: high quality, C: intermediate quality, D: moderate quality, x: not passed, -: no data available) of the welds with different gaps s, according to the ISO 13919-2 norm, determined from the cross sections.*

caused by hydrogen formation during solidification [9]. Occasionally also macro pores are seen (Figure 6.23(c)), which are formed by instabilities of the keyhole wall. In general, the HLG welds show more porosity than welds from the other processes. Although criteria for porosity are stated in ISO norm 13919-2, these are not used here, since this requires several cross sections per weld to be examined, for a good statistical overview. Also if a weld contains too much porosity, the effects will be seen in the tensile and Erichsen cupping test results.

Evaluation of the cross sections shows that none of these welds suffer from cracks. The welds do occasionally show undercut, excess weld material, excess penetration and shrinkage grooves. In Table 6.4 the resulting quality levels of the welds are given. The overall quality level is determined by considering the lowest quality level of the different criteria. Therefore if a weld has quality level C based on the shrinkage grooves, but has a quality level D based on the excess weld material, the assigned overall quality level is D.

Table 6.4 shows that the SS process results in a moderate weld quality at best. In all cases, the undercut, which is due to evaporation and weld

spatter, is too large to meet the requirements for the higher quality levels. Due to the larger volume of melt pool of the TS welding process, the evaporation and weld spatter will lead to lesser undercut. For the 1.1 mm sheets, the TS process can therefore meet the requirements for quality level B. However, as was already pointed out, this process has no tolerance for seam gaps and is not suited for welding of the 2.1 mm sheets.

For gaps under 0.2 mm, the SSCW process can also deliver weld quality of level B. For larger gaps, the quality level is C or lower, based on the criteria of excess weld material and shrinkage grooves. Table 6.4 shows that for a sheet thickness of 2.1 mm and $s = 0.6$ mm, no data is available. Inspection of the cross section indicates a quality level B, but visual inspection of the weld bead shows that the weld quality varies strongly over the weld length and that the actual weld quality is lower. This is also the case for the examined cross section of the weld of the HLG process with $b = 2.1$ mm and $s = 0.4$ mm.

Quality level B welds can be produced with the TSCW process for 2.1 mm sheets if there is no gap present. For gaps between 0.2 and 0.4 mm, the quality level drops to level C. Even larger gaps result in level D welds based on the amount of undercut and excess penetration. For 1.1 mm sheets, the restrictions on undercut and excess penetration posed by the ISO norm can be considered as too stringent.

For the HLG process, the requirements on the undercut and the excess penetration are the bottlenecks. For gaps below 0.4 mm excess penetration limits the overall quality level. For higher gap widths, the quality level is limited by the undercut. For the 2.1 mm sheets, quality level C is the highest obtainable weld quality.

In general, quality level B can only be obtained using the TS or SSCW (1.1 mm sheets) and SSCW or TSCW (2.1 mm sheets) processes, all with zero gap. In all cases the presence of a gap deteriorates the quality level of the weld as defined by the ISO norm.

6.4.3 Micro Hardness Measurements

Microhardness measurements are often used to determine the weld quality, because these measurements give a good insight on the hardness distribution across the weld bead. Other mechanical properties can be estimated from the hardness data [8, 79]. The hardness is a measure of a material's resistance to localised plastic deformations. In the MZ and HAZ, the mechanical properties of the material can be very different from the base material. Especially for cold worked aluminium alloys like AA5182-O/H111, the material properties are strongly influenced by the heating and cooling during the welding process. This effect can be quantified by measuring the hardness of a cross sectioned sample along the centreline of the sheet. A high hardness value corresponds to a high localised strength [9].

Within this project the hardness in and around the MZ and HAZ is evaluated using Vickers Hardness tests. The measured value is indicated with H_V. The measurements are performed according to the ASTM E 384 - $99^{\epsilon 1}$ norm [82]. One should take caution when comparing measurements from different sources, since the employed sample preparation, testing and analysis methods can have significant influences on the results.

Figures 6.25 and 6.26 show hardness measurements of the cross sectioned samples, which were discussed in Section 6.4.2. They show the hardness profile of the base material, HAZ and MZ, measured approximately along the centreline of the sheets in steps of 0.3 mm. In all measurements a 100 g load was used.

The hardness of the base material is not entirely homogeneous. Near top and bottom surfaces of the sheet, the hardness is 80±2 HV. However in the centre of the sheet, in the dark band (e.g. Figure 6.22), the hardness is lower (74±2 HV). The higher hardness levels at and near the surfaces are due to work hardening caused by the larger deformations during the cold rolling process. The 1.1 mm SSCW sample was deformed and bent during the metallographic preparation. This may be the cause of the higher hardness levels (higher than 85 HV) observed for the base material on both sides of this weld.

In the centre of the MZ, often a drop in hardness is visible. Especially

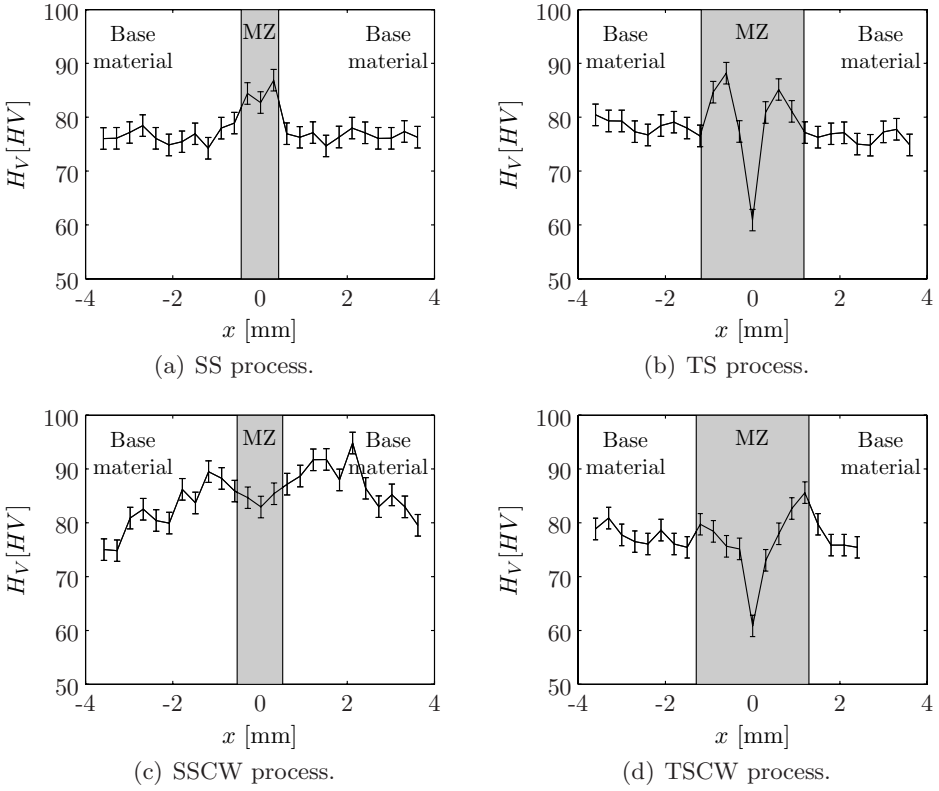

(a) SS process. (b) TS process.

(c) SSCW process. (d) TSCW process.

Figure 6.25: *The microhardness measurement values for the welds of the different processes for 1.1 mm thick AA5182 sheets. The measurement error is indicated with the error bars.*

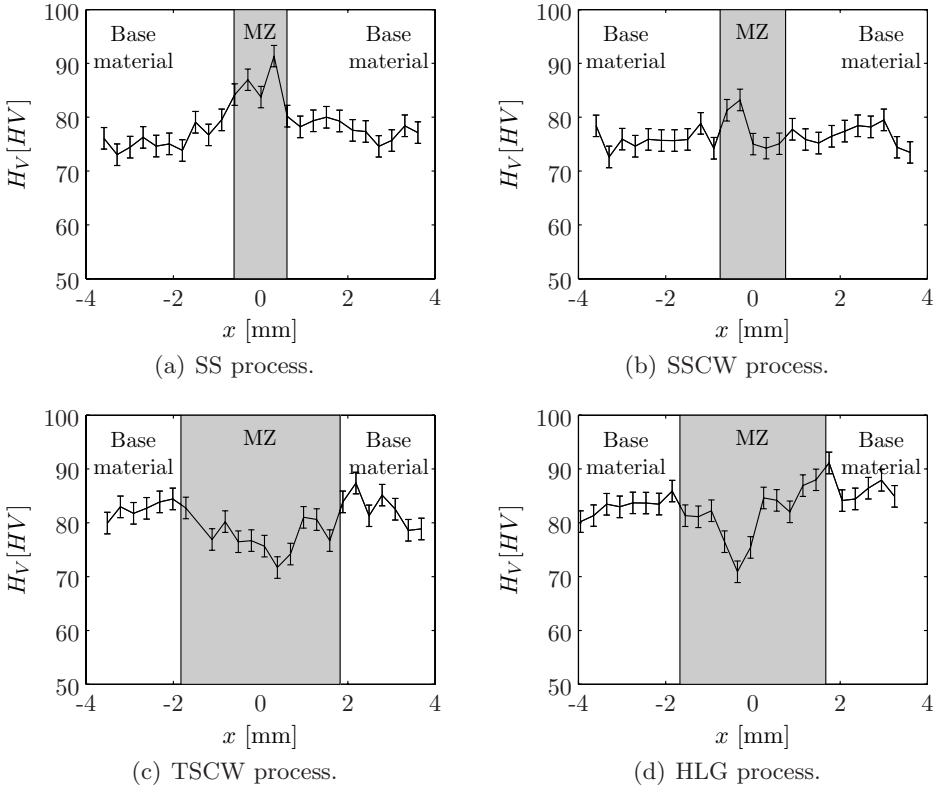

(a) SS process. (b) SSCW process.

(c) TSCW process. (d) HLG process.

Figure 6.26: *The microhardness measurement values for the welds of the different processes for 2.1 mm thick AA5182 sheets. The measurement error is indicated with the error bars.*

l_1: 100 mm r_1: 6 mm
l_2: 32 mm w_1: 10 mm
l_3: 30 mm w_2: 6.0 ± 0.1 mm

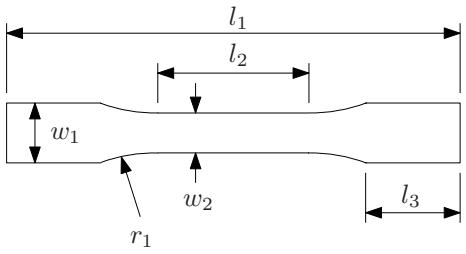

Figure 6.27: *Dimensions of a tensile test sample according to the ASTM E 8M - 98 norm [83].*

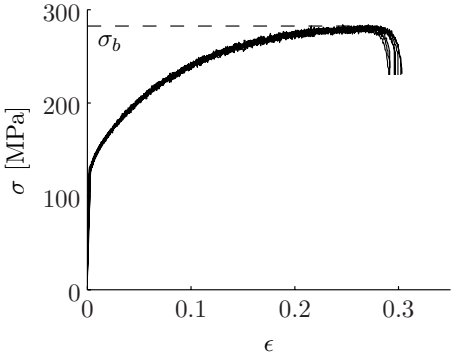

Figure 6.28: *Eight measurements of the engineering stress-strain curve of the 1.1 mm AA5182 base material. The ultimate tensile strength is indicated by σ_b.*

for the TS and TSCW processes (1.1 mm sheets) and the HLG process (2.1 mm sheets) this drop is very pronounced. A comparison of the profiles of the processes with and without filler wire shows that the use of filler wire decreases the hardness in the HAZ and MZ edges slightly. The general, the use of filler wire reduces the hardness peak near the fusion line and in the heat affected zone.

6.4.4 Tensile Tests

After TWB's are welded, the blanks have to be formed using a mold. During forming, the welds are subjected to high loads. The tensile strength is a measure of the maximum load a welded sheet can withstand. The ultimate tensile strength (σ_b) is determined according to the ASTM E 8M - 98 norm [83]. The sample dimensions are given in Figure 6.27. All tensile tests were performed transverse to the welding direction.

Figure 6.28 shows some typical engineering stress-strain curves from tensile test measurements of the AA5182-O/H111 base material, tested

transverse to the rolling direction. The σ_b of the base material is determined from these curves, which is 275 MPa in the case of 1.1 mm AA5182 sheets and 284 MPa in the case of 2.1 mm AA5182 sheets. The tensile strength of a weld sample is often given as a fraction of the tensile strength of the base material. This relative tensile strength is indicated with $\sigma_{b\%}$. Note that the σ_b of the sheets can be different in the rolling direction as compared to that in transverse direction.

The tensile test results of the welds from the different welding processes are shown in Figures 6.29 and 6.30. From each weld, three tensile tests have been performed. The scatter in tensile strength values is indicated with error bars.

The figures show that the tensile strength varies as function of s only for the SS and HLG processes. For the SS and TS processes, a higher value of s results in more undercut. This reduced area of the MZ leads to local stress concentrations, which reduces the load that the weld can carry. Therefore, for these processes all tensile test specimens fail in the MZ, where the local stress concentration is maximum. The HLG test specimens fail in the HAZ or near the edge of the MZ. In Section 6.4.2 it was already pointed out that an increased gap width results in an increased undercut. Similar to the SS and TS processes, this will lead to stress concentrations in the MZ. In Figure 6.23(d) (page 136), a cross section of a HLG weld shows that the maximum amount of undercut is found near the fusion line (boundary between MZ and HAZ).

The SSCW welds of the 1.1 mm sheets have excess weld material and excess penetration, which increases the load bearing surface during the tensile tests (Section 6.4.2). These samples fail just outside the MZ. For the 2.1 mm sheets, the samples fail in the MZ, near the fusion line. Welds of the 1.1 mm sheets, performed with the TSCW process, fail in the base material. The tensile strength values are equal to that of the base material. The excess weld material and penetration increase the load bearing surface of the MZ, which decreases the local stress. It is currently not clear why the 1.1 mm TSCW welds fail in the base material. The tensile test specimens for the 2.1 mm TSCW welds show a similar behaviour as the SSCW samples and fail in the MZ, near the fusion line.

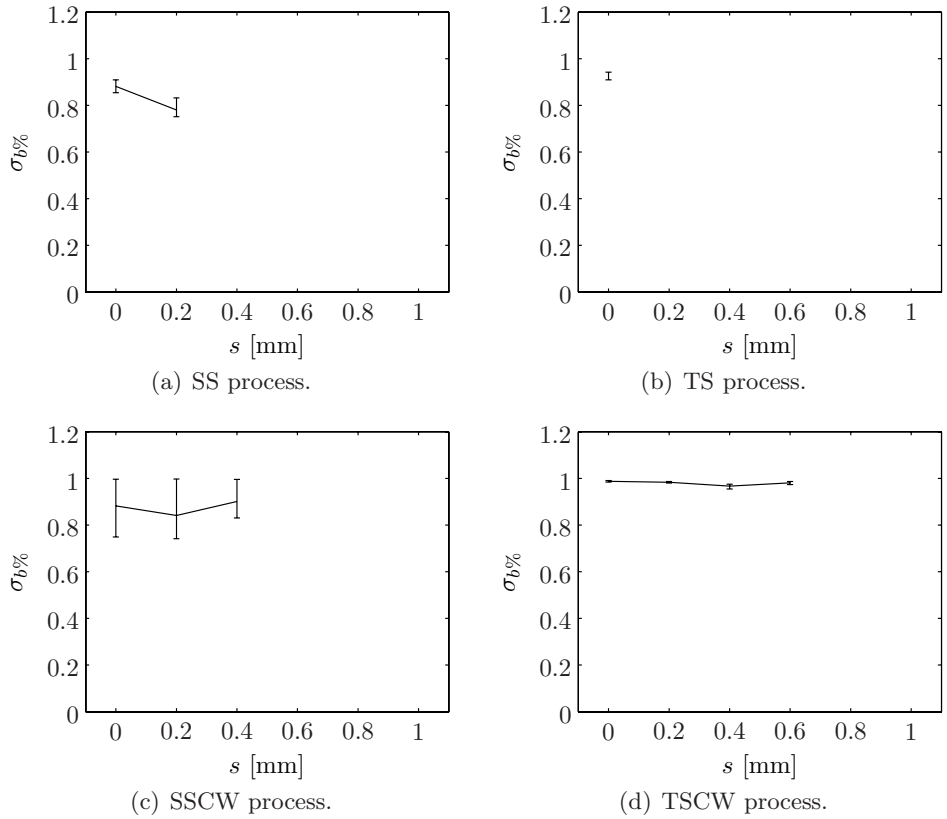

(a) SS process. (b) TS process.

(c) SSCW process. (d) TSCW process.

Figure 6.29: *The tensile test values for the welds of the different processes for 1.1 mm thick AA5182 sheets. The variations found in $\sigma_{b\%}$ found for the different gap values s are indicated with the error bars. The base material σ_b value is 275 MPa.*

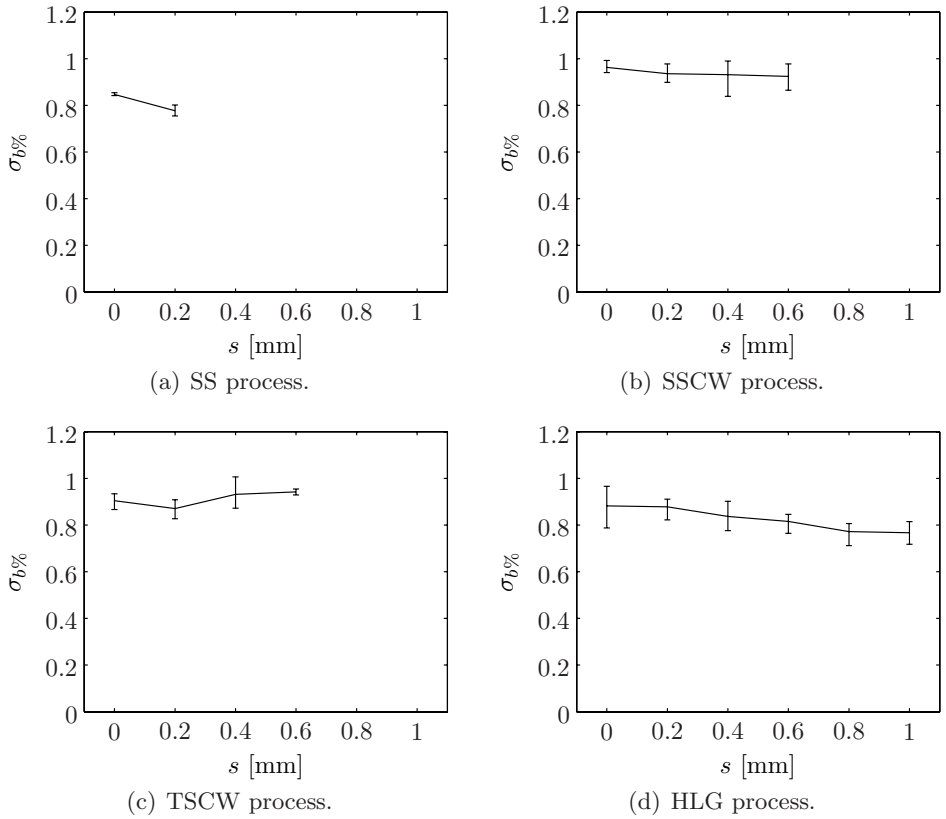

(a) SS process. (b) SSCW process.

(c) TSCW process. (d) HLG process.

Figure 6.30: *The tensile test values for the welds of the different processes for 2.1 mm thick AA5182 sheets. The variations found in $\sigma_{b\%}$ found for the different gap values s are indicated with the error bars. The base material σ_b value is 284 MPa.*

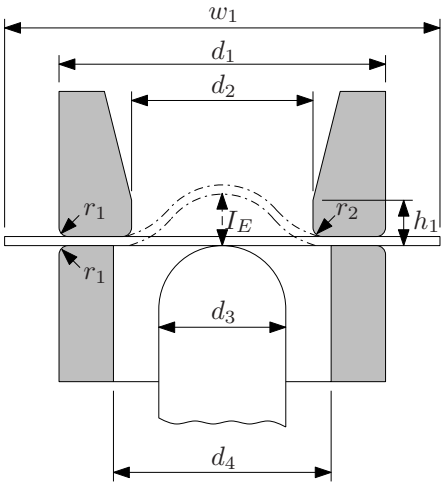

Figure 6.31: *Dimensions of the Erichsen Cupping test apparatus according to ISO norm 20482 [84].*

w_1: ≥ 90 mm
$\varnothing d_1$: 55.0 ± 0.1 mm
$\varnothing d_2$: 27.0 ± 0.05 mm
$\varnothing d_3$: 20.0 ± 0.05 mm
$\varnothing d_4$: 33.0 ± 0.1 mm
r_1: 0.75 ± 0.1 mm
r_2: 0.75 ± 0.05 mm
h_1: 3.0 ± 0.1 mm

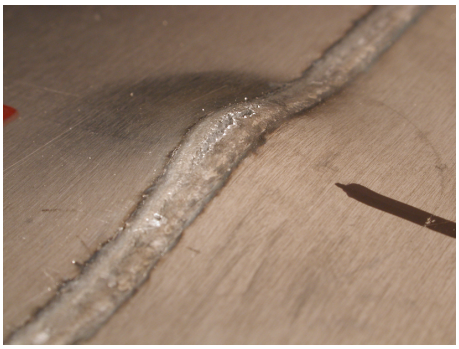

Figure 6.32: *Photograph of a AA5182-O/H111 weld sample after the Erichsen Cupping test. The black line on the right side is a shadow of the Erichsen Cupping test apparatus.*

6.4.5 Erichsen Cupping Tests

Another mechanical testing method that is often used is the Erichsen cupping test. In this test a hardened metallic ball, with a diameter of 20 mm, is slowly driven into a clamped sheet specimen (Figure 6.31). At some deformation, the specimen will rupture under the load applied by the ball. The travel distance of the ball on rupture is defined as the Erichsen Cupping Index (I_E). Like the tensile strength, the Erichsen Cupping Index of a weld sample can also be expressed as a fraction of the index value of the base material. In this case the Erichsen Cupping Index is indicated as $I_{E\%}$. The dimensions of the Erichsen cupping test apparatus, according to ISO norm 20482 [84], are given in Figure 6.31. Figure 6.32 shows a photograph of a laser welded AA5182-O/H111 sample after the cupping test.

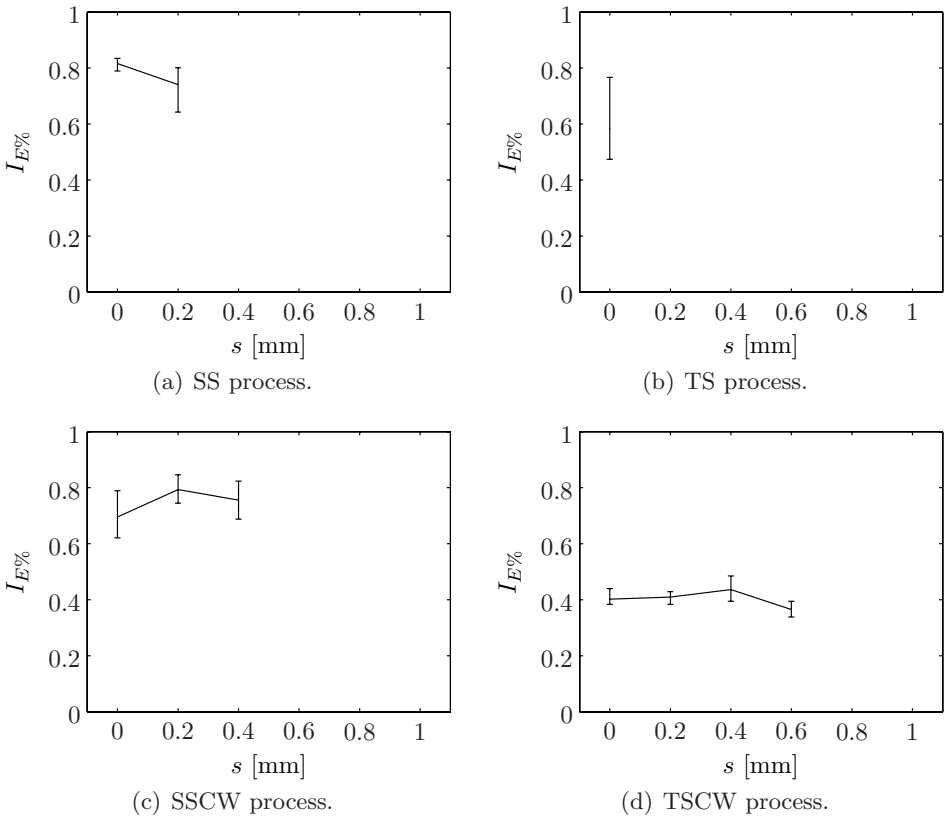

(a) SS process.

(b) TS process.

(c) SSCW process.

(d) TSCW process.

Figure 6.33: *The Erichsen Cupping test values for the welds of the different processes for 1.1 mm thick AA5182 sheets. The variations found in $I_{E\%}$ found for the different gap values s are indicated with the error bars. The base material I_E value is 8.9 mm.*

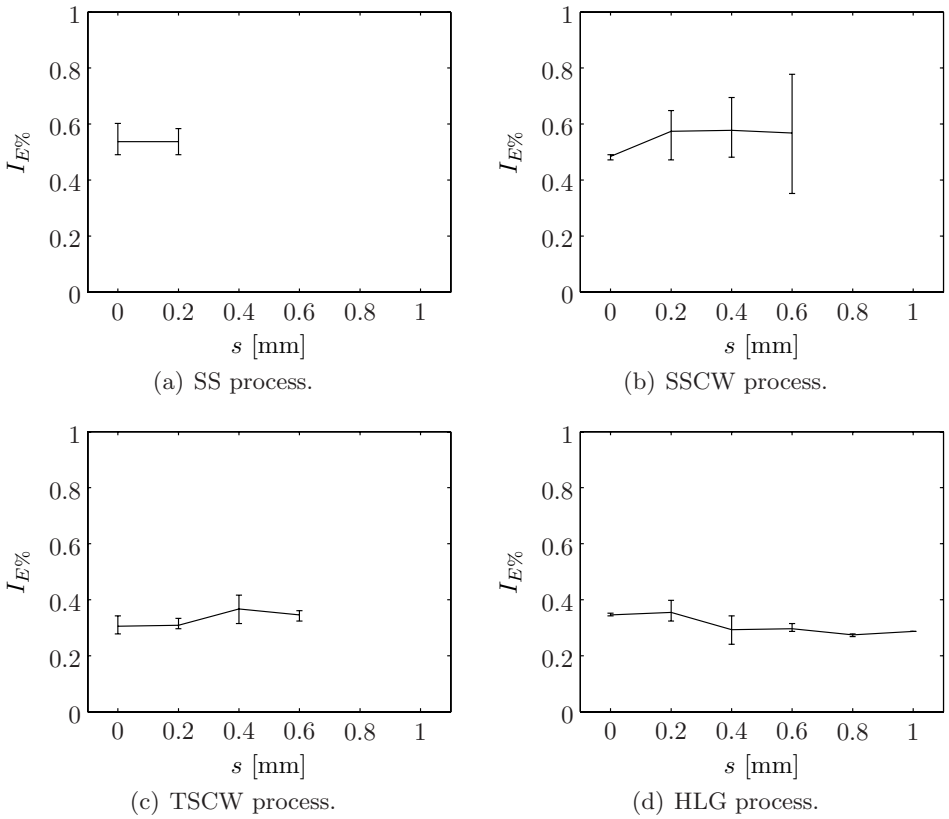

(a) SS process. (b) SSCW process.

(c) TSCW process. (d) HLG process.

Figure 6.34: *The Erichsen Cupping test values for the welds of the different processes for 2.1 mm thick AA5182 sheets. The variations found in $I_{E\%}$ found for the different gap values s are indicated with the error bars. The base material I_E value is 10.8 mm.*

The Erichsen Cupping test is a fast and simple test, which gives a good indication of the formability of welded sheets. It is a popular testing method in industry, due to its good approximation of a realistic situation, as its outcome provides a good prediction of the weld performance during for instance forming.

Figures 6.33 and 6.34 show the relative Erichsen Cupping Index $I_{E\%}$ for the welds of the different processes. For the 1.1 mm base material, I_E is 8.9 mm. For the 2.1 mm base material, I_E is 10.8 mm. For each weld configuration and gap width, three cupping tests are performed. The error bars in the figure indicate the scatter in these measurement values.

Figures 6.33 and 6.34 show that for each welding process, $I_{E\%}$ is nearly constant for different values of s. This implies that the formability of the weld does not depend on the applied gap width.

However, there are large differences between the values of $I_{E\%}$ for welds of the different laser-based welding processes. Figure 6.33 shows that for the welding of 1.1 mm sheets, the SS, TS and SSCW processes result in welds with the highest formability. For 2.1 mm sheets, the SS and the SSCW welding processes give the best deformable welds. For all the processes, the samples fail in the Melt Zone (MZ), except for the SSCW process, for which the samples generally fail near the fusion line.

6.5 Conclusions

In this chapter, the gap bridging capabilities of five different laser-based welding processes for the welding of aluminium sheets have been evaluated. In this context, welding experiments using 1.1 mm and 2.1 mm AA5182 sheets were performed. Different testing methods have been used to assess the resulting weld quality.

- In Chapter 3, it was shown that the developed monitoring system can visualise the single spot laser welding process. This monitoring system is also suited if twin spot optics and/or filler wire is used. Even the hybrid laser/arc welding process of AA5182 poses no problem.

	Sheet thickness [mm]	Gap bridging capability[1] [mm]	Quality of bead shape[2]	Microhardness [HV]	Tensile strength[3]	Erichsen cupping index[3]
SS	1.1	0.2	Moderate	74-87	0.78-0.88	0.74-0.82
TS		0	High	61-88	0.92	0.58
SSCW		0.4	High	75-95	0.84-0.90	0.70-0.79
TSCW		0.6	Moderate	61-86	0.97-0.99	0.36-0.41
SS	2.1	0.2	Low	73-91	0.78-0.85	0.54
SSCW		0.6	High	73-83	0.92-0.96	0.48-0.58
TSCW		0.6	High	72-87	0.87-0.94	0.31-0.37
HLG		1.0	Intermediate	71-91	0.77-0.88	0.27-0.35

Table 6.5: *Overview of the gap bridging capabilities of the different laser welding processes and the performance of the welds (SS: Single Spot laser welding, TS: Twin Spot laser welding, SSCW: Single Spot laser welding with Cold Wire feeding, TSCW: Twin Spot laser welding with Cold Wire feeding, HLG: Hybrid Laser/GMA welding).*

[1]The maximum seam gap that can be bridged, based on visual inspection of the weld bead.

[2]Determined from cross sections of welds with no preset gap and compared to criteria formulated in ISO norm 13919-2.

[3]Given as fraction of the base material value.

- The twin spot laser welding process in parallel configuration is not suited for welding sheet material due to the lack of tolerance for seam gaps. The hybrid laser/GMA welding process is not suited for 1.1 mm aluminium sheets due to the high heat input and wide melt pool.
- The use of filler wire is necessary to increase the gap bridging capabilities of the laser welding process.
- A precise alignment of the filler wire during the process is crucial for a good weld quality. For seam gaps over 0.6 mm, the demands on the wire alignment with the laser spot are too strict to be realised in an industrial environment.
- When gaps are present, no laser welding process can produce joints that meet quality level B (most stringent quality level according to ISO norm 13919-2).
- The use of filler wire eliminates undercut of the weld bead, increases the load bearing surface (which results in a higher load bearing capacity of the weld) and reduces the hardness peak at the boundary of the melt zone and the heat affected zone.
- Table 6.5 gives an overview of the performance of the different laser welding processes towards the different tests performed. This shows that the single spot laser welding process with cold wire feeding has the best overall performance. If for a certain application with sheet thicknesses around 2 mm the expected gap size is over 0.6 mm, the hybrid laser/GMA process might also be an option.

Chapter 7

Conclusions and Recommendations

7.1 Conclusions

In this thesis, the Nd:YAG keyhole laser welding process of thin aluminium sheets for the production of Tailor Welded Blanks (TWB's) is treated. These aluminium TWB's can potentially realise a further weight reduction of cars. Laser welding is a joining method that can reliably produce high quality joints. However, one should take care that the laser spot is properly aligned with the weld seam and that the sheet edges are properly finished to prevent seam gaps. Also the selection of good welding parameters is essential.

For an optimal strength of the TWB's, it is important that the welds fully penetrate the sheets. To facilitate this, a Fuzzy Logic Control (FLC) system was developed to guarantee full penetration under all realistic laser welding conditions. This online controller uses multiple photodiode sensors, to estimate the weld state in real time. Based on this estimation, the laser power is regulated. It is shown that the switching controller, developed by Postma for penetration control of mild steel sheets, can also be written in the FLC framework. The FLC system has been tested for the laser

welding process of aluminium AA5182 sheets in a butt weld configuration and of zinc coated steel DX54D-Z GI sheets in an overlap configuration. This shows that for DX54D-Z GI, the system can bring the process to full penetration and maintain full penetration welding under the influence of external disturbances. For the welding of AA5182 sheets, the system can also bring the process to full penetration keyhole welding. However, the system is not robust for environmental changes and a camera-based system may be a better solution to control the laser welding process of AA5182 sheets.

To facilitate the development of a camera-based monitoring system for the Nd:YAG laser welding process, spectral measurements were performed. These measurements show that mainly a broad band spectrum of thermal radiation is emitted superimposed with a few small peaks. By analysing the thermal radiation, the plume temperature is roughly estimated at 4500 K.

By using a powerful diode laser for illumination of the weld region in combination with a matching narrow band-pass filter in front of the coaxially mounted camera, clear in-situ images of the welding process can be made. Based on the availability of these diode lasers and the coating of the optics, the diode wavelength should be between 780 and 820 nm. A prototype of such a monitoring system has been built. Tests show a good performance for the Nd:YAG laser welding process of different aluminium alloys and (zinc coated) steel sheets. The system can also be used for monitoring hybrid laser/GMA welding, but a selection of an appropriate illumination wavelength is more critical here.

To realise a better understanding of the laser welding process of thin metal sheets, a 2D FEM model is applied, which computes the temperature profile and the fluid flow of the melt pool. This model can predict the melt pool contours in a qualitative way, for the keyhole laser welding process of both AA5182 and FeP04. The model results show that the latent heat of solidification causes the distinctive V-shaped tail of the melt pool, which is observed using real-time camera images of the welding process. By incorporation of the temperature dependency of the thermal conductivity and specific heat in the model, the accuracy of the predicted melt contour was enhanced. Furthermore, partial penetration of the keyhole during welding

results in an enlarged melt contour at the top surface compared to the full keyhole penetration situation. This is probably due to a stronger upward flow in the melt pool, caused by a different keyhole shape.

Top view camera observations of the keyhole show that a circular keyhole shape generally results in a weld bead with distinctive V-shaped striations. Occasionally, the keyhole is more elongated, which results in a weld bead which is smoother, but has grooves along the side of the bead and often has holes in the weld bead. This elongation effect is investigated by examining the keyhole pressure balance at the keyhole wall. This evaluation shows that the surface tension and recoil pressure terms are dominant. By taking into account the doubly curved shape of the keyhole and splitting up the surface tension pressure term, the keyhole elongation can be explained. Experiments show that keyhole elongation occurs if $r_s > 0.25b$ (AA5182) and $r_s > 0.4b$ (FeP04), where r_s is the laser spot radius and b is the sheet thickness. An estimation of the recoil pressure shows that the keyhole wall temperature is just above the normal boiling temperature of the material.

The twin spot laser welding process, in which the spots are projected side by side on the material, is not suited for welding AA5182 sheets due to the low tolerance for seam gaps. The use of filler wire is necessary to increase the gap bridging capabilities. It reduces the hardness peak in the melt zone and eliminates undercut in the weld bead. A good alignment of the filler wire with the welding process is essential for a good weld quality. For 1.1 mm AA5182 sheets, the hybrid laser/GMA welding process performs poorly due to the high heat input and a wide melt pool. The single spot laser welding process with cold wire feeding has the best overall performance rating. The hybrid laser/GMA process can also be an option for welding sheet thickness larger than 2 mm which have a seam gap larger than 0.6 mm.

7.2 Recommendations

In this work, a proof of principle of a fuzzy logic control system for penetration control during laser welding is given. This control system has been

tested for two external disturbances, which posed no problem in the case of zinc coated steel sheets. However, there are numerous other disturbances that can occur in an industrial environment. Therefore additional tests are required to investigate if this system is suited for a wider application.

The developed camera-based monitoring system has been tested for Nd:YAG laser-based welding processes of various materials. Other processes that potentially can be monitored are the CO_2 laser welding process and the Hybrid Laser/GMA welding process of steel. Both of these processes result in a much higher degree of ionisation of the weld plume, and will show more peaks in the spectrum. Spectral measurements of these processes will indicate locations of these peaks. Based on this knowledge, a suitable illumination wavelength can be selected.

In Chapter 4 it is shown that the melt pool dimensions are significantly larger if the keyhole does not fully penetrate the sheet during welding. Using digital image processing, it should be possible to automatically detect the boundaries of the melt pool by processing of the camera images of the monitoring system. Thus by tracking the melt pool boundaries it is possible to monitor online if the keyhole fully penetrates the sheets. In this way a similar camera-based penetration control system can be developed for aluminium as was demonstrated for zinc coated steel using photodiode sensors.

By extending the 2D FEM model to a 3D model, a better insight can be obtained in the 3D flow phenomena in and around the melt pool. An improved keyhole model will be of significant aid. With such a model, the observed keyhole elongation could be predicted. For verification of model results, it might be helpful to capture images of the bottom surface also during welding.

The influence of for instance shielding gas flow rates or the presence of oxide layers on the base material on the gap bridging capabilities of the different laser-based welding processes is not entirely clear. Further research could provide more information on these influences. Since in the automotive industry (zinc coated) steel is very often used, it is of interest to expand this gap bridge investigation to such materials. Such an investigation could also include studies on the tolerance for other sheet alignment defects, like

sheet height mismatch.

Appendix A

Aluminium Alloy Designation

In general aluminium alloys can be divided into two main groups: the cast and the wrought alloys. In this project aluminium plates are investigated,

Principal alloying element	Cast alloys	Wrought alloys
$\geq$ 99% Al	1xx.x	1xxx
Cu	2xx.x	2xxx
Mn	3xx.x	3xxx
Si	4xx.x	4xxx
Mg	5xx.x	5xxx
Mg + Si	6xx.x	6xxx
Zn	7xx.x	7xxx
Other elements	8xx.x	8xxx
Unused	9xx.x	9xxx

Table A.1: *The ANSI codes for the aluminium alloy groups with a common principal alloying element [8]*

which are rolled and hence belong to second group. Both groups can subsequently be subdivided into groups which have the same principal alloying component. The ANSI designation system for wrought and cast aluminium alloys uses four digits to identify the specific aluminium alloy. In Table A.1 [9, 8] the ANSI codes for the aluminium alloy groups with a common principal alloying element are given. The last two digits are used to identify the specific alloy within the group. The second digit in the ANSI code is used to indicate modifications of the original composition of the aluminium alloy within that subgroup. Thus a 57xx alloy has a modified composition compared to a 50xx alloy.

The Aluminium Association (AA) uses the ANSI standard. For wrought aluminium alloys the materials are sometimes indicated using AAxxxx, where the x's indicate the ANSI code. Besides the AA and ANSI standard, there are several other codes to indicate a certain aluminium alloy, like the UNS or the ISO standard. In this thesis the ANSI standard will be used, which is widely adopted and familiar in the field of material processing.

Each material can also have a temper designation which indicate a sequence of mechanical and thermal treatments. F indicates that no further treatment was given to the material after fabrication. Annealed materials are indicated using an O, H indicates that the material was strain hardened and T is used for heat treated materials. Suffix numbers indicate secondary treatments. The temper designation $O/H111$ for instance indicates that the material is annealed, followed by a strain hardening process (see [8] for more information).

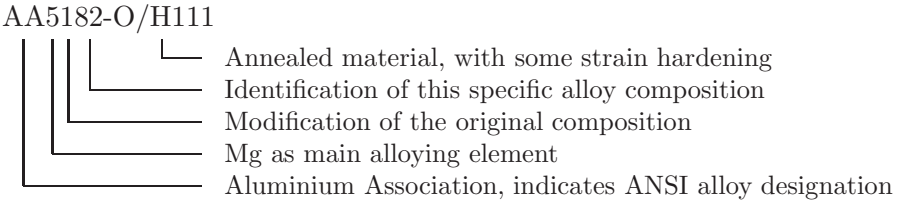

Appendix B

Filter Characteristics

In this section the transmittance of the different optical filters which are used in this work are shown.

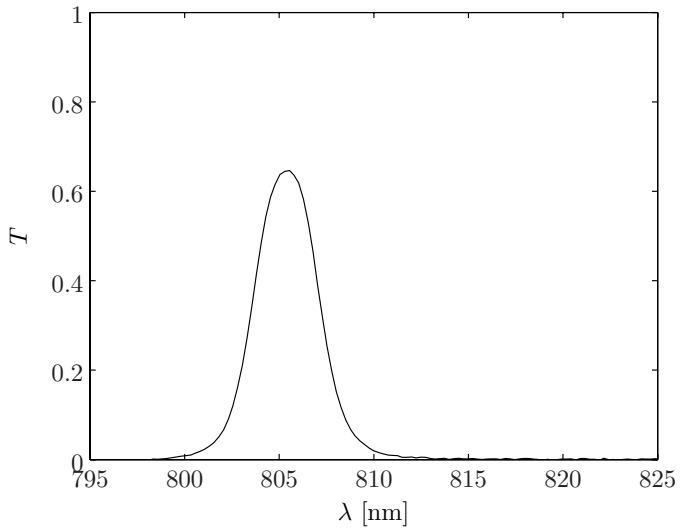

Figure B.1: *Transmittance of the Thorlabs CDI1553 805-4 filter.*

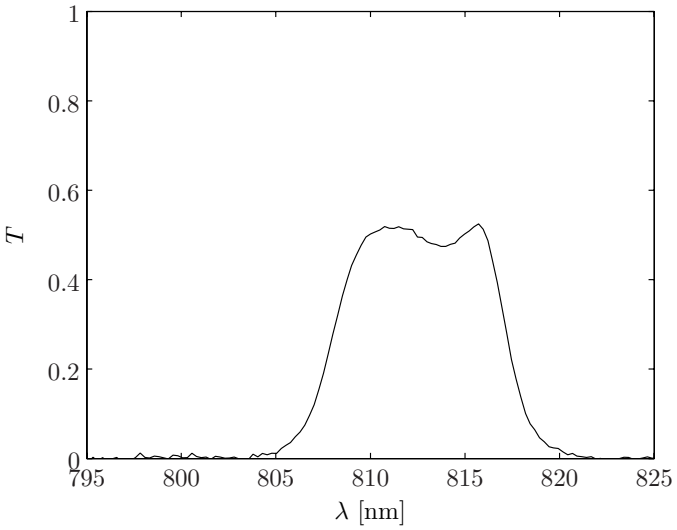

Figure B.2: *Transmittance of the Melles Griot 03FIL058 filter.*

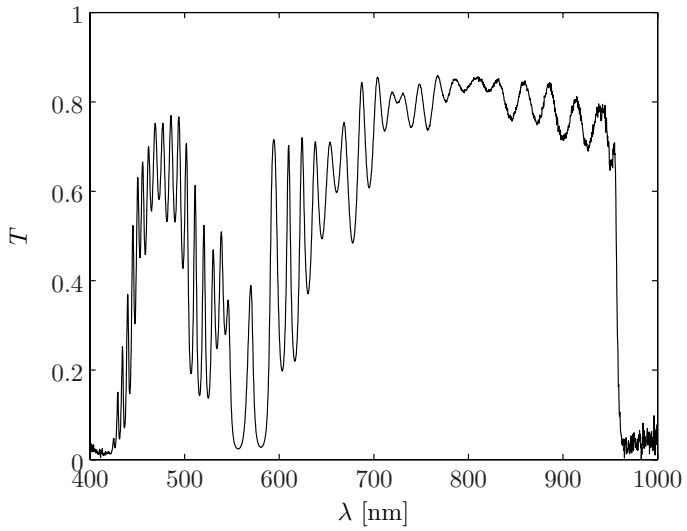

Figure B.3: *Transmittance of the Thorlabs FES0950 filter.*

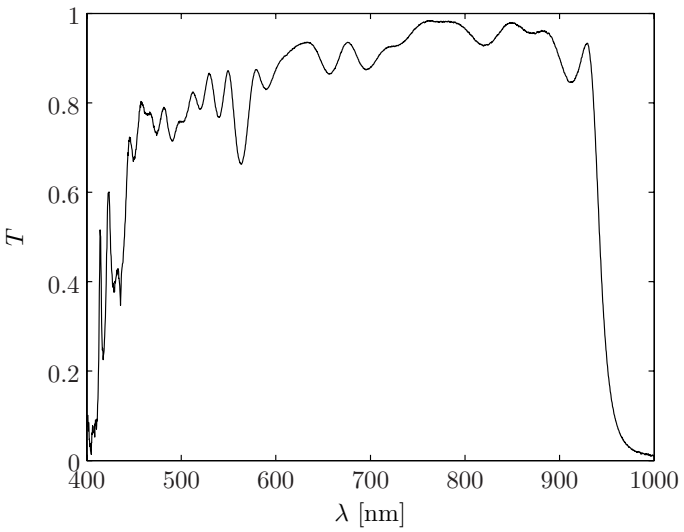

Figure B.4: *Transmittance of the Melles Griot 03SWP624 filter.*

Appendix C

Material Parameters

The material parameters of AA5182 and FeP04 which are relevant for this research are presented in following sections.

C.1 AA5182

Element	Content [wt%]
Mg	4.90
Mn	0.26
Cu	0.11
Si	0.08
Ti	0.01
Al	Bal.

Table C.1: *The chemical composition of the AA5182-O/H111 base material (Courtesy of Corus).*

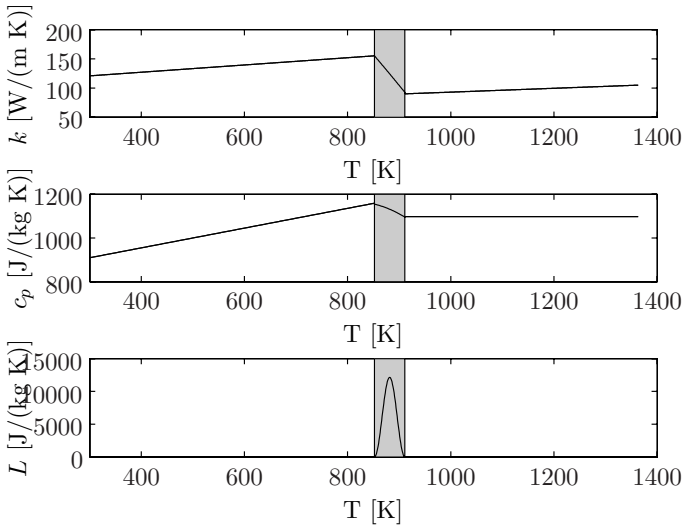

Figure C.1: *The thermal conductivity k [49, 50], the specific heat c_p [50] and the latent heat L for AA5182 [43, 51], as a function of the temperature. The gray area indicates the melt trajectory [8, 51].*

A	Absorptivity[1] [1, 37]	< 0.1	
T_s [K]	Solidus temp. [8, 50, 51]	852	
T_l [K]	Liquidus temp. [8, 50, 51]	911	
T_b [K]	Boiling temp.[2] [49]	1363	
L_m [J/kg]	Latent heat of the solid-liquid phase transition [51]	$3.58 \cdot 10^5$	
γ [N/m]	Surface tension [59]	0.6	
μ [kg/(m s)]	Dynamic viscosity [8]	$1.05 \cdot 10^{-3}$	
ρ [kg/m^3]	Density[3] [51]	2454	
k [W/(m K)]	Thermal conductivity [49, 50]	$0.06230T + 102.2$	$T_r \leq T \leq T_s$
		$-4.800 \cdot 10^{-4}T^2 - 0.2178T + 689.3$	$T_s < T \leq T_l$
		$0.03300T + 59.99$	$T_l < T \leq T_b$
c_p [J/(kg K)]	Specific heat[4] [50]	$0.4520T + 773.6$	$T_r \leq T \leq T_s$
		1097	$T_s < T \leq T_l$
		$-7.400 \cdot 10^{-3}T^2 + 12.04T - 3732$	$T_l < T \leq T_b$

Table C.2: *The relevant properties of AA5182.*

[1] For $\lambda = 1064$ nm.
[2] Boiling temperature of Mg (boiling temperature of Al is 2792 K)
[3] Averaged over temperature
[4] Excluding the latent heat

C.2 FeP04

Element	Content [wt%]
Mn	0.227
Al	0.047
C	0.047
Cr	0.020
Ni	0.020
S	0.013
Cu	0.010
P	0.010
Sn	0.010
Si	0.005
Mo	0.002
Fe	Bal.

Table C.3: *The chemical composition of the FeP04 base material (Courtesy of Corus).*

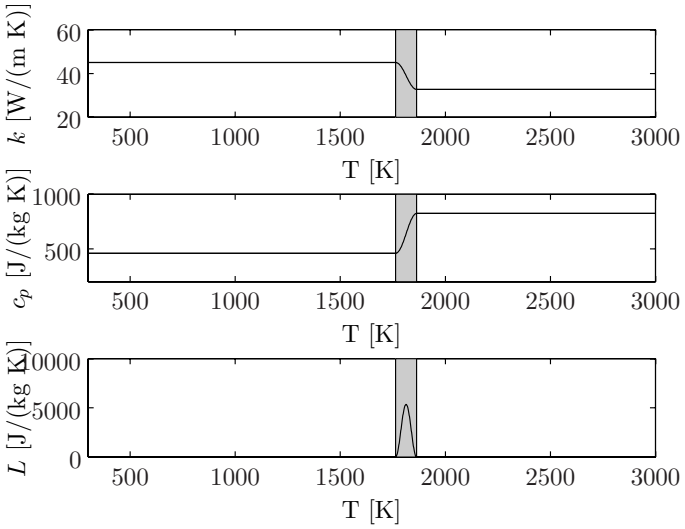

Figure C.2: *The thermal conductivity k [85, 86], the specific heat c_p [85, 86] and the latent heat L for FeP04 [85], as a function of the temperature. The gray area indicates the melt trajectory [85].*

A	Absorptivity[1] [1, 37]	≈ 0.4
T_s [K]	Solidus temp. [85]	1763
T_l [K]	Liquidus temp. [85]	1863
T_b [K]	Boiling temp. [49]	3134
L_m [J/kg]	Latent heat of the solid-liquid phase transition [85]	$2.67 \cdot 10^5$
γ [N/m]	Surface tension [59]	1.6
μ [kg/(m s)]	Dynamic viscosity [85]	$2.25 \cdot 10^{-3}$
ρ [kg/m^3]	Density [86]	$6.7 \cdot 10^3$
k [W/(m K)]	Thermal conductivity [85, 86]	45.0 $T_r \leq T \leq T_s$ $32.7 + 12.3\cos^2(0.0157T - 27.69)$ $T_s < T \leq T_l$ 32.7 $T_l < T \leq T_b$
c_p [J/(kg K)]	Specific heat[2] [85, 86]	460 $T_r \leq T \leq T_s$ $824 - 364\cos^2(0.0157T - 27.69)$ $T_s < T \leq T_l$ 824 $T_l < T \leq T_b$

Table C.4: *The relevant properties of FeP04.*

[1]For $\lambda = 1064$ nm.
[2]Excluding the latent heat

Appendix D

Estimation of Reynolds Number for Melt Pool Flow

To determine if the fluid flow around the keyhole during full penetration keyhole welding is laminar or turbulent, the Reynolds number can be used. Under the assumption that the molten material is homogeneous and incompressible, the flow can be modelled as an open channel flow. The Reynolds number of an open channel flow is given by [60]

$$\mathrm{Re} = \frac{\rho \bar{v}_f R_h}{\mu}, \tag{D.1}$$

where ρ is the density of the fluid, $\bar{v}_f$ is the average velocity of the fluid in the channel and μ is the dynamic viscosity of the fluid. The hydraulic radius R_h is defined as the cross sectional area of the flow A_f divided by the cross sectional wetted length l_f. Figure D.1 shows a section of the fluid flow along the keyhole side wall.

The average flow velocity of the fluid flow can be calculated by means of conservation of mass. If the mass flux of the evaporated and ejected material is assumed to be negligible compared to the mass flux of the fluid flow, then the mass flux by solid material supply in front of the melt pool ($\dot{m}_1$) must equal the mass flux passing through area A_f in Figure D.1 ($\dot{m}_2$)

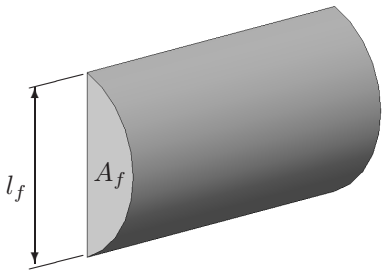

Figure D.1: *Section of approximate fluid flow along the sides of the keyhole.*

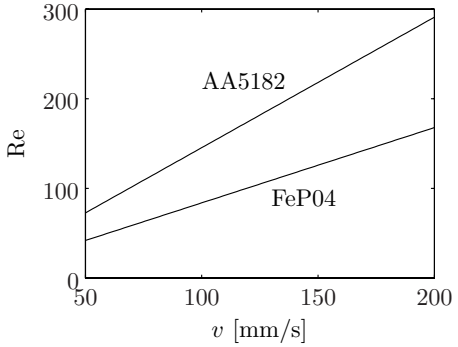

Figure D.2: *Reynolds numbers for the fluid flow along the keyhole side as a function of the welding speed.*

$$\dot{m}_1 = \dot{m}_2. \tag{D.2}$$

The mass fluxes $\dot{m}_1$ and $\dot{m}_2$ can be described as

$$\begin{aligned} \dot{m}_1 &= \rho w_m b v \\ \dot{m}_2 &= 2\rho A_f \bar{v}_f, \end{aligned} \tag{D.3}$$

respectively. Here w_m is the width of the melt pool, b is the material thickness and v is the welding speed. Combining Equations D.2 and D.3, gives

$$\bar{v}_f = \frac{w_m b v}{2A_f}. \tag{D.4}$$

Therefore the Reynolds number for this model can be approximated by

$$\mathrm{Re} = \frac{\rho w_m v}{2\mu}. \tag{D.5}$$

In Appendix C the material parameters are given for AA5182 and FeP04. From the camera images the value of w_m is estimated to be 1.2

and 0.48 mm for AA5182 and FeP04, respectively, for a laser spot diameter of 0.45 mm. Figure D.2 shows Re for the welding process of these materials as a function of v.

The values show that for both materials Re < 500 for all realistic welding speeds, indicating that the fluid flow at the sides of the keyhole is laminar. This is consistent with earlier findings for FeP04 [43].

The Reynolds number of the melt flow in the melt pool at the rear keyhole wall cannot be calculated easily. In this part of the flow, the value of R_h will be higher than at the keyhole side walls. However, the flow velocity in this part will be somewhat lower due to viscous forces. Therefore, despite some vortices in the melt pool flow as visible in Figure 4.5(a), one can consider the flow to be laminar.

Bibliography

[1] W.W. Duley. *Laser Welding*. John Wiley and Sons, Inc, first edition, 1999.

[2] D. Schuöcker. *Handbook of the EuroLaser Acadamy*. Chapman and Hall, first edition, 1998.

[3] International Iron & Steel Institute. www.ulsab.org.

[4] D. van Nieuwerburgh, A. Smeyers, and T. van der Veldt. Market introduction of Al tailor welded blank technology. *Proceedings of EALA '04*, 2004.

[5] R.W. Davies, H.E. Oliver, M.T. Smith, and G.J. Grant. Characterizing Al Tailor-Welded Blanks for Automotive Applications. *The Journal of the Minerals, Metals and Materials Society*, 51(11):46–50, 1999.

[6] Vereniging FME-CWM. vm 121: Hoogvermogen lasers voor het bewerken van materialen, 2002.

[7] E. Cicală, G. Duffet, H. Andrzejewski, D. Grevey, and S. Ignat. Hot cracking in AlMgSi alloy laser welding operating parameters and their effects. *Materials Science and Engineering A*, 395:1–9, 2005.

[8] ASM International. *ASM Specialty Handbook - Aluminum and Aluminum Alloys*. first edition, 1993.

[9] G. Mathers. *The welding of aluminium and its alloys*. Woodhead Publishing Ltd, first edition, 2002.

[10] M. Jurca, D. Mokler, R. Ruican, and T. Zeller. On-line Nd-YAG Laser Welding Process Monitoring. *Proceedings of SPIE '94*, 2207:342–352, 1994.

[11] C. Dietz, M. Jurca, L Schlichtermann, and M. Kogel-Hollacher. Closed-Loop Control System for Laser Welding of Transmission Parts. *Proceedings of ICALEO '98*, pages 178–187, 1998.

[12] H.K. Tönshoff, A. Ostendorf, and W. Specker. Quality Assurance of Laser Welding Processes by Adaptive Closed-Loop Process Control. *Proceedings of ICALEO '00*, pages E252–E261, 2000.

[13] C. Deininger, J. Müller-Borhanian, F. Dausinger, and H. Hügel. Development of Multi-Detector Systems for the Process Monitoring of Laser Beam Welding Capable for Industrial Use. *Proceedings of LANE '04*, pages 107–117, 2004.

[14] A. Ali and D.F. Farson. Analysis of Laser Weld Quality Sensor Signals by Stepwise LDA. *Proceedings of ICALEO '99*, pages 39–48, 1999.

[15] D.F. Farson, A. Ali, and X.C. Li. Laser weld penetration monitoring with multiple emission signal measurements. *Journal of Laser Applications*, 11:47–53, 1999.

[16] S. Postma, R.G.K.M. Aarts, J. Meijer, and J.B. Jonker. Penetration Control in Laser Welding of Sheet Metal. *Journal of Laser Applications*, pages 210–214, 2002.

[17] S. Postma. *Weld Pool Control in Nd:YAG Laser Welding*. PhD thesis, University of Twente, 2003.

[18] M.W. de Graaf, J. Olde Benneker, J. Meijer, and J.B. Jonker. Robust Process-Controller for Nd:YAG Welding. *Proceedings of ICALEO '05*, pages 862–868, 2005.

Bibliography

[19] J. Jauregui. Implementation and testing of a control scheme for laser welding. Master's thesis, University of Twente, 2006.

[20] K.M. Passino and S. Yurkovich. *Fuzzy Control*. Addison Wesley Longman, Inc, first edition, 1998.

[21] Trumpf Laser GmbH. www.trumpf-laser.com.

[22] A. Hatwig, R. Kutzner, and M. Jurca. Laser on-line überwachen mit dem Laser Welding Monitor LWM. *Laser Magazin*, 4:20–25, 1990.

[23] J. Griebsch, L. Schlichtermann, M. Jurca, S. Heissler, and D. Funk. On-line monitoring of laser welding. *Industrial Laser Review*, 12(5): 7–10, 1997.

[24] M. Kogel-Hollacher, M. Jurca, C. Dietz, G. Janssen, and E.F. Davila Lozada. Quality assurance in pulsed seam laser welding. *Proceedings of ICALEO '98*, pages 168–177, 1998.

[25] Precitec Group. www.precitec.de.

[26] R. Güttler. Sensor detects faults in the keyhole. *Opto& Laser Europe*, page 13, 1998.

[27] Laser Zentum Hannover eV. www.lzh.de.

[28] 4D GmbH. www.4d-gmbh.de.

[29] J. Caanen. Camera based sensor system for hybrid laser/MIG welding of aluminium. Master's thesis, University of Twente, 2006.

[30] J. Veenstra. Improved Gap Tolerance for Laser Welding of Aluminium Using Twin Spot Techniques. Master's thesis, University of Twente, 2006.

[31] B.J. Aalderink, R.G.K.M. Aarts, J.B. Jonker, and J. Meijer. Weld Plume Emissions During Nd:YAG Laser Welding. *Proceedings of LIM '05*, pages 413–417, 2005.

[32] B.J. Aalderink, R.G.K.M. Aarts, J.B. Jonker, and J. Meijer. Experimental Observations of the Laser Keyhole Welding Process of AA5182. *Proceedings of ICALEO '05*, pages 832–836, 2005.

[33] A. Sun, E. Kannatey-Asibu jr., and M. Gartner. Sensor systems for real-time monitoring of laser weld quality. *Journal of Laser Applications*, 11:153–168, 1999.

[34] A. Matsunawa, J.D. Kim, S. Takemoto, and S. Katayama. Spectroscopic Studies on Laser Induced Plume of Aluminium Alloys. *Proceedings of ICALEO '95*, pages 719–728, 1995.

[35] R.E. Müller, H. Gu, N. Ferguson, M. Ogmen, and W.W. Duley. Real Time Optical Spectral Monitoring of Laser Welding Plumes. *Proceedings of ICALEO '98*, pages C132–C138, 1998.

[36] E. Hecht. *Optics*. Addison Wesley Longman, Inc, third edition, 1998.

[37] M. von Allmen and A. Blatter. *Laser-Beam Interactions with Materials*. Springer, second edition, 1994.

[38] J. Beersiek. A CMOS camera as a tool for process analysis not only for laser beam welding. *Proceedings of ICALEO '01*, 2001.

[39] J. Müller-Borhanian, C. Deininger, F.H. Dausinger, and H. Hügel. Spatially Resolved On-Line Monitoring During Laser Beam Welding of Steel and Aluminum. *Proceedings of ICALEO '04*, 2004.

[40] Laserwave srl. www.laserw.com.

[41] PixeLINK. www.pixelink.com.

[42] Visible Solutions, Inc. www.visiblesolutions.com.

[43] D.F. de Lange, S. Postma, and J. Meijer. Modelling and Observation of Laser Welding: The Effect of Latent Heat. *Proceedings of ICALEO '03*, 2003.

Bibliography

[44] B.J. Aalderink, D.F. de Lange, R.G.K.M. Aarts, and J. Meijer. Experimental verification of multi-physical modelling of the keyhole laser welding process. *Proceedings of ICALEO '06*, pages 479–486, 2006.

[45] R. Fabbro and K. Chouf. Keyhole Modeling During Laser Welding. *Journal of Applied Physics*, 87:4075–4083, 2000.

[46] P.G. Klemens. Heat balances and flow conditions for electron beam and laser welding. *Journal of Applied Physics*, 47:2165–2174, 1976.

[47] A.F.H. Kaplan. A model of deep penetration laser welding based on calculation of the keyhole profile. *Journal of Physics D: Applied Physics*, 27:1805–1814, 1994.

[48] P. Li, H. Hyungson, and J. Mazumder. Modeling Laser Keyhole-Welding with Adaptive Mesh Refinement. *Proceedings of ICALEO '05*, pages 512–517, 2005.

[49] CRC Press. *CRC Handbook of Chemistry and Physics*. 84 edition, 2003.

[50] J. Sengupta, S.L. Cockcroft, D.M. Maijer, and A. Larouche. Quantification of temperature, stress, and strain fields during the start-up phase of direct chill casting process by using a 3D fully coupled thermal and stress model for AA5182 ingots. *Materials Science and Engineering A*, 397:157–177, 2005.

[51] K.C. Mills. *Recommended values of thermophysical properties for selected commercial alloys*. Woodhead Publishing Limited, first edition, 2002.

[52] Comsol AB. www.comsol.com.

[53] Comsol AB. *COMSOL Multiphysics User's Guide*, 2005.

[54] B.J. Aalderink, D.F. de Lange, R.G.K.M. Aarts, and J. Meijer. Experimental Observation of Keyhole Shapes in the Laser Welding of Aluminium Blanks. *Journal of Laser Applications*, 2007. in press.

[55] B.J. Aalderink, D.F. de Lange, R.G.K.M. Aarts, and J. Meijer. Keyhole shapes during laser welding of thin metal sheets. *Journal of Physics D: Applied Physics*, 40:5388–5393, 2007.

[56] J. Kroos, U. Gratzke, and G. Simon. Towards a self-consistent model of the keyhole in penetration laser beam welding. *Journal of Physics D: Applied Physics*, 26:474–480, 1993.

[57] R. Ducharme, K. Williams, P. Kapadia, J. Dowden, B. Steen, and M. Glowacki. The laser welding of thin metal sheets: an integrated keyhole and weld pool model with supporting experiments. *Journal of Physics D: Applied Physics*, 27:1619–1627, 1994.

[58] T. Klein, M. Vicanek, and G. Simon. Forced oscillations of the keyhole in penetration laser beam welding. *Journal of Physics D: Applied Physics*, 29:322–332, 1996.

[59] J. Szekely. *Fluid flow phenomena in metals processing.* Academic Press, Inc, first edition, 1979.

[60] B.R. Munson, D.F. Young, and T.H. Okiishi. *Fundamentals of Fluid Mechanics.* John Wiley and Sons, Inc, third edition, 1998.

[61] X. Chen and H.X. Wang. A calculation model for the evaporation recoil pressure in laser material processing. *Journal of Physics D: Applied Physics*, 34:2637–2642, 2001.

[62] S.I. Anisimov and V.A. Khokhlov. *Instabilities in Laser-Matter Interaction.* CRC Press, first edition, 1995.

[63] W. Wisniak. Frederick Thomas Trouton: The Man, the Rule, and the Ratio. *The Chemical Educator*, 6:55–61, 2001.

[64] R. Fabbro R, S. Slimani, I. Doudet, F. Coste, and F. Briand. Experimental study of the dynamical coupling between the induced vapour plume and the melt pool for NdYag CW laser welding. *Journal of Physics D: Applied Physics*, 39:394–400, 2006.

[65] B. Hohenberger, C.-L. Chang, C. Schinzel, F. Dausinger, and H. Hügel. Laser Welding with Nd:YAG-Multi-Beam Technique. *Proceedings of ICALEO '99*, pages D167–D176, 1999.

[66] T. Iwase, K. Shibata, H. Sakamoto, F. Dausinger, B. Hohenberger, M. Müller, A. Matsunawa, and N. Seto. Real Time X-ray Observations of Dual Focus Beam Welding of Aluminium Alloys. *Proceedings of ICALEO '00*, pages 26–34, 2000.

[67] M. Grupp, T. Seefeld, and G. Sepold. Laser Beam Welding of Aluminium Alloys with Diode Pumped Nd:YAG Lasers. *Proceedings of ICALEO '01*, 2001.

[68] J. Schneegans. *Untersuchungen zum Laserstrahlschweissen mit Zusatzdrahtfürung an un- und niedriglegierten Stählen.* PhD thesis, Rheinisch-Westfälische Technische Hochschule Aachen, 1992.

[69] D. Fuest. *Entwicklung von Systemkomponenten zur Automatisierung von CO_2-Laserstrahlprozessen mit Zusatzdraht.* PhD thesis, Rheinisch-Westfälische Technische Hochschule Aachen, 1995.

[70] C. Bagger and F.O. Olsen. Review of laser hybrid welding. *Journal of Laser Applications*, 17:1–14, 2005.

[71] S. Katayama, Y. Naito, S. Uchiumi, and M. Mizutani. Penetration and Porosity Prevention Mechanism in Laser-Arc Hybrid Welding. *Proceedings of LIM '05*, pages 193–198, 2005.

[72] A. Mahrle and E. Beyer. Hybrid laser beam welding - Classification, characteristics, and applications. *Journal of Laser Applications*, 18: 169–180, 2006.

[73] B.J. Aalderink, R.G.K.M. Aarts, and J. Meijer. Increased gap bridging capabilities using twin spot and hybrid laser/GMA welding for AA5182. *Proceedings of LIM '07*, pages 79–83, 2007.

[74] Fronius International GmbH. www.fronius.com.

[75] B. Hu. *Nd/YAG Laser-assisted Arc Welding*. PhD thesis, Delft University of Technology, 2002.

[76] A. Huwer. *Sensorsystem zur Erfassung variabler Fügespaltweiten beim Laserstrahlschweissen im Stumpfstoss*. PhD thesis, Rheinisch-Westfälische Technische Hochschule Aachen, 1993.

[77] F. Armao. Invesigation of the smut generation during welding aluminium alloy with GMAW. *Practical Welding Today*, 7:40–41, 2003.

[78] S. Jyogan, K. Kogane, S. Sasabe, H. Hirano, T. Ochiai, and T. Okita. How to recognize, minimize weld smut. *Proceedings of Inalco '98*, pages 17–25, 1998.

[79] W.D. Callister, Jr. *Material Science and Engineering - An Introduction*. John Wiley and Sons, Inc, fourth edition, 1997.

[80] W. Wen and J.G. Morris. The effect of cold rolling and annealing on the serrated yielding phenomenon of AA5182 aluminum alloy. *Materials Science and Engineering A*, 373:204216, 2004.

[81] ISO. International Standard, ISO 13919-2: Welding - Electron and laser beam welded joints - Guidance on quality levels for imperfections - Part 2: Aluminium and its weldable alloys, 2001.

[82] ASTM International. ASTM, E 384 - $99^{\epsilon 1}$: Standard Test Method for Microindentation Hardness of Materials, 1999.

[83] ASTM International. ASTM, E 8M - 98: Standard Test Method for Tension Testing of Metallic Materials [Metric], 1998.

[84] ISO. International Standard, ISO 20482: Metallic materials - Sheet and strip - Erichsen cupping test, 2003.

[85] J.M. Dowden. *The Mathematics of Thermal Modeling*. Chapman and Hall, first edition, 2001.

[86] A. Bejan. *Heat Transfer*. John Wiley and Sons, Inc, first edition, 1993.

Summary

Weight reduction is important in the automotive industry. To achieve this, Tailor Welded Blanks (TWB's) are used. Good examples are body panels consisting of sheets which are welded together and formed into the desired shape. TWB's are thicker at highly loaded places and thinner in other areas. In contrast to steel, aluminium TWB's have been introduced only recently. The forming of the sheets poses high requirements on the welds. Laser welding has the potential to produce these strong, yet deformable welds.

During TWB production, both full penetration welding (high weld strength) and a high welding speed (low production costs) are important. An online weld penetration control system can facilitate both. For the welding of aluminium alloy AA5182 and for zinc coated steel DX54D-Z sheets, a fuzzy logic penetration control system was developed and tested. This controller adjusts the laser power based on online photodiode sensor measurements. For zinc coated steel sheets, this system performs well and is suited for industrial application. For aluminium alloy sheets though the controller is very sensitive for external disturbances.

A camera-based monitoring system of the laser welding process of aluminium is developed to monitor this laser welding process. The images can also be used to monitor or control the weld quality online. Based on spectroscopic measurements of the welding process, a diode laser is selected to illuminate the weld zone and a matching narrow band-pass filter is placed in front of a CMOS camera. Tests show that this monitoring system can be used to monitor and control the Nd:YAG laser welding process of dif-

ferent aluminium alloys and (zinc coated) steel sheets. A 2D finite element model was developed which calculates the temperature and flow field in the melt pool for keyhole welding of thin metal sheets. The melt and keyhole contours are not explicitly tracked, but follow from the melt and vaporisation isotherms. A comparison of the model results with camera images shows that the model gives a good estimation of the melt contour. The incorporation of latent heat and temperature dependent material parameters in the model are mandatory for an accurate prediction of the melt pool shape. Furthermore, the penetration of the keyhole during welding has a significant influence on the fluid flow in the melt pool.

In some welding experiments using the developed monitoring system, an elongated keyhole shape is observed. By considering the pressure balance at the keyhole wall and by taking the finite thickness of the material into account, this effect can be explained. In this pressure balance, the surface tension pressure is split into a term that tries to close the keyhole and another term that tries to open it. When the keyhole diameter is in the order of the sheet thickness, the closing pressures can no longer balance the opening pressures and the keyhole elongates. Evaluation of the vaporisation pressure at the keyhole wall shows that the wall temperature is just over the normal boiling temperature of the material.

The Single Spot laser welding (SS) process of TWB's has a low tolerance for seam gaps. This tolerance can be improved by using other laser-based welding processes, like Single Spot laser welding with Cold Wire feeding (SSCW), Twin Spot laser welding with Cold Wire feeding (TSCW) and Hybrid Laser/GMA welding (HLG). The gap bridging capabilities of these processes are tested experimentally and show that feeding wire is mandatory to increase the gap bridging capabilities. For 1.1 mm AA5182 sheets, the SSCW process has the best overall performance. For 2.1 mm AA5182 sheets the HLG welding process shows large gap bridging capabilities at the cost of weld strength and deformability.

Samenvatting

Gewichtsbesparing is erg belangrijk in de automobielindustrie. Hiervoor worden onder andere Tailor Welded Blanks (TWB's) gebruikt. Dit zijn gelaste plaatdelen van verschillende diktes en/of materialen welke in een bepaalde vorm worden gepest. TWB's zijn dikker op plaatsen waar veel sterkte nodig is en dunner op de andere plaatsen. In tegenstelling tot TWB's van staal zijn TWB's van aluminium pas recentelijk geïntroduceerd. Het persen van de plaatdelen stelt hoge eisen aan de lassen. Deze sterke en goed vervormbare lassen kunnen potentieel met laserlassen gemaakt worden.

Een volledige penetratie van de lassen (goede lassterkte) en een hoge lassnelheid (lage productiekosten) zijn belangrijk tijdens de TWB productie. Een online regelsysteem dat de laspenetratie regelt kan helpen om aan beide eisen te voldoen. Een fuzzy logic regelsysteem voor de laspenetratie bij het lassen van platen van aluminium legering AA5182 en verzinkt staal DX54D-Z is ontwikkeld. Deze regelaar regelt het laservermogen op basis van fotodiode sensorsignalen van het lasproces. Voor het lassen van verzinkt staal functioneert het systeem uitstekend en is het geschikt voor industriële implementatie. Voor het lassen van de aluminium platen is het systeem echter heel gevoelig voor externe verstoringen.

Voor het beter leren begrijpen van het aluminium laserlasproces is een camera gebaseerd laserlasobservatiesysteem ontwikkeld. De resulterende beelden kunnen ook voor online procesbewaking en procesregeling gebruikt worden. Op basis van spectroscopische metingen van het lasproces is een diode laser geselecteerd voor procesverlichting. Een bijpassend optisch in-

terferentiefilter is voor een CMOS camera geplaatst. Experimentele resultaten laten zien dat het observatiesysteem gebruikt kan worden bij het Nd:YAG laserlassen van verschillende aluminiumlegeringen en (verzinkte) staalplaten.

Een 2D eindige elementen model is ontwikkeld voor het berekenen van de temperatuursdistributie en de stromingen in het smeltbad bij het keyhole-lassen van dunne metaalplaten. In dit model worden de keyhole- en smeltcontour niet expliciet opgeslagen, maar volgen deze uit de verdampings- en smeltisothermen. Een vergelijking van de modelresultaten met camerabeelden van het lasproces laat zien dat het model goede schattingen geeft van de smeltcontour. Het modelleren van latente warmte en het gebruik van temperatuursafhankelijke materiaalparameters is noodzakelijk voor een goede schatting van deze smeltcontour. Verder blijkt het penetreren van de keyhole door de plaat een significante invloed te hebben op de stroming in het smeltbad.

Met gebruikmaking van het observatiesysteem kan zichtbaar gemaakt worden dat de keyhole zich verlengt onder sommige omstandigheden. Door de drukbalans aan de keyhole-wand te bekijken, terwijl de eindige dikte van de plaat in ogenschouw wordt genomen, kan dit verlengingseffect verklaard worden. In de drukbalans wordt de oppervlaktespanningsterm gesplitst in een deel dat de keyhole probeert te sluiten en een deel dat de keyhole wil openen. Als de keyhole diameter de zelfde orde van grootte heeft als de plaatdikte, dan worden de keyhole-openende termen dominant en zal de keyhole gaan verlengen. Een evaluatie van de verdampingsdruk aan de keyhole-wand laat zien dat de wandtemperatuur net boven het atmosferische kookpunt van het materiaal ligt.

Het Single Spot (SS) laserlasproces van TWB's heeft een lage tolerantie voor spleten tussen de plaatdelen. Deze spleettolerantie kan worden vergroot door gebruik te maken van toevoerdraad, een twin spot objectief of het hybride laser/MIG lasproces. De spleetoverbruggende capaciteit van vijf verschillende laser-gebaseerde lasprocessen is vergeleken. Deze experimenten laten zien dat het gebruik van toevoerdraad vereist is om de spleettolerantie te vergroten. Voor 1.1 mm AA5182 platen geeft het SS lasproces in combinatie met koude draadtoevoer de beste resultaten. Voor 2.1 mm

AA5182 platen kan met het hybride laser/MIG lasproces nog grotere spleten overbrugd worden, maar dit gaat wel ten koste van de treksterkte en vervormbaarheid van de lassen.